UNIVERSITY OF TRENTO

DEPARTMENT OF PHYSICS

THESIS

SUBMITTED TO THE

DOCTORAL SCHOOL IN PHYSICS

BY

LUCA MATTEO MARTINI

IN CANDIDATURE FOR THE DEGREE OF

PHILOSOPHIAE DOCTOR - DOTTORE DI RICERCA

DENSITY MEASUREMENT OF OH RADICALS IN NON-THERMAL PLASMAS BY LASER INDUCED FLUORESCENCE AND TIME-RESOLVED ABSORPTION SPECTROSCOPY

TUTOR: PROF. PAOLO TOSI

CO-TUTOR: DOTT. GIORGIO DILECCE - CNR

27° PhD cycle

a Stefano e Dolores

Members of the doctoral thesis committee

- Prof. Gino Mariotto (chair), Università degli Studi di Verona.
- Prof. Vittorio Colombo, Università degli Studi di Bologna.
- Prof. Giulio Monanco, Università degli Studi di Trento.

Trento, January 22nd, 2015

Abstract

In the present thesis work, we have developed two different experimental setups for the optical detection of the OH radical in discharges at atmospheric pressure. The first one allows us to improve the time-resolved broad-band absorption spectroscopy. The main advances of the new set up are a better collimation of the UV light and a novel gating scheme. They both significantly reduce the interference of the plasma-induced emission on the absorption measurement. The second setup is dedicated to an improved laser induced fluorescence experiment, which takes advantage of a novel multi-transition excitation scheme. This permits the simultaneous measurements of both the OH density and its ground state rotational temperature. In addition, we have developed a new rate-equation model to rationalize LIF spectra, by taking into account the electronic quenching, the vibrational and rotational energy transfers, and the spatial profile of the laser beam. Finally, the electrical power dissipated in the discharge was accurately measured.

Acknowledgements

I acknowledge my tutor Prof. Paolo Tosi for his support, patience, encouragement, and scientific guidance throughout my PhD work. I also thank my co-tutor Dr. Giorgio Dilecce for sharing his experience and ideas on optical diagnostics and plasma physics. Dr. Mario Scotoni helped me with the laser source, and I am grateful to him for helpful advice and inspiring discussions. I thank Dr. Matteo Franchi for helping me to develop embedded systems, and Dr. Marco Scapinello for working with me. Thanks are due to all the members of the Atomic and Molecular Physics Group, for the great atmosphere and for making my everyday life so enjoyable. Finally, I thank my parents and all my family for supporting me. Especially, I would like to thank my wife for her encouragement, support and patience during the Doctoral course.

Contents

Chapter 1

Introduction

1.1 Applications of atmospheric-pressure non-thermal plasmas

Laboratory plasmas are ionised gases, in the vast majority of the cases sustained by the application of electric fields. The energy of the electric field is transferred, in the first instance, to free electrons. It is subsequently distributed through collisions to the feedstock molecules and their dissociation products. The sum of all possible excitation mechanisms leads to the key aspect of non thermal plasmas (NTPs): the injected energy is not equally distributed across all the species and their degrees of freedom. In particular, heating of the gas can remain low (due to the large mass difference between the colliding electron and molecule), while certain molecular states are highly excited. They promote bond breaking and dissociation. Controlling and tailoring the non-equilibrium nature of the plasma is the key to delivering the injected energy specifically to the bonds that are to be broken up. In essence, NTP is an environment that is far from thermodynamic equilibrium conditions so that conventional chemical processes are intensified and very high values of energy efficiency can be achieved. Techniques based on atmospheric pressure non thermal plasmas are used in several different fields. Important examples directly related to the present research are the plasma reforming of CO_2 for the production of solar fuels, the plasma destruction of pollutants and the plasma medicine. Regardless of the specific application, the quantitative detection of the active species generated in the plasma is an imperative requirement for the understanding of the plasma effects, because experimental molecular densities can be

compared with the results of model calculations, and eventually validate them. The quantification of transient species is particularly challenging. My research activity in the last three years, at the Doctoral School in Physics of the University of Trento, was devoted to develop optical diagnostics in gaseous discharges for the detection of transient species, and in particular of the OH radical.

1.1.1 Plasma reforming and solar fuels

Solar fuels are energy vectors that are produced from CO_2 by using renewable energy sources, i.e. solar energy, ultimately. The production of fuels and chemicals from renewable sources appears a promising way to store energy into value-added chemicals. Since renewable energy sources are often intermittent, their exploitation requires storage systems, ideally liquid chemicals that have high energy density. As the installed capacity of these sources increases, so do issues related to load-balancing and to temporal and geographical disparities between supply and demand. Implementation of quick-start systems for the consumption of excess renewable energies could play a role in resolving these issues. This has an incidental benefit in terms of the cost-effectiveness of the technology because the electricity generated during such periods of excess production is of relatively low cost. Plasma-based systems are ideally suited to this task due to low inertia, low investment costs, and no requirement for rare materials. At the same time reusing CO_2 is a key element for curbing green house gas (GHG) emissions [1].

NTPs have been explored for their capability to activate very stable molecules such as methane and carbon dioxide at low temperature. In fact NTP are able to reform CO_2 and CH_4 to get value-added chemicals. Depending on the particular experimental set-up and the specific operational features, different gaseous [2, 3], liquid [4, 5, 6] or solid chemicals [7] are produced by the discharge in addition to the most abundant products CO and H_2.

In our recent works [8, 9], our attempts to convert CO_2 and CH_4 in syngas (hydrogen and carbon monoxide) and other value-added chemicals are presented. We show that a partial control of the product selectivity can be achieved by modulating the electrical power delivered to the discharge[8]. In addition, we investigated the catalytic effect of the electrode surface on the production of oxygenate products[9]. The aim of our study was to

contribute to a better understanding of the fundamental processes involved. To this purpose, the product branching ratio must be known as a function of discharge parameters. However, if ones desire to investigate the detailed chemical mechanisms leading to the final products, knowledge of the latter is not sufficient, and intermediate, transient species, such as CH_3, H and OH, must be identified as they are chemical markers of specific reaction paths [10].

1.1.2 Plasma medicine

As outlined by Fridman in [11] "Plasma medicine embraces physics required to develop novel plasma discharges relevant for medical applications, medicine to apply the technology not only in vitro but also in vivo testing and, last but not least, biology to understand the complicated biochemical processes involved in plasma interaction with living tissues". Radicals, in particular O-atoms and OH, are effectively generated in atmospheric pressure discharges and they play a role in several plasma induced oxidation processes [12, 13]. For this reason radical diagnostics is a key point for the rapidly developing field of plasma medicine[14]. In addition, OH measurements in test cases are of interest for comparison to recent model calculations [15].

1.1.3 Plasma abatement of pollutant

Nowadays environmental protection is an important issue. Exhausts from mobile and stationary sources pollute the air with a variety of dangerous substances for the human health and the ecological life. Volatile organic compounds (VOCs) are an important group among these pollutants. VOCs play an important role at global level (global warming promoters), at regional scale (acid rain promoters), but especially at local scale, directly affecting human health given that several VOCs are carcinogens. Also in the everyday indoor environments, organic compounds can be detrimental for human health. NTPs offer interesting opportunities in the field of air-cleaning systems. There is a clear opportunity for NTP techniques to be employed for the activation and dissociation of the feedstock molecules[16]. Reactive oxygen species (ROS), such as O, OH, O_3, H_2O_2, HO_2 and $O_2(a^1\Delta_g)$, play an important role in pollutants remediation. Indeed, VOCs destruction mainly proceeds via oxidative reactions. Therefore any effective destruction method should maximise the amount

of oxidant species, and their quantitative detection is a critical issue to improve the performance.

1.2 Optical spectroscopy diagnostics of discharges at atmospheric pressure

Spectroscopic diagnostics are particularly suitable to estimate quantities such as gas temperature, electron density, electric field and density of transient species. The main optical diagnostic techniques are: optical emission spectroscopy (OES), laser induced fluorescence (LIF), and absorption spectroscopy (AS). OES is the simplest technique and thus it is widely used. Unfortunately, it provides information only about excited species, which depend in a complex and indirect way on the corresponding ground state populations. Molecules in their ground state can be instead detected either by AS or by LIF. AS is cheap, provides absolute outcomes, but its spatial and temporal resolution is low [17, 18].

Laser induced fluorescence (LIF) is the best technique if sensitivity, time and space resolution are a crucial requirement [19]. LIF, however, needs a calibration because the outcome is not absolute. In addition, the LIF signal depends on collisional processes of the excited state, and therefore a detailed model is necessary to rationalise the experimental outcomes.

Chapter 2

Time-resolved broad-band absorption spectroscopy

In absorption spectroscopy, the light radiation passes through the plasma, and the modification of the spectrum as a function of the wavelength of the incoming light by absorption and scattering is measured. Absorption spectroscopy is the technique of choice to get the absolute density of molecules in their ground state. When dealing with plasma-mediated processes, absorption can be achieved by simply using an incoherent broadband light source much brighter than the plasma itself, like broad-band xenon or deuterium lamps [20]. Unfortunately, not all the spectral regions can be covered by broadband sources. When no broadband light sources are available, *self-absorption* can be used. In this case the plasma itself can be used as source [21]. Resonant transitions can be also achieved by using tunable laser-based systems [22].

Various types of arrangements and techniques have been developed in the past years in the field of non-thermal atmospheric pressure plasmas or other similar environments (like flames or plasma activated flames), such as resonant absorption [17], broad-band absorption spectroscopy (BBAS) [18, 23], cavity enhanced absorption spectroscopy (CEAS) or cavity ring-down spectroscopy (CRDS) [24, 25, 26, 27]. An example of the application of absorption spectroscopy in plasma environments is the detection of CF_2 by using a Xe arc lamp as a light source in Ar/fluorocarbon mixtures [28]. As far as tunable laser diode absorption spectroscopy is concerned, Pipa *et al.* [29] measured NO density in an atmospheric pres-

sure plasma jet operating at 13.56 MHz in argon with small admixtures of air in a multi-pass cell. Ar$(1s_5)$ metastable density measurements were carried out by Belostotskiy *et al.* [30] in a pulsed dc argon micro-plasma discharge by using diode laser absorption spectroscopy. The populations of the excited Ar atoms were studied by Penache *et al.* [31] using diode laser atomic absorption spectroscopy. Also Niemi *et al.* [32] measured metastable He with the same technique.

In recent years the development of cheap, broad-band, very stable near-UV sources (UV-LED) has increased the interest for the BBAS technique. In fact, many radicals have strong electronic transition in the near-UV range. An example is the OH radical and its $A^2\Sigma^+ \leftarrow X^2\Pi$ transitions that were used by Dilecce *et al.* [18] and Bruggeman *et al.* [33] for absolute temperature and concentration measurements. In the following sections I describe our new attempt to improve the TR-BBAS technique [23].

2.1 Broad band absorption spectroscopy: principles and application to OH

2.1.1 Basics nomenclature in light-matter interaction

When molecules undergo an electronic transition between an upper level j and a lower level i, a spectral line is emitted. The wavelength λ_{ji} of the emitted line is proportional to the energy gap between the two levels:

$$\nu_{ji} = \frac{E_j - E_i}{h} \qquad \lambda_{ji} = \frac{c}{\nu_{ji}},$$

where c indicates the speed of light. If the transition is spontaneous the variation of the population of the upper level n_j is proportional to the population density and to the Einstein coefficient of spontaneous emission A_{ji}:

$$-\frac{dn_j}{dt} = A_{ji} n_j.$$

When the emission of photons is induced by the radiation, one gets

$$-\frac{dn_j}{dt} = B_{ji} \xi_\nu n_j.$$

The induced emission is proportional to the level population, the Einstein coefficient B_{ji} and to the spectral radiant energy density ξ_ν, like its inverse process, the absorption:

$$-\frac{dn_i}{dt} = B_{ij}\xi_\nu n_i. \tag{2.1}$$

The Einstein coefficients for absorption and induced emission are related by:

$$g_i B_{ij} = g_j B_{ji},$$

where g_i and g_j are the statistical weights of the lower and higher level, respectively.

2.1.2 Broad band absorption

The BBAS technique consists in the measurement of changes of the spectral radiance $I(x,\nu)$ induced by the absorption process along the optical path[20]. Radiation absorption within a media can be described by introducing a wavelength-dependent absorption coefficient $\kappa(x,\nu)$ defined as

$$dI(x,\nu) = -\kappa(x,\nu)I(x,\nu)\mathrm{d}x \tag{2.2}$$

that represents the variation of the spectral radiance $I(x,\nu)$ along the direction x by a thin slab dx of absorbing medium. The unit of $\kappa(x,\nu)$ is m^{-1} and the spectral radiance $I(x,\nu)$ unit is $\mathrm{W\,s^{-1}\,m^{-2}\,sr^{-1}}$. By the spatial integration of Eq. 2.2 along the length l (the optical path inside the discharge) one gets the well known Lambert-Beer law:

$$I\left(l,\nu\right) = I\left(0,\nu\right)\mathrm{e}^{-\int_0^l \kappa(x,\nu)\mathrm{d}x} \tag{2.3}$$

Given the central frequency of a certain transition ν_{ji}, the line absorption coefficient can be written as a function of the transition line shape function $\mathcal{L}(\nu-\nu_{ji})$, with its integral respect to the frequency normalised to one, and the integrated line absorption coefficient $\kappa^L(x,\nu_{ji})$:

$$\kappa_{ji}\left(x,\nu\right) = \kappa^L\left(x,\nu_{ji}\right)\mathcal{L}\left(\nu-\nu_{ji}\right), \qquad \int_{+\infty}^{-\infty}\mathcal{L}\left(\nu-\nu_{ji}\right)\mathrm{d}\nu = 1.$$

The integrated line absorption coefficient unit is $\mathrm{Hz\,m^{-1}}$. If we consider the spectral flux absorption in a plasma slab of thickness Δx defined in Eq. 2.1 and we multiply it by a factor

$h\xi_\nu$ it becomes equal to the right-hand side of Eq. 2.2 after the integration of the absorption coefficient $\kappa(x,\nu)$:

$$B_{ji}\xi_\nu\left(\nu_{ji}\right)n_j\Delta x h\nu_{ji} = I_\nu\left(\nu_{ji}\right)\Delta x\int_{+\infty}^{-\infty}\kappa(x,\nu-\nu_{ji})\mathrm{d}\nu$$
$$= \kappa^L\left(x,\nu_{ji}\right)I_\nu\left(\nu_{ji}\right)\Delta x.$$

Considering the case of collimated radiation, the radiance and the radiant energy density are related by

$$\xi\left(\nu\right) = \frac{1}{c}I\left(\nu\right),$$

changing the coefficients unit from frequency to wavelength one gets:

$$\kappa^L\left(x,\lambda_{ji}\right) = \frac{h\lambda_{ji}}{c}B_{ji}n_j.$$

Considering the cross-section σ_{ji} as the absorption coefficient divided by the density of the species in the lower state j we have

$$\sigma_{ji}(x,\lambda) = \frac{\kappa_{ji}\left(x,\lambda\right)}{N_j(x)} = \frac{\kappa^L\left(x,\lambda_{ji}\right)\mathcal{L}(\lambda-\lambda_{ji})}{N_j(x)} = \sigma_{ji}^L\mathcal{L}(\lambda-\lambda_{ji}).$$

Assuming that the spatial dependence is only in the $N_j(x)$ term, one gets

$$\sigma_{ji}^L \approx \frac{\kappa^L\left(\lambda_{ji}\right)}{N_j(x)} = \frac{h\lambda_{ji}}{c}B_{ji}. \tag{2.4}$$

The Lambert Beer law (Eq. 2.3) for a single molecular band with $N_j(x) = n_jN(x)$, where n_j is the fractional population of the rotational level involved in the transition j, becomes:

$$I_\lambda\left(l,\lambda\right) = I_\lambda\left(0,\lambda\right)\mathrm{e}^{-\int_0^l N(x)\mathrm{d}x\sum_j n_j\sigma_{ji}^L\mathcal{L}(\lambda-\lambda_{ji})}. \tag{2.5}$$

2.2 Time-resolved broad-band absorption spectroscopy experimental set-up

The TRBBAS set-up is composed of two main parts: the broad-band light source and the light detection system.

2.2.1 Light Source

The light source used to probe the OH molecule is a UV-LED (UVTOP-310-TO39-BL, SET) with a peak-emission wavelength at $3089\,\text{Å}$ and a full width at half maximum (FWHM) of $89\,\text{Å}$ (Figure 2.1). The UV-LED is housed in a TO-39 package and equipped with a ball lens with a focal length of $\approx 18\,\text{mm}$. The maximum LED forward current in cw mode is $30\,\text{mA}$, but it can be increased to $200\,\text{mA}$ in pulse mode (at $1\,\text{kHz}$, 1% duty cycle).

To inject the UV-light into the discharge gap it is crucial to collimate the LED radiation. A good collimation permits a multiple pass configuration and the possibility to add a spatial

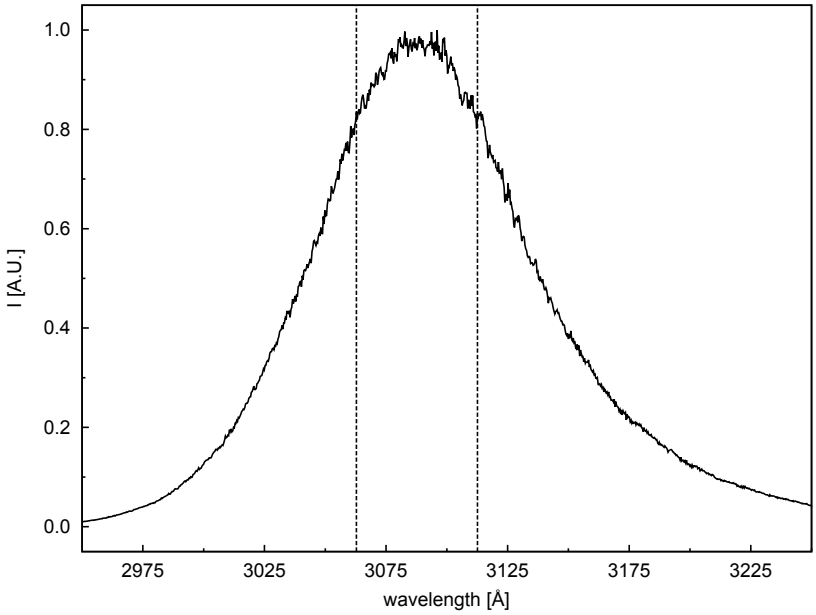

Figure 2.1: Measured spectral profile of the UVTOP-310-TO39-BL (SET) UV-LED. The vertical lines set the range of OH absorption.

filter after the discharge to decrease the amount of spontaneous emission radiation reaching the detector. Unfortunately, the LED is not a point-source of light, and the quality of the beam obtained using a single-lens collimation system is poor, i.e. the beam remains well collimated only over a short distance (in the order of $\approx 100 - 200\,\text{mm}$ [18]). In this condition, it is possible to get only a single-pass configuration through the discharge area (that is $35\,\text{mm}$ wide). On the other hand, the rejection of the spontaneous emission is achieved by putting one or more irises between the plasma and the detector. A proper rejection of

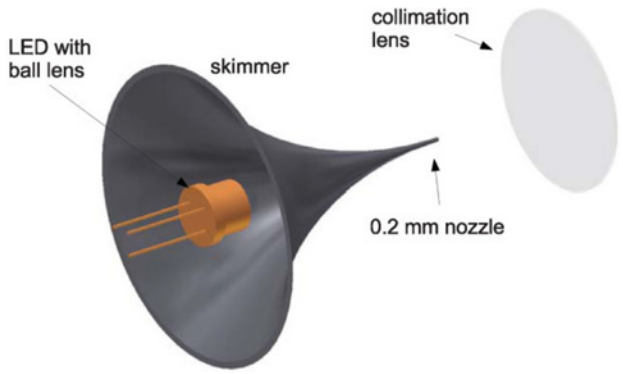

Figure 2.2: Scheme of the LED collimation arrangement. The LED has a ball lens on top. The skimmer is made of polished nickel; its internal walls are partially reflective. The 200 µm nozzle of the skimmer acts as a small size source allowing a good collimation by the 50 mm focal length collimation lens [23]

the spontaneous emission with spatial filters requires putting the detector centimetres away from the discharge. Increasing the beam collimation corresponds to a significant increase of the spontaneous emission rejection, as well as the possibility to lengthen the optical path inside the plasma.

The solution adopted is presented in Figure 2.2, where we put the UV-LED inside a skimmer made of polished nickel. The skimmer's walls help to *canalise* the UV-light to the 200 µm exit bore that is placed in correspondence of the LED ball lens focal point. A $f = 50$ mm lens is used to collimate the light exiting from the nozzle. The resulting beam remains well collimated for a distance of ≈ 500 mm with a section in the order of $1 - 2\,\text{mm}^2$. Thanks to the better beam collimation we could adopt a two-pass configuration inside the discharge and we could add two irises in order to spatially filter the spontaneous emission. Of course the disadvantage is that an increasing beam collimation decreases the beam intensity.

Figure 2.3 shows the schematic representation the TR-BBAS apparatus. The light travels inside the discharge area perpendicular to the gas flux. The total absorption length is 70 mm The UV-LED driver is an home-made gateable current source circuit made of fast JFET transistors, with a maximum output current of 160 mA and a minimum gate time of 500 ns. The UV-LED gate trigger is generated by a waveform generator (33250A, Agilent).

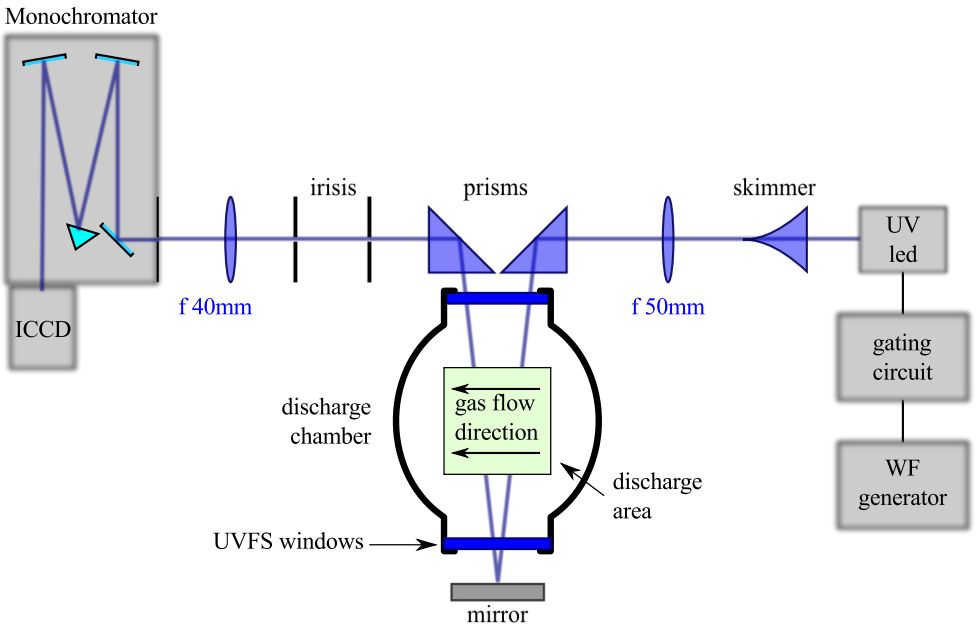

Figure 2.3: Schematic representation of TR-BBAS apparatus. The UV-LED beam is injected in the discharge area with a double pass configuration. Irises serve as spatial filters in order to stop the spontaneous emission emitted by the discharge. The $f = 40\,\text{mm}$ lens matches the incoming UV-beam to the f-number of the monochromator.

2.2.2 Light Detectors

The first detection setup D1 is based on a 140 mm focal length monochromator (microHR, Jobin-Yvon) equipped with a 1200 gr mm^{-1} 300 nm blaze grating with a 100 µm input slit. The light detector is a charge coupled device (CCD) (GARRY 3000, Ames Photonics). This device is non-cooled, non-intensified, gateable 3000 elements linear CCD array. The second detection setup D2 is composed of a 300 mm focal length monochromator (Shamrock 303i, Andor) equipped with a 1200 gr mm^{-1} 300 nm blaze grating, 70 µm input slit. The detector coupled to the Shamrock 303i is a cooled, 1024×1024 pixel, intensified CCD (ICCD) (DH334T-18U-03, Andor).

2.2.3 Discharge Design

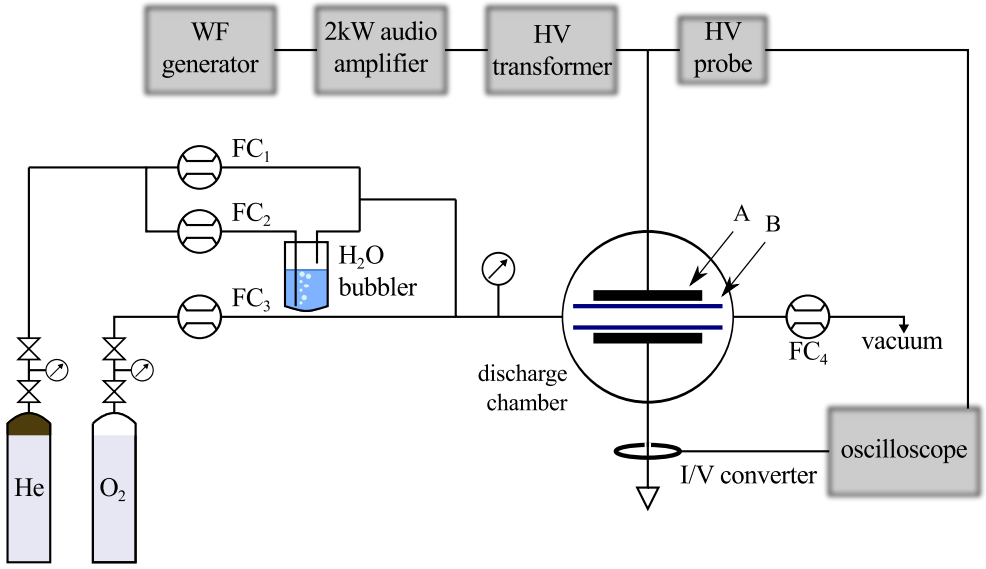

Figure 2.4: Schematic representation of the DBD set-up. FC_{1-4}: mass flow controllers; A: 35×35 mm^2 copper electrodes; B: 0.7 mm thick alumina plates.

A schematic representation of the discharge gas feed and electrical apparatus is shown in Figure 2.4. The discharge set-up is composed of two main components, the plasma power supply, the monitoring system and the discharge chamber gas feed lines controller.

Discharge configuration and gas feed

The dielectric barrier discharge used is a parallel plate configuration composed of $35 \times 35\,\mathrm{mm}^2$ copper electrodes. Two 0.7 mm thick alumina plates are used as dielectric barriers. Two inter-electrode gaps have been used (4.5 mm and 2.0 mm). With these two configurations the electrode surface is $12.25\,\mathrm{cm}^2$ and the discharge volume $5.50\,\mathrm{cm}^3$ and $2.45\,\mathrm{cm}^3$ for 4.5 mm and 2.0 mm, respectively. The discharge gas feed is composed of three separate gas lines: a pure He (99.995% purity) carrier controlled by a 1000 sccm full scale mass flow controller FC_1 (1179B, MKS); a pure He (99.995% purity) flow injected in a bubbler filled with distilled water, whose temperature is measured with a type *K* thermocouple, controlled by a 500 sccm full scale mass flow controller FC_2 (1179A, MKS); and a pure O_2 (99.995% purity) line controlled by a 10 sccm full scale mass flow controller FC_3 (1179A, MKS). Another 5000 sccm full scale mass flow controller FC_4 (1179A, MKS) is placed in between the discharge chamber and the $4\,\mathrm{m}^3\,\mathrm{h}^{-1}$ membrane pump. Thanks to FC_4 the pressure inside the discharge chamber is kept at a constant value 20 torr above atmospheric pressure, in order to prevent air to penetrate inside the discharge chamber. The water partial pressure inside the discharge chamber is described by the equation:

$$P_{H_2O} = P^{vap}_{H_2O}(T)\,\frac{\phi_2}{\phi_1+\phi_2+\phi_3},$$

where $P^{vap}_{H_2O}(T)$ is the water vapour pressure at the temperature T, ϕ_1 is the flux of the He carrier, ϕ_2 is the He flux injected in the bubbler and ϕ_3 is the O_2 flux, as described in [34, 35]. The total flux injected into the discharge chamber is kept at a constant value of 500 sccm during measurements. Mass flow controllers are driven by a computer controllable multi-gas controller (647B, MKS).

Power supply and electrical diagnostic

The high-voltage (HV) power supply is composed of a wave form generator (33220A, Agilent) that generates a sinusoidal signal amplified by a 2 kW bridged class-D audio amplifier (UCD2k OEM, Hypex). The amplified low-voltage signal is converted in a HV stimulus V_s by using a HV transformer (Al-T1000.7-P10, Amp-Line). The secondary coil of the HV transformer is connected to the parallel between one electrode of the reactor and

a HV high bandwidth (DC - 75 MHz) probe (P6015A, Tektronix) that is used as a voltage monitor. The second discharge electrode is connected directly to the ground and a high bandwidth (200 Hz - 500 MHz) I/V converter (CT-01-b, Magnelab) is placed around the wire that connects the reactor to the ground. Signals acquired by the voltage and current probes are digitalised and recorded by a four-channel 4 GSps 600 MHz bandwidth digital signal oscilloscope (DSO) (Infiniium 54831B, Agilent).

2.2.4 PC based control program

I wrote a program by using LabWindows/CVI (National Instruments) to control the discharge gas feed apparatus, plasma power supply and to record the spectrum acquired by the CCD/ICCD. A schematic representation of the connection between the apparatus and the PC is presented in Figure 2.5. The program initialises the waveform generators in order to

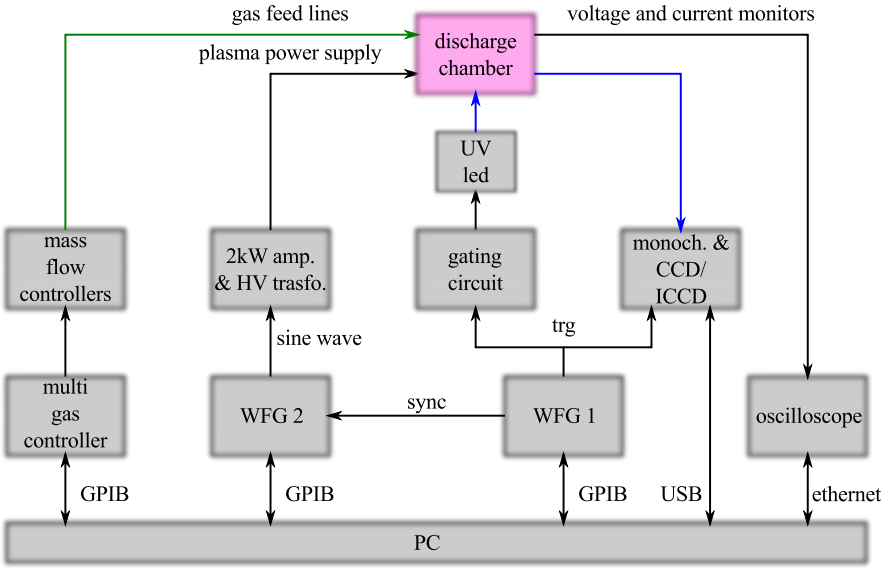

Figure 2.5: Schematic representation of the pc-based control system. WFG 1-2: waveform generators synchronised in frequency and phase by sharing the 10 MHz external time-base reference. Black lines: analog and digital signals; Blue lines: UV-LED light signal; Green line: gas feed connection.

generate the gates for the UV-LED and for the detector, sets amplitude, frequency and duty cycle of the sinusoidal signal that drives the discharge. For every mixture of $He-O_2-H_2O$, the PC sets the mass flow controllers and records the temperature inside the bubbler and the

pressure inside the discharge chamber. Absorption measurement requires the acquisition of the light generated by the UV-LED interacting with the discharge. In order to avoid the influence of the light source fluctuations or changes in the external light background, each acquisition of an absorption spectrum is followed by that of the UV-LED light signal, i.e. with the plasma switched off. Several spectra were taken in order to increase the statistics and to achieve a better detection limit.

2.3 Measurement strategy

The transitions involved in the absorption belong to the (0,0) band of the OH 3064 Å system, $A^2\Sigma^+ \leftarrow X^2\Pi$. In order to eliminate measurement baseline drift, LED low-frequency intensity fluctuations, and to reduce as much as possible the spontaneous emission from the plasma, we adopted a time-resolved detection strategy for the TR-BBAS. The timing

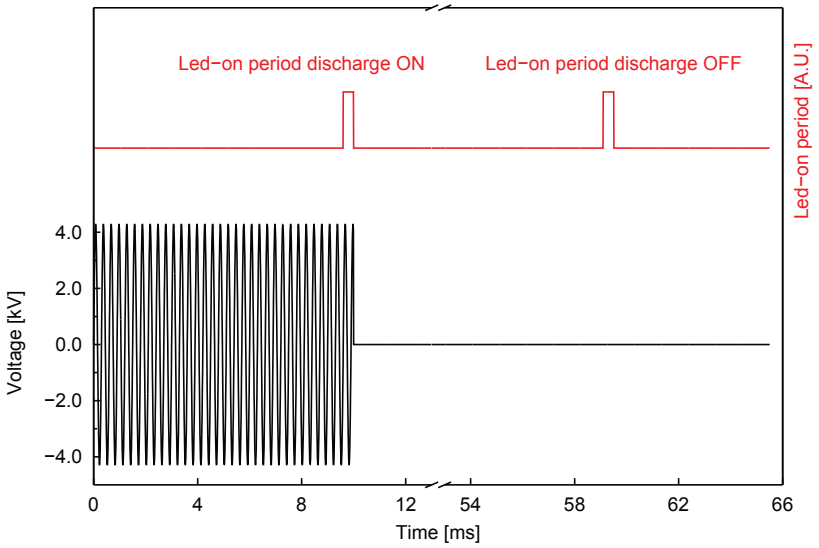

Figure 2.6: Red line: CCD/ICCD gate and LED pulsing for the TR-BBAS scheme, Led-on period discharge OFF provides the reference (without absorption) light intensity. Black line: sinusoidal stimulus applied to the discharge.

scheme of a TR-BBAS experiment is shown in Figure 2.6. We modulate the sinusoidal voltage of the discharge with a square wave, generating a burst of 200 20 kHz sine waves.

During the sine wave burst, the plasma switches on (the duration of the burst is defined by the number of burst times the period of the sine wave $T_{ON} = 10\,\text{ms}$). After the burst of sine waves, the waveform generator output goes to zero for a time $T_{OFF} = 90\,\text{ms}$, and consequently the plasma switches off. The sum of T_{ON} and T_{OFF} defines the total period T of the on-off cycle, which is $T = 100\,\text{ms}$. The OH concentration is probed by acquiring the absorption spectrum $I_\lambda^M(l,\lambda)$ at the end of the T_{ON} period, for a total duration of $T_{LED}^{ON} = 300\,\mu\text{s}$ (the same gate was applied to the UV-LED driver and to the CCD-ICCD gate). A further acquisition is carried out $50\,\text{ms}$ after the first one in order to record the LED profile $I_\lambda^M(0,\lambda)$ when the [OH] becomes negligible[34, 35, 18]. The resulting gate sequence is a combination of the sine-wave burst at $10\,\text{Hz}$ and the LED/detector-gate at $20\,\text{Hz}$. Gates are generated by two waveform generators, whose synchronisation is ensured by sharing the $10\,\text{MHz}$ external time-base reference. In this way, the two devices are synchronised in phase and frequency.

The gate configuration just described was used in conjunction with the D1 scheme based on the non-cooled, non-intensified, gateable linear CCD array. In this case, the spontaneous emission rejection was achieved by using spatial filters (irises) placed in between the discharge area and the monochromator. The rejection of the spontaneous emission can be further increased by using the improved detection scheme D2, which is based on the synchronisation of the ICCD acquisition with respect to the periodical null value of the discharge current (see Figure 2.8), i.e. when the spontaneous emission is minimal. For comparison, in the scheme D1, the signal is acquired continuously during the LED gate, i.e. for each value of current.

Spontaneous emission is detrimental for BBAS because, in many cases, it is much more intense than the absorption signal. Besides the OH concentration value, it can also affect the temperature estimate. We notice that the spontaneous emission is generated by the $A^2\Sigma^+(\upsilon=0) \rightarrow X^2\Pi(\upsilon=0)$ band, that is the same interested by the absorption $A^2\Sigma^+(\upsilon=0) \leftarrow X^2\Pi(\upsilon=0)$. Bruggeman *et al.* in [33] proposed to calculate the absorption spectrum of OH subtracting the spontaneous emission from the transmitted LED light (which of course contains also the plasma spontaneous emission). However, if the emission is much larger than the absorption, the estimation of the transmittance is affected

by a strong systematic error. For these reasons, we chose alternative strategies in order to decrease the incidence of spontaneous emission in the measurement:

- using light sources with an adequate radiant energy density, much larger than the spontaneous emission. In this way, it is possible to adopt short CCD gates and in turn to acquire less spontaneous emission radiation.

- rejecting the spontaneous emission that travels from the discharge to the detector by stopping all the radiation that is not collimated with the UV-LED beam.

- adopting a multi-pass strategy to increase the optical path, i.e. the absorbance signal.

Finally, we emphasise the importance of the light source that has to be gateable and well collimable.

During the T_{ON} period the spontaneous emission intensity is not constant, and it follows the time dependence of the voltage. We measure the spontaneous emission intensity versus time using the D2 configuration. The gate scheme is equal that presented in Figure 2.6, but the LED is always kept in the off state. In this way, during T_{ON} the spontaneous emission plus background is recorded $I_{\lambda}^{SE}(\lambda)$, and during T_{OFF} only background light $I_{\lambda}^{BG}(\lambda)$ is acquired. We used a 5 µs gate for the ICCD. $I_{\lambda}^{SE}(\lambda)$ and $I_{\lambda}^{BG}(\lambda)$ are obtained by averaging 2000 single ICCD acquisitions. The integral respect to the wavelength of

$$I_{SE}(\lambda) = I_{\lambda}^{SE}(\lambda) - I_{\lambda}^{BG}(\lambda),$$

is used to quantify the spontaneous emission intensity. The results, taken at various delay times with respect to the excitation voltage, are presented in Figure 2.7. The spontaneous emission reaches the maximum value when the current flowing inside the discharge is at its largest values. On the other hand, when the current is zero, the spontaneous emission is negligible (that happens two times every excitation voltage period). The spontaneous emission is related to exited OH molecules that are generated by the plasma when the current increases rapidly inside the voltage excitation period. These excited molecules decay radiatively to the ground state rapidly inside a V_s semi-period, while the ground state [OH] is expected to remain constant [35]. Starting from the experimental observation of the time

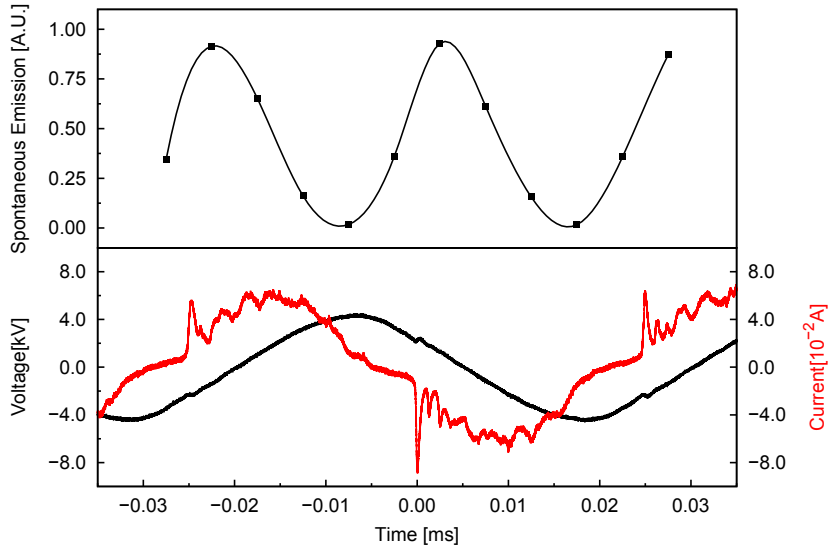

Figure 2.7: Top: $\int_{\lambda_{min}}^{\lambda_{max}} I_{SE}(\lambda)\, d\lambda$ in function of time, points are interpolated with a spline. Bottom: current (red line) and voltage (black line) in function of time.

dependence of the spontaneous emission, we decided to improve the spontaneous emission rejection only by changing the gates sequence of the acquisition.

The image intensifier (multi-channel plate, MCP) coupled with a cooled CCD, permits to use the MCP as an electrical shutter. Taking advantage of the *integration on chip* (IOC) function of the ICCD, we realised the possibility to gate the MCP several times during a single CCD acquisition. In this way, it is possible to sample $I_\lambda^M(l,\lambda)$ when the spontaneous emission is negligible, for a $10\,\mu s$ time interval immediately before the discharge current increases. During the following $15\,\mu s$, the MCP is switched off, thus avoiding to detect the spontaneous emission ($25\,\mu s$ is a V_s semi-period). The CCD signals ($I_\lambda^M(l,\lambda)$ and $I_\lambda^M(0,\lambda)$) are then acquired by switching the MCP on and off 14 times during a single $400\,\mu s$ CCD-LED gate. A representation of the CCD-LED and MCP gates together with the I-V characteristic of the discharge are shown in Figure 2.8. The resulting effective gate time for the signal acquisition decreases from $300\,\mu s$ in the case of detection system D1 to $140\,\mu s$ in the case of D2, at the expense of the signal to noise ratio. A comparison between the $I_{SE}(\lambda)$ values acquired with and without the MCP gating is presented in Figure 2.9. The new MCP gating strategy reduces the spontaneous emission by about a factor four.

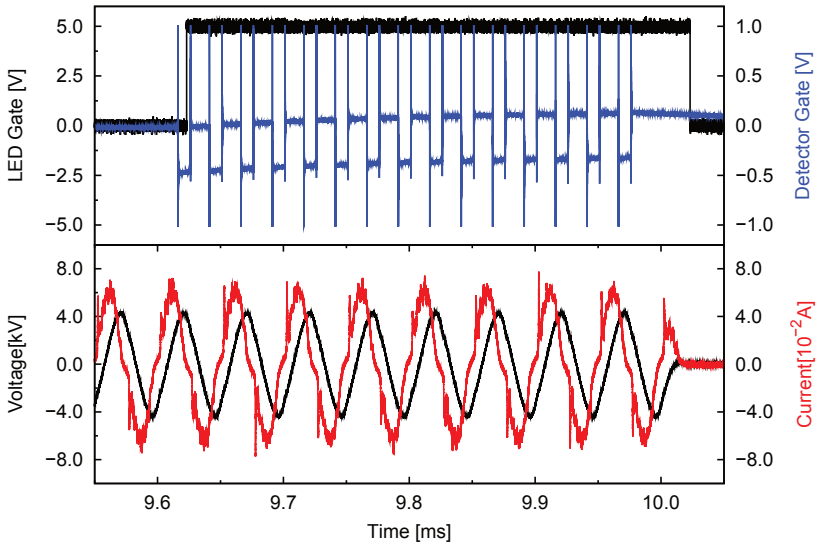

Figure 2.8: Top: Detail of the gating at the end of the discharge packet, the MCP gating (blue line) is for detection system D2 only. It is open (negative level) in the null discharge current intervals. The black line is the LED-CCD gate. Bottom: current (red line) and voltage (black line) in function of time.

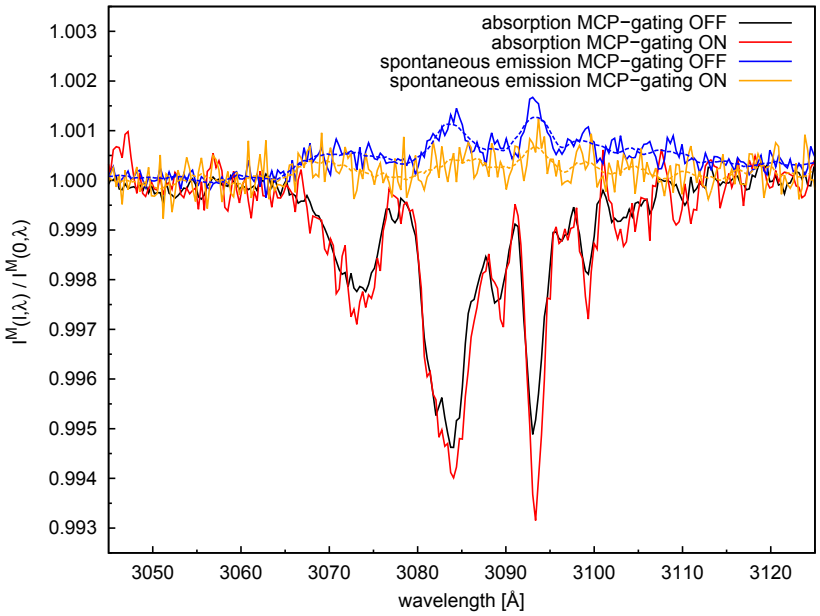

Figure 2.9: Spontaneous emission (blue line) and transmittance spectrum (black line) in function of wavelength for the spatial filtering strategy. The red and yellow lines are the transmittance spectrum and the spontaneous emission, respectively, for the spatial filtering plus MCP gating strategy. Dashed lines are smoothed spontaneous emission profiles. Measurements were taken using detection system D2.

However, although effective in the case of the OH detection in a DBD, this strategy cannot be applied in general, in particular either to short living molecule or discharges where the excitation period is short compared to the life time of the states responsible of spontaneous emission.

For both the measurement configurations, (in order to decrease the measurement noise) the quantities $I_\lambda^M(l,\lambda)$ and $I_\lambda^M(0,\lambda)$ are obtained by averaging 10000 gate CCD signals.

2.3.1 Fit of the experimental data

Our experiment is based on transitions of the 3064 Å system $(0,0)$ band. The outcomes are values of the spectral radiance when the discharge is on and off, $I_\lambda^M(l,\lambda)$ and $I_\lambda^M(0,\lambda)$, respectively. These two quantities and the modelled spectral radiance $I_\lambda(l,\lambda)$ (Eq. 2.5) are related by the equations

$$I_\lambda^M(l,\lambda) = \int_{-\infty}^{+\infty} I_\lambda(l,\lambda')\mathcal{S}(\lambda'-\lambda)\mathrm{d}\lambda', \tag{2.6}$$

$$I_\lambda^M(0,\lambda) = \int_{-\infty}^{+\infty} I_\lambda(0,\lambda')\mathcal{S}(\lambda'-\lambda)\mathrm{d}\lambda', \tag{2.7}$$

where $\mathcal{S}(\lambda)$ is the spectrometer instrumental function, that of course is different for the two detection systems. In the case of the second detection setup D2, the instrumental function is presented in Figure 2.10. The instrumental function was recorded by putting a He−Ne calibration lamp (6034, Newport) in front of the spectrometer slit entrance. The optimum slit width was chosen in order to have the maximum signal to noise ratio with a good spectral resolution [18]. The entrance input slit widths used were $100\,\mu$m and $70\,\mu$m in the case of detection setup D1 and D2, respectively. The transmittance spectrum is defined as the ratio between the spectral radiance in the discharge-on condition (Eq. 2.6) and the spectral radiance in the discharge-off condition (Eq. 2.7).

$$\frac{I_\lambda^M(l,\lambda)}{I_\lambda^M(0,\lambda)} = \int_{-\infty}^{+\infty} \mathrm{e}^{-lN_{ave}\sum_i n_i\sigma_i^L\mathcal{L}(\lambda'-\lambda_i)}\mathcal{S}^N(\lambda'-\lambda)\mathrm{d}\lambda'. \tag{2.8}$$

In the limit of a *narrow instrumental function*, i.e. narrow with respect to the wavelength dependence of the light source, $I_\lambda(0,\lambda)$ can be brought out of the integral sign in Eq. 2.8. The term N_{ave} refers to the average particles density along optical path ($l = 70$ mm)

$$N_{ave} = \frac{1}{l}\int_0^l N(x)\mathrm{d}x,$$

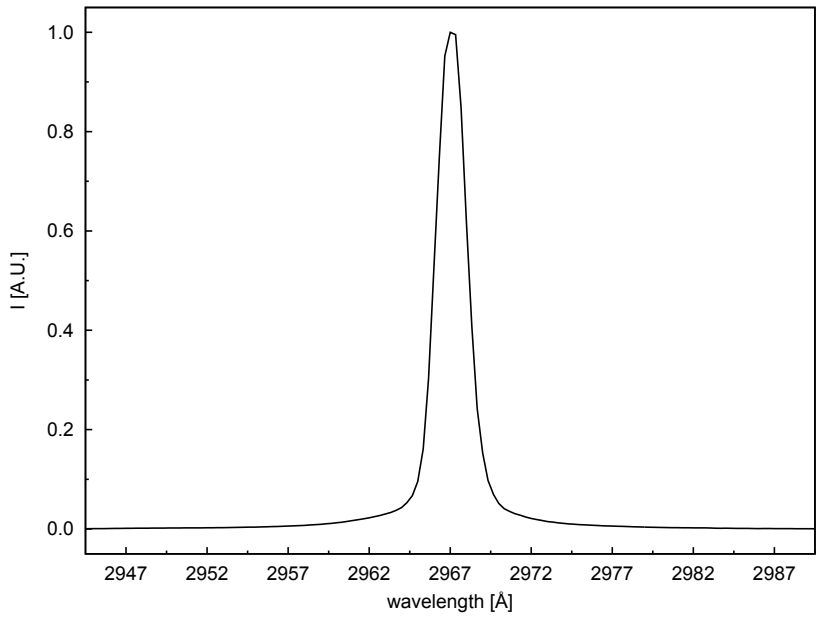

Figure 2.10: Detection system D2 instrumental function for a 70 µm input slit width.

and $\mathcal{S}^N(\lambda)$ is the normalised instrumental function of the spectrometer

$$\mathcal{S}^N(\lambda) = \frac{\mathcal{S}(\lambda)}{\int_{-\infty}^{+\infty} \mathcal{S}(\lambda)\mathrm{d}\lambda}.$$

The terms $n_i\sigma_i^L\mathcal{L}(\lambda - \lambda_i)$ in the sum over the i transitions of the $(0,0)$ band are calculated starting from the LIFBASE spectral simulation program [36]. Given a certain temperature and line shape function, LIFBASE calculates a spectrum normalised to the peak absorption line (only proportional to $n_i\sigma_i^L\mathcal{L}(\lambda-\lambda_i)$). The line shape function used in our simulations is given by a Doppler plus pressure broadening profile (Figure 2.11). The pressure broadening is taken from [37], and its value of $3.5\,\mathrm{GHz\,atm^{-1}}$ at $298\,\mathrm{K}$ is assumed to be the same for all rotational levels.

Starting from a set of simulated transition spectra, corresponding to various temperatures, and by comparing them with the experimental data, it is possible to estimate the absolute mean concentration of OH radical along the optical path.

We wrote a C program that fits Eq. 2.8 on the experimental data. An example of the measured transmittance $T^M(\lambda) = \frac{I_\lambda^M(l,\lambda)}{I_\lambda^M(0,\lambda)}$ is shown in Figure 2.12. It is visible an anomalous negative baseline that deviates from the expected value of a transmittance spectra (equal to 1). This anomalous baseline is probably due to a change in the refractive index of

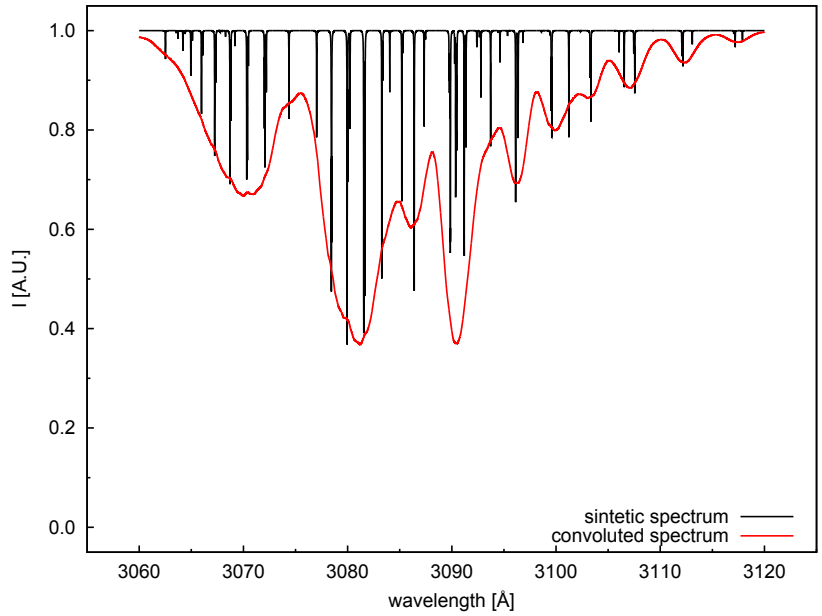

Figure 2.11: Black line: simulated transmittance spectrum, the line shape function is given by a Doppler plus pressure broadening profile. Red line: simulated transmittance spectrum convoluted with the instrumental function of detection system D2.

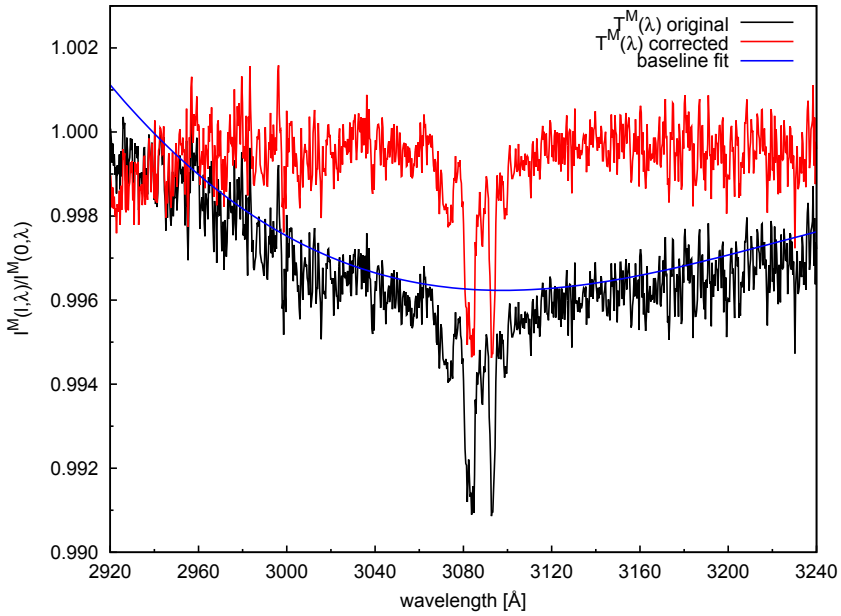

Figure 2.12: Black line: experimental transmittance spectrum. Blue line: baseline best fit of a 4^{th} order polynomial function. Red line: experimental transmittance spectrum after baseline subtraction.

the media along the optical path during the plasma-on condition, which in turn creates an anomalous transmittance signal. A change in the refractive index of the medium corresponds to a shift in the wavelength of the UV-LED profile. In order to eliminate this spurious effect we fitted the baseline with a 4^{th} order polynomial function (the blue line in Figure 2.12) and we subtracted it from the experimental transmittance. The result is the red graph in Figure 2.12 where only the transmittance spectra of the $A^2\Sigma^+\,(\upsilon = 0) \leftarrow X^2\Pi\,(\upsilon = 0)$ band is present.

We then re-normalise the LIFBASE spectrum to the value required in Eq. 2.8 by taking an isolated line, the $P_1(2)$ one, and normalising its spectral integral to $n_{(N=2,\ F_{1e})}\sigma^L_{P_1(2)}$, using formula Eq. 2.4 with the absorption coefficient taken from LIFBASE database. $n_{(N=2,\ F_{1e})}$ is the population of the rotational sublevel $N = 2$, F_{1e} ($J = 2.5$), parity e at a given rotational temperature [18, 38] (see Appendix B for the nomenclature of transitions and rotational levels).

Given a OH density value, all the $n_i\sigma_i^L\mathcal{L}(\lambda - \lambda_i)$ transitions of the (0,0) band were multiplied by the average OH density and the optical path length. After computing the exponential term inside the integral of Eq. 2.8 we calculated the circular convolution with the monochromator instrumental function. In order to estimate the right value of the OH concentration all these calculation were carried out using a multidimensional nonlinear last-squares fitting tool written using the GNU Scientific Library [39]. After the baseline subtraction, 150 points of the experimental transmittance spectrum were used to fit the model of Eq. 2.8 to the experimental spectrum. This allows us to estimate N_{ave} (the OH density) and the wavelength offset ω_o between the experimental data and the model. The program minimises the squared residuals of the $n = 150$ functions f_i via the parameters N_{ave} and ω_o

$$\begin{aligned}\Phi\left(N_{ave},\omega_0\right) &= \frac{1}{2}\|F\left(N_{ave},\omega_0\right)\|^2 = \\ &= \frac{1}{2}\chi^2 = \frac{1}{2}\sum_{i=1}^{n}\frac{\left(T\left(N_{ave},\omega_0,\lambda_i\right) - T^M\left(\lambda_i\right)\right)^2}{\sigma_i^2},\end{aligned} \tag{2.9}$$

where σ_i are the errors associated with each of the 150 points of the transmittance spectrum $T^M\left(\lambda_i\right)$. We estimated the errors by acquiring the spectrum $T^M\left(\lambda_i\right)$ with the plasma off condition. In this way the expected transmittance spectrum is a constant equal to one. In

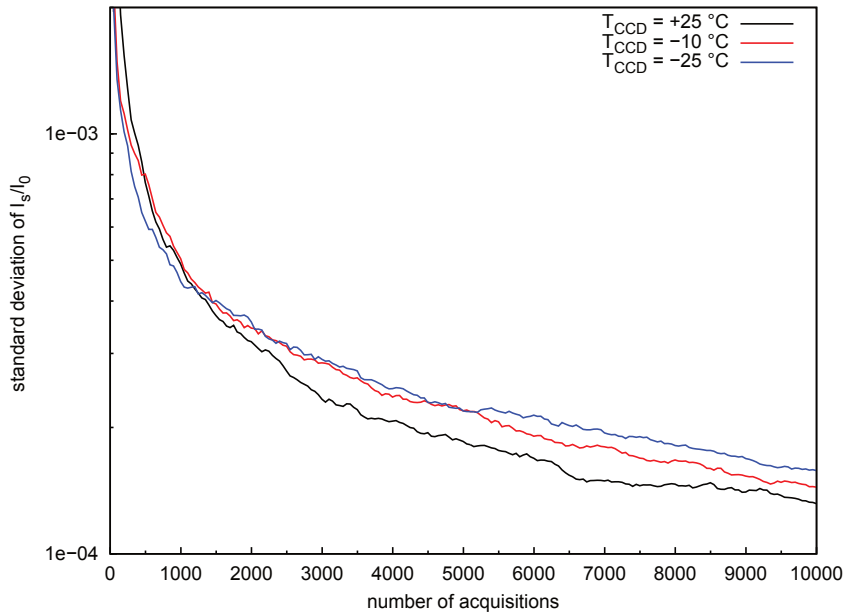

Figure 2.13: Standard deviation of 150 points of the experimental spectrum in function of the number of the CCD acquisition. Measurements were taken using detection system D2, keeping the discharge always in the off-condition, at three different CCD temperatures.

Figure 2.13, the standard deviation of the $n = 150$ points used to fit the experimental plot is presented as a function of the number of acquisitions of $T^M(\lambda_i)$ (i.e. for every acquisition of $I_\lambda^M(l,\lambda)$ and $I_\lambda^M(0,\lambda)$) carried out with detector scheme D2 (300 µs CCD and MCP gate). We computed the standard deviation for three temperature values of the CCD, which works in a quasi-saturated regime. Figure 2.13 shows that for achieving a lower uncertainty in the transmittance spectrum, the CCD has to be kept at room temperature or even higher temperatures. We decided to set the temperature of the CCD to $T_{CCD} = 15\,°\text{C}$. In this condition, the standard deviation of the 150 points is around 1.5×10^{-4} after averaging 10000 T^M measurements. We decided to associate to every measured point of the transmittance spectrum an error equal to $3 \times \sigma_i \approx 5 \times 10^{-4}$. The fitting program starts from initial guesses for OH density N_{ave}^0, and the wavelength offset ω_0^0. Then it evaluates the term:

$$\phi\left(N_{ave}^p, \omega_0^p\right) = \| F\left(N_{ave}^0 + N_{ave}^p, \omega_0^0 + \omega_0^p\right) \| \approx$$
$$\approx \| F\left(N_{ave}^0, \omega_0^0\right) + J\left(N_{ave}^p, \omega_0^p\right) \|$$

where N_{ave}^{p} and ω_0^p are the proposed steps, and $J\left(N_{ave}^{p}, \omega_0^p\right)$ is the Jacobian defined as:

$$J_{ij}\left(N_{ave}^{p}, \omega_0^p\right) = \frac{1}{\sigma_i} \frac{\partial\left(T\left(N_{ave}, \omega_0, \lambda_i\right)\right)}{\partial x_j}.$$

In the Jacobian, x_j are the parameters to be fit, and the algorithm tries to minimise the linear system $\| F\left(N_{ave}^{0}, \omega_0^0\right) + J\left(N_{ave}^{p}, \omega_0^p\right) \|$ using the Levenberg-Marquardt [40]. The terms of the jacobian matrix are computed numerically using a two-point numerical derivative. Best fit parameter errors are inferred from the covariance matrix. Figure 2.14 shows an example

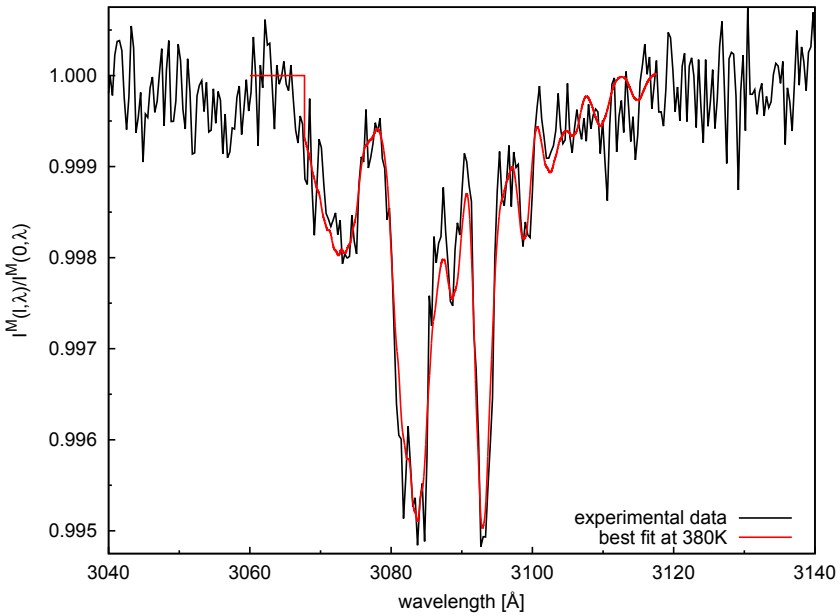

Figure 2.14: Absorption spectrum in the 2 mm gap discharge with $[H2O] = 0.56\%$, no added oxygen. $I_M(l, \lambda)$ is measured at the end of the discharge packet, and $I_M(0, \lambda)$ is measured in the post-packet. The best fit simulated spectrum is at a gas and rotational temperature of 380 K and at OH density of $6.62 \times 10^{13}\,\mathrm{cm}^{-3}$

of experimental transmittance spectrum fitted with the algorithm. In order to find the best temperature that fits the experimental spectrum, the multidimensional nonlinear last-squares fit is computed for a set of temperature (i.e. synthetic spectra). The best temperature (and associated OH density and wavelength offset) is the one that minimises the $\tilde{\chi}^2$, defined as in Eq. 2.9, but with the sum restricted to two 1 Å wavelength intervals centred on the two local minima of the transmittance spectrum (3083 Å and 3093 Å, Figure 2.14), respectively. These are the regions that are more sensitive to temperature changes. The temperature T^f of

the trial set that minimises $\tilde{\chi}^2$ and the associated N_{ave}^f and ω_0^f are the best fitting parameters.

2.3.2 Errors and the lower detection limit

As reported in [18] the errors related to the density estimate are: 4% due to a ± 20 K temperature uncertainty, 5% caused by the optical length uncertainty, 6% error due to the absorption coefficients. The statistical error associated with fit, given by the covariance matrix, is around 6%. The final uncertainty of the absolute density value is about 20%. The lower detection limit is the OH density that corresponds to an absorption spectrum with an amplitude equal to the noise amplitude. In our case its value is 9×10^{12} cm^{-3}.

Chapter 3

Laser induced fluorescence

In classical absorption spectroscopy, radiant sources with a broad band emission spectrum are used. As reported in Chapter 2, the absorption spectrum is obtained by comparison of the transmitted light inside the absorptive media with the reference light beam. The spectral resolution is limited by the resolution power of dispersing spectrometer. The detection sensitivity (the minimum absorbed power which can still be detected) is limited by the detector noise, light source fluctuation or change in the refractive index of the medium. The limit is generally reached at relative absorption $\frac{\Delta I_\lambda^M(l,\lambda)}{I_\lambda^M(0,\lambda)} \approx 10^{-5}$. More sensitive detection methods were developed in the past, thanks to the introduction of tunable lasers. In order to overcome the sensitivity limits connected to the measurement of a small difference between two large quantities, it is more convenient to detect directly the absorbed energy. The latter can either be converted into fluorescence energy and recorded by a fluorescence detection system (*laser-induced fluorescence* or *excitation spectroscopy*), or it can be converted by collisions into thermal energy with a consequent temperature and pressure rise, which can be detected by a microphone (*photoacustic spectroscopy*). Other spectroscopy techniques are based on the dependence of laser-intensity on absorption losses that happen inside the laser resonator (*intracavity laser absorption*) [22, 41].

A LIF measurement relies on atomic or molecular excitation by laser radiation, and on the observation of the resulting spontaneous emission from the exited state or from the nearby states that have been populated by collisions. Although LIF is not a scattering process (because radiation is absorbed by atoms or molecules and then the fluorescence is

observed due to the spontaneous emission of the exited species), it is useful to introduce the concept of scattering in order to compare LIF with other techniques that are based on light scattering. If we consider the *cross section* of the LIF phenomena, it is several orders of magnitude larger than Rayleight and Thomson scattering [42]. Like scattering processes, LIF signals can be observed with very high spatial resolutions without the needs of optical or acoustic cavities (like *intracavity laser absorption* or *photoacustic spectroscopy*). From a time dependent view, thanks to the use of pulsed lasers, the time resolution of LIF is essentially limited by the duration of the laser pulse.

3.1 Literature overview

Atmospheric pressure discharge applications, like plasma medicine and plasma assisted combustion, deal with a gas stream with some degree of humidity. OH radical is readily formed and, it being the most reactive oxidizing species, its amount in the discharge is a relevant parameter. Many papers have been recently published on OH quantitative detection by LIF: in a pulsed corona discharge [43, 44, 45, 46, 47], in a DBD [48], in a pulsed DBD [18, 34, 49], in a plasma-jet [50, 51, 52, 53, 54, 55, 56], in a pulsed discharge over a liquid surface [46], in a pin-to-pin single filament discharge [57, 58, 59], in a nanosecond H_2-air plasma for plasma assisted combustion at $50 - 100$ torr [60].

Excitation transitions commonly used in LIF spectroscopic of OH radicals are 1) $A^2\Sigma^+ (\upsilon = 3) \leftarrow X^2\Pi (\upsilon = 0)$ around $2480\,\text{Å}$ [43, 47], the 2) $A^2\Sigma^+ (\upsilon = 1) \leftarrow X^2\Pi (\upsilon = 0)$ around $2820\,\text{Å}$ [48, 18, 57] or the 3) $A^2\Sigma^+ (\upsilon = 0) \leftarrow X^2\Pi (\upsilon = 0)$ around $3060\,\text{Å}$ [55].

In the first case, the LIF signal is recorded around $2970\,\text{Å}$ and, in the case of mixtures containing oxygen, the excitation spectra is strongly disturbed by either LIF signal from vibrational-excited O_2 $(X, \upsilon = 6)$ [43] or the O_3 strong absorption band at around $2480\,\text{Å}$ [44]. In the second case, the fluorescence signal is recorded from the $A^2\Sigma^+ (\upsilon = 1) \rightarrow X^2\Pi (\upsilon = 1)$ around $3150\,\text{Å}$ and from $A^2\Sigma^+ (\upsilon = 0) \rightarrow X^2\Pi (\upsilon = 0)$ centred in $3090\,\text{Å}$ thanks to vibrational energy transfer from $A^2\Sigma^+ (\upsilon = 1)$ to $A^2\Sigma^+ (\upsilon = 0)$.

In many applications involving NTP of noble gas (i.e. He and Ar) with the addition of OH precursors like H_2O, spontaneous emission from plasma-excited OH molecules is

emitted from the same bands involved in the LIF process [18], thus introducing a potential source of error in the measurement. In the last excitation scheme, the fluorescence signal is observed from the transitions $A^2\Sigma^+\,(\upsilon = 0) \rightarrow X^2\Pi\,(\upsilon = 0)$ that is centred at $3090\,\text{Å}$, very close to the excitation wavelength ($3060\,\text{Å}$), that in turn can cause scattered light to be recorded by the LIF signal detection system [53]. Laser-beam stray light collection causes a decrease in the signal-to-noise ratio of the LIF readout apparatus.

3.2 Spectroscopic scheme

In general the choice of N must be guided by the criteria of maximum population and smooth dependence on the rotational temperature, so that small local changes of temperature do not influence appreciably the outcome. Low rotational levels generally satisfy these requirements. For example, when using the $Q_1(1)$ line of $A^2\Sigma^+\,(\upsilon = 1) \leftarrow X^2\Pi\,(\upsilon = 0)$, the relevant sublevel of the ground state is $F_1(N = 1)$. Its relative population is 0.196 at $300\,\text{K}$, 0.167 at $350\,\text{K}$ and 0.145 at $400\,\text{K}$. In cold pulsed discharges, where the gas temperature remains below $350\,\text{K}$, neglecting temperature variations produces an error within 15%. The situation is even better for the sublevel $F_1(N = 2)$ that goes from 0.196 at $300\,\text{K}$ to 0.161 at $400\,\text{K}$, and for $F_1(N = 3)$ that ranges from 0.149 to 0.140 in the $300 - 400\,\text{K}$ interval, and drops only to 0.127 at $500\,\text{K}$. The choice, for example, of the $P_1(3)$ line for excitation makes the rotational population of the initial state almost constant in a wide temperature range.

In the present work we adopted the classical excitation-detection scheme that involves transitions of the $3064\,\text{Å}$ system [34]:

$$OH(X^2\Pi, v, N) + h\nu_L \rightarrow OH(A^2\Sigma^+, v', N') \rightarrow OH(X^2\Pi, v'') + h\nu_F \qquad (3.1)$$

with $v = 0$, $v'' = v' = 1$. We used several rotational transitions (see Appendix B for the nomenclature of transitions and rotational levels) :

- the $Q_1(1)$ at $2819.13\,\text{Å}$ and the $Q_2(3)$ at $2829.37\,\text{Å}$ for measurements of OH density;
- the $P_1(3)$ at $2830.09\,\text{Å}$ for the recovery of the saturation characteristic;

- the group of lines $Q_{12}(1)$ at 2829.21 Å, $Q_2(1)$ at 2829.23 Å, $Q_1(6)$ at 2829.27 Å, $Q_{12}(3)$ at 2829.31 Å and $Q_2(3)$ at 2829.37 Å for temperature measurements.

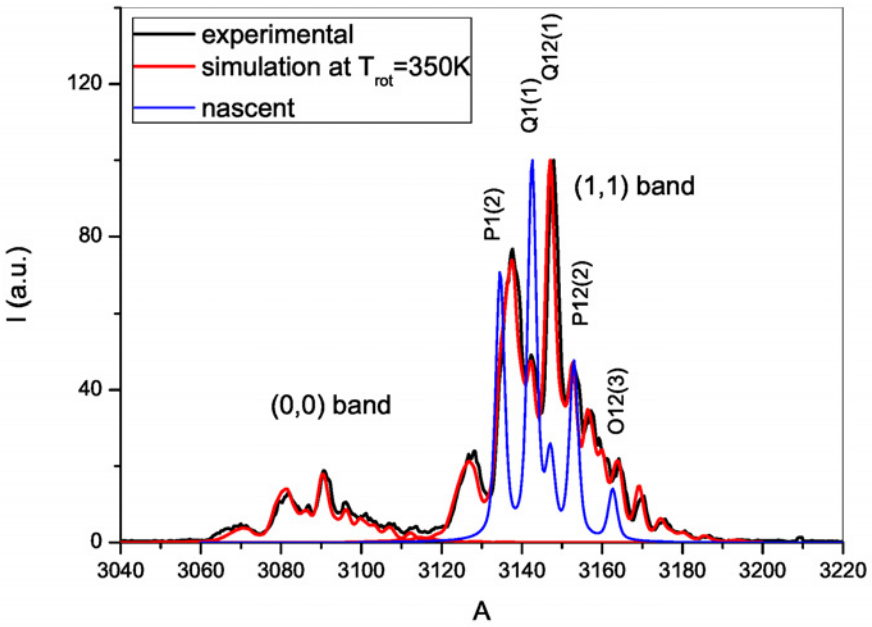

Figure 3.1: Laser Induced Fluorescence spectrum in a He−H_2O dielectric barrier discharge, after excitation of $OH(A^2\Sigma^+, v' = 1, N' = 1)$ by scheme 1. The rotational transitions labels refer to the nascent spectrum, which is the expected one in the absence of RET collisions.

The fluorescence is captured by a broadband detection. Due to fast RET collisions, the initial population of the rotational level N' excited by the laser is quickly redistributed in the whole rotational manifold towards a Boltzmann distribution at equilibrium with the gas temperature. This can be seen in Figure 3.1, in which the observed fluorescence spectrum shows a thermalised rotational distribution, in contrast with the nascent spectrum (i.e. in the absence of RET collisions) that contains only transitions coming from the N'=1 pumped level.

Another clear feature of the spectrum shown in Figure 3.1 is the presence of the (0,0) vibro-electronic band, in spite of the fact that only the (1,1) band has been pumped by the laser. This is due to VET processes induced by collision with water molecules. Figure 3.2

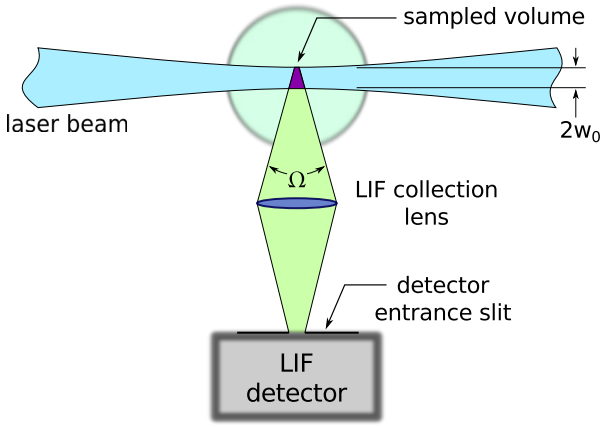

Figure 3.2: Schematic representation of a LIF experiment; the sampled volume is defined by interception between the laser beam (that excite the OH molecules) and the collection lens cone of acceptance.

presents the basic arrangement of our LIF experiment. The laser beam is injected into the target either directly or focalised (as in Figure 3.2). The fluorescence signal is observed in the scattering arrangement, in which the signal is collected from a different direction from the laser beam [42]. Collecting the LIF signal perpendicular to the laser beam is the arrangement of choice in order to prevent stray light caused from scattering at optical surfaces. Thanks to this configuration, the spatial resolution of the measurement is very high. The sampled volume is defined by the intersection of the laser beam (whose diameter is $2w_0$) and the collection lens acceptance cone (defined by the solid angle Ω and the distance between the sampled volume and the lens).

3.3 LIF Experimental Set-up

The LIF experimental set-up is composed of three main parts: the laser light generation and manipulation apparatus, the collection and detection of fluorescence signal system, and the PC-based control system.

3.3.1 Laser light generation and manipulation

The quality (in terms of beam profile) of the generated laser beam, energy and wavelength stability are crucial requirements in order to carry out precise and accurate measure-

ments. We modified the laser-light source to have a more stable source in terms of wavelength and more reliable wavelength scanning. In addition we spatially filtered the laser beam, so that hot spots and excessive long tails are removed from the laser beam spatial profile.

Laser source

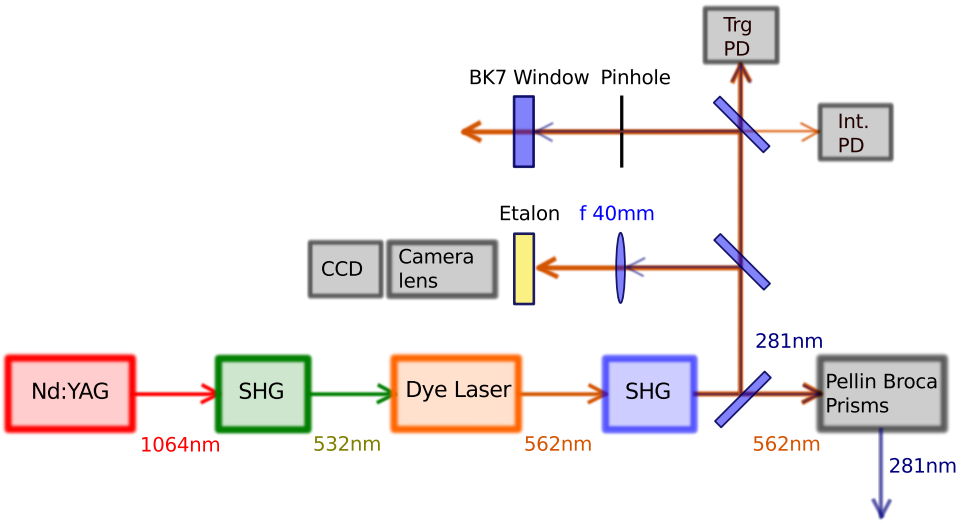

Figure 3.3: UV-laser source setup: Nd:YAG: Q-switched laser, SHG: frequency doubling crystals, Trg. PD: interferometer sample and hold circuit trigger source photodiode, Int PD: interferometer signal photodiode, CCD: camera to record the etalon fringe pattern

The laser source set-up is shown in Figure 3.3. It is composed of a dye laser (TDL50, Quantel) pumped by a Q-switched Nd:YAG laser (YG580, Quantel). The Nd:YAG laser works with a repetition rate of $10\,\mathrm{Hz}$, generating a $1064\,\mathrm{nm}$ pulse. Frequency doubling is achieved by passing the beam through a second harmonic generator (type II KDP crystal). The obtained $532\,\mathrm{nm}$ average power is $360\,\mathrm{mJ\,pulse^{-1}}$ and serves to pump the dye laser. A mixture of methanol and Rhodamine 590 chloride (Exciton, $89\,\mathrm{mg\,l^{-1}}$, tuning range $552-584\,\mathrm{nm}$) flows in the dye laser oscillator and pre-amplifier dye cells. Only methanol flows in the second capillary dye cell, because the energy of the beam generated by the pre-amplifier (around $11\,\mathrm{mJ\,pulse^{-1}}$) is enough for second harmonic generation. The dye output beam is then frequency doubled using a KDP crystal harmonic generator. The UV-beam energy at

2810 Å, after fundamental separation, is around 0.53 mJ pulse^{-1}. UV-beam separation from the fundamental is achieved using a wavelength filter composed of two CaF_2 Pellin-Broca prisms and a beam stopper in the middle.

In order to prevent dye laser wavelength fluctuations during fixed wavelength operations, and to perform more accurate scans (avoiding the use of the dye laser motors to move the tuning mirror), we modified the moving system of the tuning mirror of the laser cavity. A representation of the Quantel TDL50 sine drive mechanism is presented in Figure 3.4.

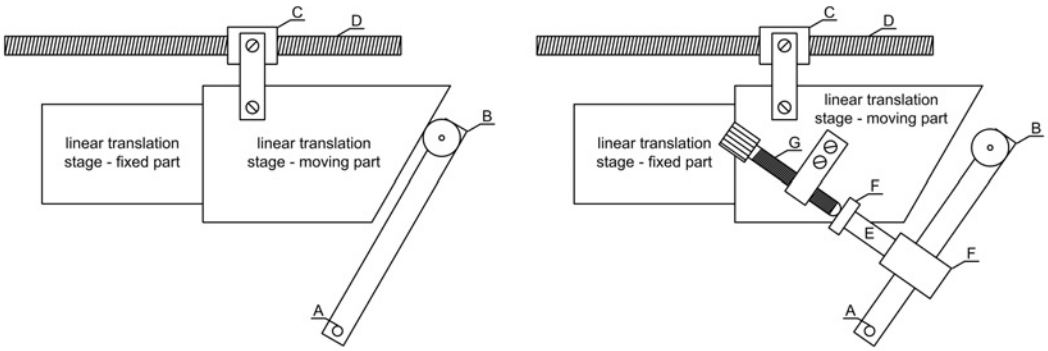

Figure 3.4: Comparison between the original sine drive mechanism of the dye laser tuning mirror (on the left), and the modified one (on the right)

On the left it is shown the original one, where the sine bar rotating arm (B), that is connected through the rotational axis (A) to the tuning mirror, is moved by a liner translation stage. The translation stage and the nut (C) are moved by the lead screw (D) rotation. On the right the modified mechanism is presented. An adjustment screw (G) and a piezoelectric actuator (E) (Thorlabs AE0505D16, housed in a holder (F) connected to the sine bar rotational arm) are placed between the sine bar rotating arm and the translation stage. The measured conversion factor between the linear translation stage displacement and the wavelength variation is $\xi = 5 \times 10^3$ pm mm^{-1} in the original mechanism. In this configuration the distance between the centre of the rotational axis (A) and the point of contact of the linear translation stage with the sine bar translation arm is $L = 85$ mm. In the new configuration the distance between the centre of the rotational axis (A) and the centre of the piezoelectric actuator holder (F) is $l = 35$ mm. In both cases the angle between the vertical and the sine bar translation arm, in the wavelength region around 562 nm, is $\alpha = 25\,^{\circ}$C.

The nominal piezoelectric actuator displacement at the maximum working voltage (100 V) is $\Delta l = 12(2)$ µm, so the maximum wavelength displacement is given by:

$$\Delta \upsilon = \xi \frac{L}{l} \frac{\Delta l}{cos\,(\alpha)} = 16(3) \times 10 \text{ pm}.$$

In this way, it is possible to perform wavelength scans by using only the piezoelectric actuator (for intervals smaller than $\Delta \upsilon$), or to use the original system based on DC motors controlled by the PC (see Chapter 3.3.4). Moving the tuning mirror with the piezoelectric actuator has the disadvantage that the dye laser control unit cannot read the actual wavelength. The laser control unit calculates the wavelength by using an optical encoder connected directly to the lead screw and moved by the DC motors.

During fixed wavelength laser operations, when the laser needs to be tuned to a molecular transition for a long time, it is crucial to avoid changes of the output wavelength of the dye laser. Temperature drifts and mechanical relaxations of the mechanism that controls the tuning mirror of laser cavity cause variations of the beam wavelength in the order of $10 - 20\,\text{pm}\,\text{h}^{-1}$. To fix this problem, we implemented a feedback mechanism for the dye laser based on a etalon and a CCD (Figure 3.3). A fraction of the laser beam is sampled before the Pellin-Broca prisms by using a wedge quartz window. The sampled beam is sent to a $f = 40$ mm BK7 lens. The etalon ($FSR = 10$ GHz, broadband) is placed behind the lens focal point, in order to have a divergent beam incident on it. A $50 - 200$ mm manual camera lens (Tamron) coupled with a grey-scale CCD (DMK 41AU02.AS, Imaging Source) are used to record the interference fringes. The exposure time of the CCD is set to 300 ms, shots are recorded and analysed with a program written in LabVIEW. The stabilisation program of the laser records the etalon picture, creates the image histogram, along a direction defined by the user, which intercepts the more intense interference fringes and performs the peak detection. Positions (in pixel) of two fringes are recorded to track the wavelength (absolute position) and to calculate the conversion factor between the etalon free spectral range (FSR) and the camera pixels (relative position). The change in the absolute position of one of the two fringes is used to generate a signal that is converted in the voltage of the piezoelectric actuator to correct the dye laser output wavelength. The laser beam is stabilised within $0.1\,\text{pm}\,\text{h}^{-1}$ around the desired wavelength.

In the case of wavelength scanning carried out by using the piezoelectric actuator, it is

necessary to measure the change in wavelength. For this purpose, a small fraction of the dye beam is sampled by a quartz wedge window and sent to a low-finesse Fabry–Pérot interferometer made by a $1/2''$ thick $2''$-diameter BK7 window. The interferometer FSR is given by:

$$FSR = \frac{\lambda^2}{2nlcos\vartheta} = 8.1\,\text{pm}$$

where $n = 1.51794$ is the BK7 refractive index at $\lambda = 562\,\text{nm}$, $\vartheta = 0°$ is the angle between the incident beam and the window, and $l = 12.84\,\text{mm}$ the window thickness. An iris is placed in between the two windows to align the etalon. Interference fringes reflected by the interferometer are detected for each laser shot, by using a photodiode placed behind the wedge window. The other part is sent to another photodiode that serves as trigger source for the sample-and-hold circuit that carries out the interferometer readout.

3.3.2 Beam Optics

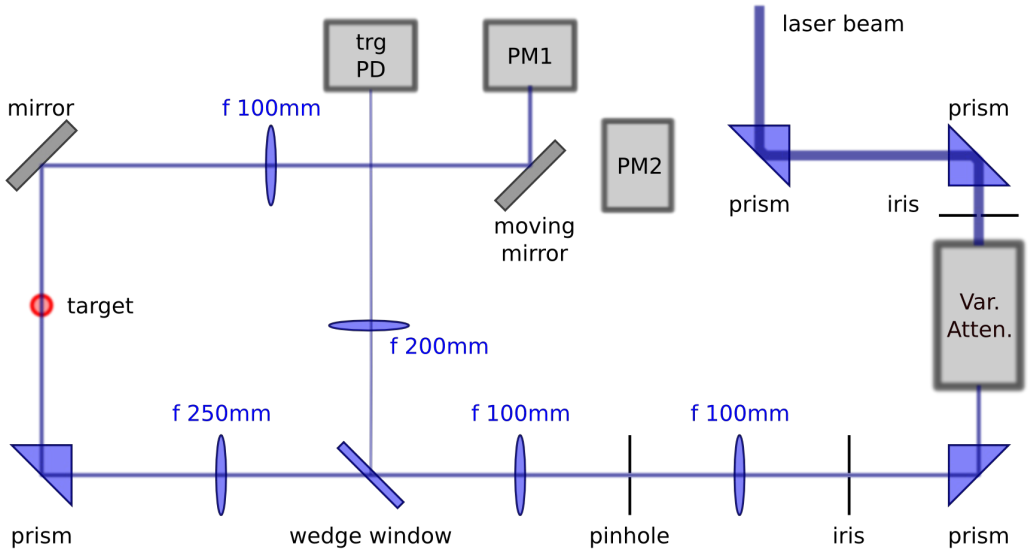

Figure 3.5: UV-beam optics set-up schematic representation. Var. Atten.: optical variable attenuator; trg PD: oscilloscope acquisition trigger source; PM1: low energy ($< 4\,\mu\text{J pulse}^{-1}$) power monitor; PM2: high energy ($> 4\,\mu\text{J pulse}^{-1}$) power monitor.

The UV laser beam is injected in a separate breadboard, where it is manipulated to hit the target with a known shape and power (Figure 3.5). The UV-beam is collected by two

right angle prisms that correct propagation, height, and direction of the beam. To change the power injected into the target, we developed a variable optical attenuator based on Fresnel reflection, suitable for applications where a high-peak power is involved [61]. A further requirement is that the optical variable attenuator does not significantly alter the beam profile, position and direction. A detailed description of the device design and performances is reported in Appendix A.1.

The attenuated beam passes through a spatial filter composed of two $f = 100\,\text{mm}$ biconvex UVFS lenses, and a pinhole to filter the beam noise. The pinhole cuts the wings of the spatial Fourier-mode spectrum of the incoming beam. Beam imperfections, due to laser generation, frequency doubling and optics quality, cause structures in the beam with higher spatial modes that are cut off by the pin-hole [62]. The estimated beam waist is $23(3)\,\mu\text{m}$ in the focal plane of the spatial filter. We chose a $\varnothing 50\,\mu\text{m}$ high-power precision pinhole (P50C, Thorlabs) coupled with a precision positioning system (M-461-XYZ-M, Newport). A wedge UVFS window is placed after the spatial filter to sample a fraction of the incident beam, which is then used to generate the acquisition trigger signal. A $12\,\text{V}$ reverse biased broad-band UV SiC photodiode (SG01M, Sglux), coupled with a diffuser, collects the trigger beam and records the time profile of the laser. The filtered laser beam is then injected in the target area, either directly (with a $2\,\text{mm}$ beam diameter) or focalised by a $f = 250\,\text{mm}$ UVFS plano-convex lens (expected beam diameter is $0.2\,\text{mm}$).

In order to avoid back reflection of the UV-beam into the target area, an aluminium mirror (working at 45°) directs the beam towards the detection system. For low energies ($E < 4\,\mu\text{J pulse}^{-1}$), a single-channel silicon-based thermopile (DX-0576, Dexter research center) is used. The thermopile output voltage is amplified by a non-inverting amplifier with gain $G = 500$, and the peak voltage of the signal is acquired by using a digital multimeter (34410A, Agilent). The pulse energy is inferred from the peak voltage, which in turn is proportional to the energy deposited on the detector (see Appendix A.2.1 for a detailed description). In the case of higher energies ($E > 4\,\mu\text{J pulse}^{-1}$), the moving mirror is removed and the UV-beam energy is measured by using a pyroelectric detector (P1-13, Molectron), amplified by a high speed non-inverting amplifier, and then digitising by using an oscilloscope (Infiniium 54831B, Agilent). In this case, the detector has a fast time response, which

allows us to record the amplifier output simultaneously to the signal of the photomultiplier tube. I describe two devices in Appendix A.2.

3.3.3 Fluorescence detectors

The laser induced fluorescence is emitted isotropically from the target [63]. The collection of the fluorescence emitted perpendicular with respect to the laser beam is the arrangement of choice in order to minimise the possibility of collecting scattered laser light. A schematic representation of the fluorescence detection optics is shown in Figure 3.6. The

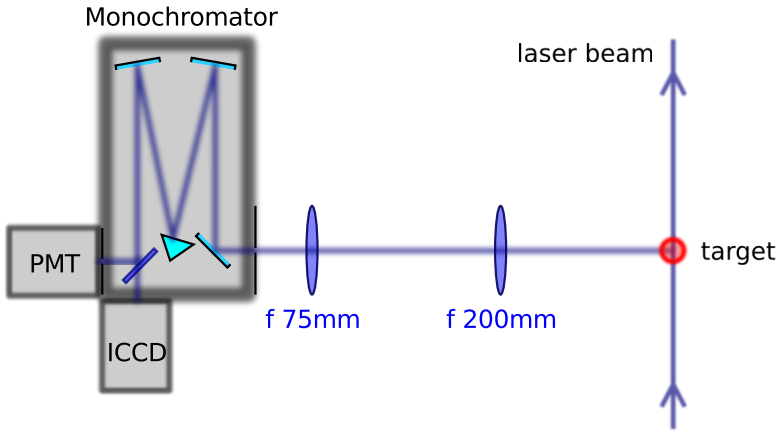

Figure 3.6: Schematic representation of the laser induced fluorescence detector arrangement. PMT: gated photomultiplier tube for time-resolved measurement; ICCD: multi-channel plate plus charge coupled device.

fluorescence signal emitted is collected by a $f = 200\,\text{mm}$ $\varnothing = 1''$ UVFS plano-convex lens. Two $\varnothing = 2''$ enhanced aluminium mirrors (omitted in figure) are used to direct the light to the monochromator entrance slit. A $f = 75\,\text{mm}$ UVFS plano-convex matches the incoming beam to the f-number of the monochromator. A set of four neutral density filters (NDUV01B,NDUV03B,NDUV06B and NDUV510B, Thorlabs) is placed in front of the input slit to change the incoming light intensity. A Shamrock 303i 300 mm focal length monochromator, equipped with two gratings ($1200\,\text{gr}\,\text{mm}^{-1}$ blaze 300 nm and $600\,\text{gr}\,\text{mm}^{-1}$ blaze 300 nm) is used to separate the spectral components of the fluorescence signal. The monochromator is coupled with two different detectors: a 1024×1024 px intensified CCD (ICCD) (DH334T-18U-03, Andor) and a gateable photomultiplier tube (PMT) (8575, Burle

Electron Tubes). The ICCD is used to record the spectrum of fluorescence signal, while the PMT serves to record the temporal evolution of the LIF signal.

When LIF is applied to targets with a strong spontaneous emission at the same wavelengths involved in the fluorescence, it is crucial to use gated detectors. ICCDs gating can be simple, since the multi-channel plate (MCP) can be used as an electrical shutter. PMTs can be gated by using a proper bias circuit, the latter been described in Appendix A.3.

3.3.4 Control System

To control the laser source, to record the LIF signal, and to synchronise the measurement with the discharge, we developed a PC-based control system, represented schematically in Figure 3.7. The two main building blocks of the apparatus are the digital delay generator (DDG), and the control program (CP) that is written by using LabWindows/CVI (National Instruments).

Digital Delay Generator

The five-channel DDG was developed using the evaluation board ZedBoard based on the Zynq-7000 All Programmable SoC (Z-7020, Xilinx). The presence in a single device of a ARM Cortex A9 dual core processor and a field programmable gate array (FPGA) permits to develop stand-alone devices where real-time operations are carried out by the FPGA, with the possibility to communicate with the latter using user space programs running on a linux operating system. A FPGA-design was developed in order to create five independent delayed channels starting from an either external or internal clock reference. The minimum time step is $2.5\,\text{ns}$. The maximum settable delay is $21.4\,\text{s}$, the external source to channel jitter, expressed in terms of 3σ is $j_{ext-ch} = 2.2\,\text{ns}$, the internal source to channel jitter is $j_{int-ch} = 74.3\,\text{ps}$, and the channel to channel jitter is $j_{ch-ch} = 35.1\,\text{ps}$. An AXI-Lite core ($32\ bit$ for $32\ bit$ address) is used to ensure the communication between ARM (master) and FPGA (slave). The developed custom device (delay generator plus the AXI-lite interface) is integrated in a linux-based system running on the ZedBoard. Programs in C language were written in order to set channel states, delays and on-times.

Two channels of the DDG (D and E) are used to trigger the Nd:YAG control unit to start

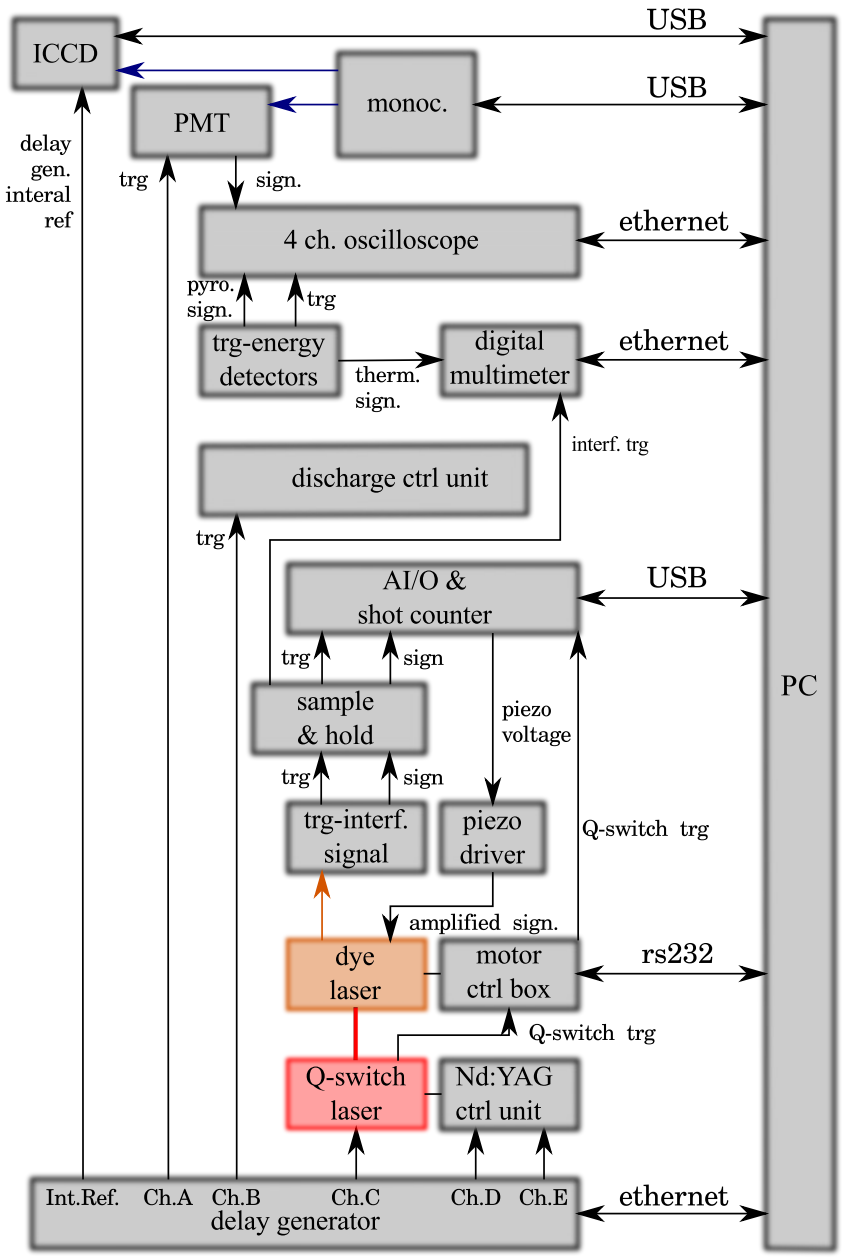

Figure 3.7: Schematic representation of the control system of the apparatus. monoc: monocromator; trg-energy detectors: acquisition photodiode, thermopile and pyroelectric energy monitors;

the capacitors charge (charge-order) and the flash of the laser lamps (fire-order). Another delayed channel is used to control the Q-switch unit of the laser. The same trigger signal is sent to the laser-motor control unit that records the dye laser wavelength and controls the DC-motor that moves the tuning mirror of the laser. The laser-motor control unit is composed of two elements: a digital control unit based on a FPGA evaluation board (Spartan 3 starter kit, Digilent-Xilinx), and an analog multiplexing unit. The digital control unit reads the wavelength of the laser, communicates the wavelength via rs232 to the PC (either on software trigger or on laser shot) and it can receive a set of commands used to control the dye laser tuning mirror. The analog multiplexing unit is composed of two high-voltage 4-channel multiplexer (ADG5404, Analog Devices). In our configuration the operator can chose two voltage levels (slow and fast scanning) by setting the output of a two channel power supply (E3631A, Agilent).

The dye laser control box, after every laser shot, repeats a delayed (100 µs) trigger signal that is recorded by a counter implemented in a USB DAQ card (NI-USB 6009, National Instruments). During LIF measurements, the counter state is continuously checked, and when there is a new count the program starts the acquisition from the oscilloscope (PMT-LIF signal and pyroelectric detector signal), from the DAQ analog channels (interferometer signal and reference), from the multimeter (thermopile detector signal) and reads the rs232 buffer in order to get the laser wavelength. The signals generated by the interferometer photodiode and its reference are stored in a sample and hold circuit (SHC) prior to acquisition. The SHC acquisition is triggered by the interferometer reference signal, and the sampling time is chosen to get the maximum signal from the photodiodes. An analog output of the DAQ card is used to control the high-voltage output of the piezoelectric driver (MDT694A, Thorlabs).

The remaining two channels of the DDG (A and B) are used to trigger the on-state of the PMT, and to trigger the discharge. The DDG internal reference is used to trigger the ICCD's DDG that sets the on-state of the CCD and MCP.

PC based control program

The program for the control of the apparatus (CP) can acquire LIF excitation spectra while laser is scanning using the DC motor (usually long scan) or using the piezoelectric actuator (short scan). The operator can choose the type of detection, start and stop wavelength scan, the total number of points for the scan and the number of averages to be computed. The CP records shot by shot the fluorescence signal recorded by the PMT, computes the integral of the signal corrected by the baseline (the user can choose the integration interval and set the baseline). The CP controls also all the ICCD features (exposure, temperature, binning etc.) and the spectrometer. It is also possible to change the fluorescence detector by moving via software the flipping mirror inside the monochromator and consequently setting the appropriate grating (PMT is used with the $600\,\mathrm{gr\,mm^{-1}}$, blaze $300\,\mathrm{nm}$ grating; the ICCD with the $1200\,\mathrm{gr\,mm^{-1}}$, blaze $300\,\mathrm{nm}$ grating).

3.3.5 Discharges Design

LIF measurements were performed on two different types of discharges. The first one is a He$-$$H_2O$ DBD discharge with small amount of O_2, already described in Chapter 2.2.3. The second one is a RF plasma jet. The capability of non-thermal plasma to generate reactive oxygen species (ROS) is well known [23, 58]. When dealing with biological or medical applications, plasmas are required to operate at atmospheric pressure and the plasma effluent has to remain at low-temperature to avoid thermal damages of the biological targets. He, due to its excellent thermal conductivity, is considered the carrier of choice for these non-thermal plasmas. In order to produce ROS, precursors like O_2 or H_2O, can be added to the gas carrier [15, 64].

Figure 3.8 shows a schematic representation of the RF plasma jet. The plasma source consists of a tungsten needle of $2\,\mathrm{mm}$ diameter that acts as high voltage electrode, surrounded by a quartz tube ($3\,\mathrm{mm}$ inner diameter, $5\,\mathrm{mm}$ outer diameter) where a mixture of He and H_2O flows. In order to prevent contamination of the plasma plume by the outside atmosphere a PTFE tube ($6\,\mathrm{mm}$ inner diameter, $7\,\mathrm{mm}$ outer diameter) concentric to the needle is used to inject a co-flow of pure He. The He$-$$H_2O$ mixture is obtained by injecting a fraction of the gas carrier inside a bubbler filled with distilled water at room temperature. Gas

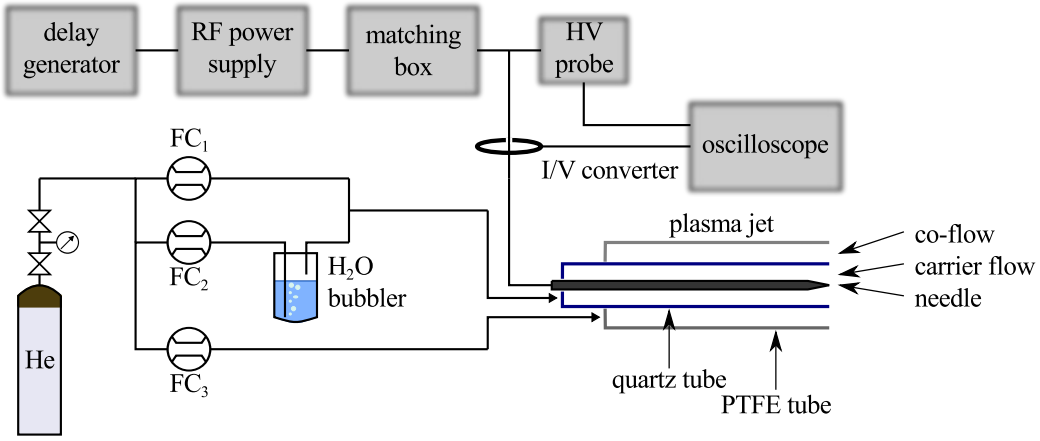

Figure 3.8: Schematic representation of the RF-driven plasma jet, the gas feed and electrical set-up. He: He cylinder 99.995% purity; FMC_1, FMC_2 and FMC_3: mass flow controllers for He carrier, He carrier injected in the water-bubbler and co-flow He respectively.

flows are controlled by using three mass flow controller (1179A, MKS) with 5000 sccm, 500 sccm and 20 000 sccm full scale for the carrier, carrier injected in the bubbler and co-flow, respectively. The grounded electrode (an aluminium cylinder of 20 mm diameter) is placed 11(1) mm below the tungsten needle tip and a temperature sensor (LM35, Texas Instruments) is placed inside it to monitor the target temperature. The used targets are liquid, placed inside a small PTFE cylindrical vessel on the grounded electrode. In this configuration, the plasma jet is a so-called *linear field plasma jet*, because the electric field and the gas flow have the same direction [65]. A 500 W RF power supply (RF5S, RFPP) working at 13.56 MHz generates the discharge. Impedance matching between the power supply and the plasma jet is achieved by using an automatic matching network (AM5, RFPP). In order to measure the power dissipated in the plasma, we used a voltage probe (P6015A, Tektronix) and a high bandwidth (200 Hz to 500 MHz) I/V converter (CT-01-b, Magnelab). Their signals are recorded and digitising with a DSO (Wavesurfer 104MXs-A 1 GHz 5 GSps, LeCroy).

As described previously in Chapter 2, spontaneous emission arising from the plasma plume generate a strong signal in the same bands interested by the fluorescence. Thanks to the possibility to gate the RF power supply, the plasma jet can be switched on and off. After the plasma is switched off, excited OH vanishes faster than ground state OH. Thus an

appropriate gate strategy is the best solution for decreasing or even eliminating the interference spontaneous emission on LIF signal. The LIF measurement is carried out $14.6\,\mu s$ after switching off the plasma.

3.4 Model description

The model of the LIF process is based on a set of rate equations that describe the time evolution of the population of the involved states.

The simplest treatment [52], assumes that the population of the ground state is constant. This approach is valid only in a strictly linear regime. In addition, the laser pulse is approximated by a rectangular function. With these approximations, an analytical solution can be found for the LIF outcome. Similar choices were made in [51]. A three level model was implemented in [34], assuming a rate equation for the ground state and an arbitrary laser pulse. Although in principle the three level model includes the possibility to handle saturation effects, it does not account for rotational energy transfer (RET) processes, which play an important role in the saturation regime. In [66], a fourth level equation for the state $(X, \upsilon = 1)$ was added. The idea is that electronic quenching of $(A, \upsilon = 1)$ terminates into $(X, \upsilon = 1)$, that is then coupled to the initial $(X, \upsilon = 0)$ state by vibrational relaxation. As a matter of fact, vibrational relaxation in the ground state is slow, and this path is negligible for $(X, \upsilon = 0)$ re-population within the laser duration time. In the same model, electronic quenching of $(A, \upsilon = 0)$ was assumed to terminate the molecule into $(X, \upsilon = 0)$. Although not explicitly stated in that paper, we believe that such an assumption is based on the Franck-Condon factors of the $A - X$ transition, that feature a large prevalence of the (0,0) transition. In [67] a long discussion on this issue is given, without a clear conclusion. Since modelling which fraction of the A state terminates into X state after electronic quenching is quite arbitrary, the authors of [67] calculated the effect of variations of such a fraction on the LIF model outcome. In order to contribute to the process, refilling of the X state by electronic quenching should be competitive with RET refilling. Its influence to the populations cycle can be important only at very high laser irradiance, when the population of the whole $(X, \upsilon = 0)$ rotational manifold starts to be significantly decreased within the laser pulse duration. For this reason we decided to neglect this process in our model.

RET collisions were considered also in [68] and [67]. The six-level model of [67] was also used in [69]. In this model the two ro-vibronic N and N' states involved in the absorption process are connected by total RET collision rates to two additional "lumped" states that include the whole remaining rotational manifold of the $(X, \upsilon = 0)$ and $(A, \upsilon = 1)$ vibro-electronic states. Given that RET rates, although somewhat uncertain, are very high, it was shown in [66] that the model outcomes are substantially independent of the exact values of RET rates, provided these are sufficiently larger than the absorption rate. Then the model can be simplified by dropping the two equations for the lumped states and setting the N and N' states always at Boltzmann equilibrium with the gas temperature. This is equivalent to saying that RET are so fast that both X and A rotational manifolds achieve equilibrium with the gas temperature at any time during the laser pulse. The validity of this four-level model was empirically tested with a $250\,\mu$m diameter laser beam with energy up to $9\,\mu$J. In the previous models the spatial distribution of the laser beam is assumed to be uniform. Only in [67] it was taken into account, with a test of different functional forms of the spatial dependence of the laser fluence.

RET collisions in both X and A states can be neglected in the linear regime, since the depletion of the initial state and its refilling by stimulated emission is negligible. In addition, to assume a spatially uniform laser beam is a good approximation. Thus in the linear regime the rationalisation of the LIF process is greatly simplified, since phenomena that are difficult to model can be neglected. It is then critical to establish the laser energy range in which linearity is achieved. As a rule of thumb, with current spectral bandwidths of dye lasers, and with beam section of the order of 1 mm diameter, linearity is found up to few μJ of laser pulse energy, for the transitions of scheme 3.1. On the other hand in an ATP plasma jet a sub-mm space resolution is required. The laser beam section can be reduced by a focusing lens to the order of a $100\,\mu$m diameter, that is suitable for jet space scales. As a consequence, linearity is found at energies below $0.1\,\mu$J, while the sampled volume, i.e. the LIF signal, is also reduced by about two orders of magnitude. To ensure space resolution and sensitivity it is then necessary to operate LIF in a partially saturated regime. We present in the following a detailed model that takes into account RET processes in both X and A states and a non-uniform (gaussian) space distribution of the laser fluence. The aim is to

understand better the whole process and to provide a realistic description that allows us to operate LIF in a partially saturated regime with a focused beam.

3.4.1 Validity of the rate equations model

The exact description of the interaction of matter with intense, coherent light is given by a density matrix formulation, the so-called optical Bloch equations [70]. In a two-level interaction with a classical electromagnetic field, the off-diagonal matrix elements contain the dipole interaction term and account for coherent effects. In the absence of any damping term, the equations have an oscillating solution at the Rabi frequency. Damping terms in the equations of the off diagonal equations are added empirically and account for processes that destroy the coherence of the interaction. Radiative decay and collision processes then have the effect of damping the Rabi oscillations up to reaching a steady-state in a time that depends on the damping rate. The validity of rate equations (RE) in place of density matrix equations (DME) in the case of a pulsed laser field was examined in [71], where it was shown that DME formalism is equivalent to RE in the steady-state approximation, i.e. when coherence damping suppresses Rabi oscillations. In the pulsed case this condition is obtained when the damping rate is much larger than the rate of change of the electric field, or, in other words, the damping characteristic time is much less than the laser pulse rise time, so that steady state is achieved with good approximation at any time during the laser pulse. In our case, as in ordinary pulsed dye lasers, the pulse duration is about 10 ns FWHM, and the rise time is of the order of some ns. All kinds of collisions in addition to pressure broadening ones, are de-phasing events, i.e. also velocity changing collisions and quenching collisions. A pressure broadening of the order of 2 GHz in He [37] gives a de-phasing time of the order of 5×10^{-10} s. Velocity changing collisions have times of the same order of magnitude. RET rates, that also at equilibrium provide a continuous exchange of population, in both states, have a time of the order of 3×10^{-10} s . As a whole, then, and even in pure He, a de-phasing characteristic time of the order of 1×10^{-10} s can be estimated, that is much less than the pulse rise time. The addition of molecular gases has the effect of reducing the de-phasing time, since it generally increases both the pressure broadening and the quenching rate. A quantitative analysis of the difference between DME and RE model

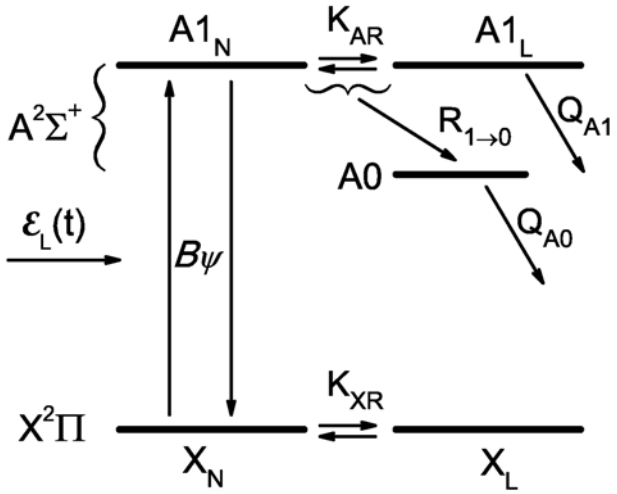

Figure 3.9: Scheme of the five levels of the model and of their mutual interactions. See text for symbols explanation.

outcomes, reported in [72], confirmed these results. In addition, the RE formulation, in conditions of sufficiently fast de-phasing as in our case, and in the presence of quenching, was seen to decrease its accuracy on increasing electric field strength and on increasing the electronic quenching up to values comparable to the pulse duration, but always with a reasonable error never larger than about 15% [72]. For this reason, anyway, the choice of working at moderate saturation conditions is a conservative one.

All the previous discussion refers to a single-mode laser. Our laser is, instead, a multi-mode one, with a variable composition of 3-5 modes per pulse, and rare pulses with 2 modes only. Modes are totally uncorrelated between each other, so that the interaction of a molecule with such a multi-mode field implies a series of photon exchanges that may not be in phase. This subject is quite difficult to treat, but certainly we can state qualitatively that it is a further source of de-phasing, at the limit of thermal light interaction when the number of modes is large, giving further validity to the RE approach. In [73], it was stated that the RE approach is valid if the coherence time of the laser is short compared to the pumping time (reciprocal of absorption probability).

3.4.2 Five-level model

We describe the LIF process by a 5-level system, schematically represented in Figure 3.9, in which the time evolution of the population of five states is calculated. We choose to label as population the density, and not the number of molecules, since we want to write the sampled volume explicitly in the formulas. As in [68, 67] RET collisions are taken into account by two rate equations for "lumped" states:

$$
\begin{aligned}
&\frac{dP_{X_N}}{dt} = -B\mathcal{E}_L(t)\psi(P_{X_N} - P_{A1_N}) + (\mathcal{F}_{X_N}P_X - P_{X_N})K_{X_R} \\
&\frac{dP_{X_L}}{dt} = -(\mathcal{F}_{X_N}P_X - P_{X_N})K_{X_R} \\
&\frac{dP_{A1_N}}{dt} = B\mathcal{E}_L(t)\psi(P_{X_N} - P_{A1_N}) - Q_{A1}P_{A1_N} - K_{A_R}(P_{A1_N} - \mathcal{F}_{\mathcal{A}}P_{A1}) \\
&\frac{dP_{A1_L}}{dt} = K_{A_R}(P_{A1_N} - \mathcal{F}_{\mathcal{A}}P_{A1}) - Q_{A1}P_{A1_L} \\
&\frac{dP_{A0}}{dt} = R_{(1\to 0)}P_{A1} - Q_{A0}P_{A0} \\
&with: \\
&P_X = P_{X_N} + P_{X_L} \\
&P_{A1} = P_{A1_N} + P_{A1_L}
\end{aligned}
\tag{3.2}
$$

- X_N is the $(X, \upsilon = 0, N)$ state that absorbs the laser photons;
- $A1_N$ is the $(A, \upsilon' = 1, N')$ state that is populated by optical absorption;
- X_L is the sum of all the rotational levels of $(X, \upsilon = 0)$ except N. In the equation X_N is depleted by absorption of the laser light, re-populated by stimulated emission from $(A, \upsilon' = 1, N')$ and by RET collisions from X_L. The refilling of X_N by RET from X_L is described by a term proportional to the difference between the actual X_N population and its equilibrium population, given by $\mathcal{F}_{X_N}P_X$, where $\mathcal{F}_{X_N}$ is the rotational population factor (fraction) at a given temperature. This is an approximation. The correct calculation should treat individual rotational levels with state-to-state rotational energy transfer rates. Both the poor knowledge of state-to-state rate coefficients and the difficulty of such a task recommend the approximation with a single equation for a "lumped" X_L state.

- $A1_L$, analogously is the sum of all the rotational levels of $(A, \upsilon' = 1)$ except N'. $A1_N$ is populated by optical absorption and depopulated by stimulated emission, spontaneous emission and by collisions with neutrals (Q_{A1} is the radiative plus electronic quenching plus vibrational relaxation rate). The rotational coupling between $A1_N$ and $A1_L$ is described in the same way as for the ground state case;

- $A0$ is the $(A, \upsilon = 0)$ total rotational manifold, that is populated by vibrational relaxation from $(A, \upsilon = 1)$ with rate $R_{(1\rightarrow 0)}$ and depopulated by radiative plus electronic quenching with rate Q_{A0};

The initial conditions for the populations are: $P_{A0}(t = 0) = P_{A1}(t = 0) = 0$, $P_{X_N}(t = 0) = \mathcal{F}_{X_N}[\mathrm{OH}]$, $P_{X_L}(t = 0) = [\mathrm{OH}] - P_{X_N}$. $P_{X_N}(t = 0)$ is the initial population of $\mathrm{OH}(X, \upsilon = 0, N)$, given by the product of the rotational population factor $\mathcal{F}_{X_N}$ and the OH density. The optical processes are calculated as follows.

- B is the Einstein coefficient for absorption. When the statistical weights are equal for both initial and final state, as it is for Q branch transitions, $B_{XA} = B_{AX} = B$.

- $\mathcal{E}_L(t)$ is the radiant energy density of the laser, that is a function of time, given by $W(t)/cS$ with c the velocity of light, S the laser beam section and $W(t)$ the laser power. We have calculated $W(t)$ using a measured laser time profile normalised such that the time integrated $W(t)$ is equal to the measured laser pulse energy E_L.

- ψ is the spectral overlap integral of the laser line and the absorption line:

$$\psi = \int_{-\infty}^{\infty} \varepsilon(\nu - \nu_L) b(\nu - \nu_x) \mathrm{d}\nu,$$

where $\varepsilon(\nu)$ and $b(\nu)$ are the spectral profile of the laser and the absorption line, respectively:

$$\mathcal{E}_\nu(t, \nu) = \mathcal{E}_L(t)\varepsilon(\nu - \nu_L) \qquad with \qquad \int_{-\infty}^{\infty} \varepsilon(\nu - \nu_L)\mathrm{d}\nu = 1,$$

$$B_{\nu,x}(\nu) = B_x b(\nu - \nu_x) \qquad with \qquad \int_{-\infty}^{\infty} b(\nu - \nu_x)\mathrm{d}\nu = 1.$$

The subscript x indicates the absorption line. The spectral profile of the laser line, $\varepsilon(\nu)$, has been deduced from the fit of laser excitation spectra (see fig. 3.10). $b(\nu)$ is

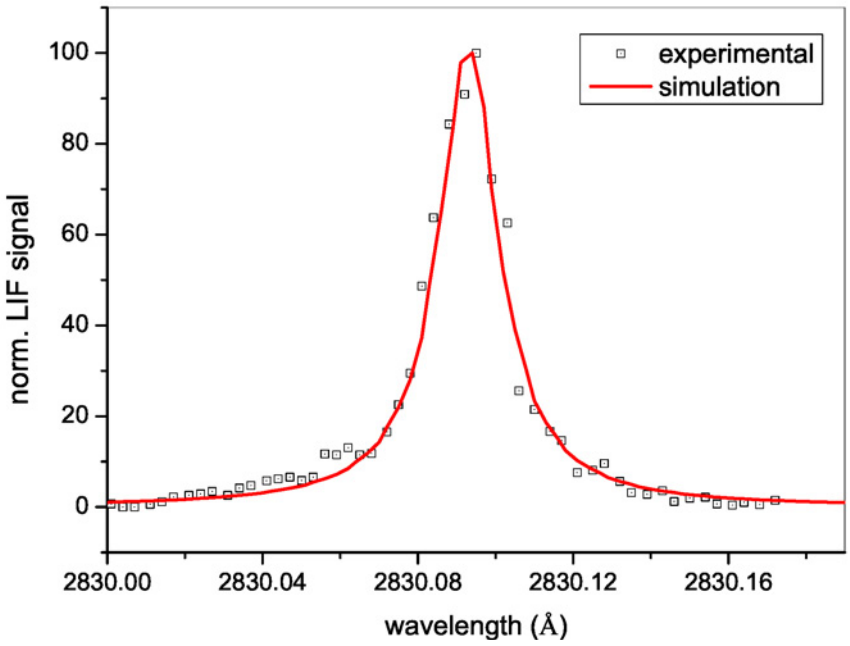

Figure 3.10: Laser excitation spectrum (laser wavelength scan) of an isolated ro-vibrational line ($P_1(3)$), with pressure (0.00535 Å) + Doppler (0.00916 Å) broadening = 0.0122 Å . The model simulation is obtained by a Lorentzian laser profile with 9×10^{-3} Å width.

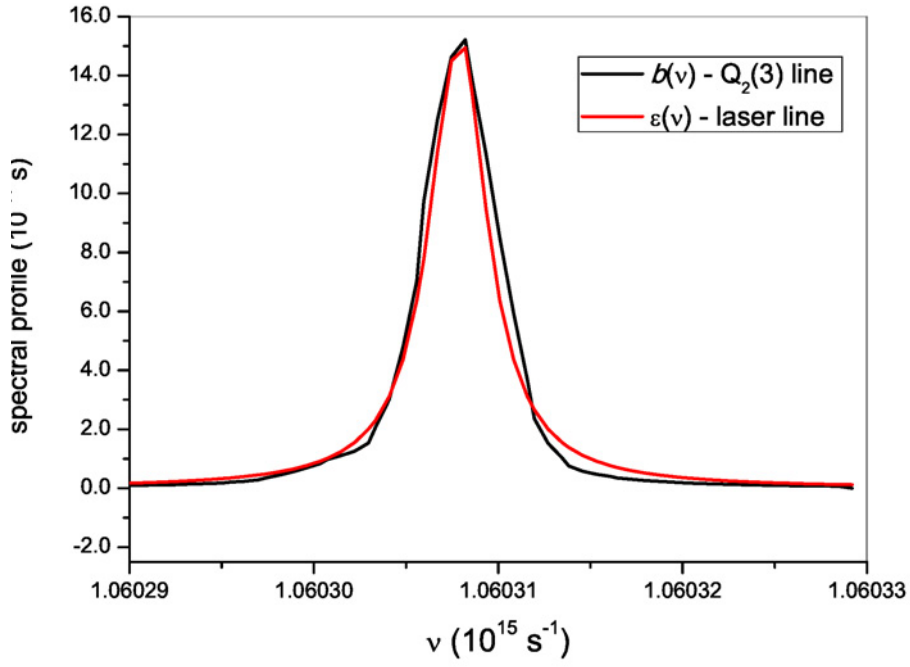

Figure 3.11: Spectral absorption and laser line profiles with the laser tuned on the $P_1(3)$ line. In this case $\psi = 8.65 \times 10^{-11}$ s

given by the Doppler plus pressure broadening. The superposition of $\varepsilon(\nu - \nu_L)$ and $b(\nu - \nu_x)$ is shown in Figure 3.11, where the laser is tuned on the $P_1(3)$ line. Note finally that the product $\mathcal{E}_L(t)\psi$ has the correct dimensions of a spectral radiant energy density required for multiplication with the Einstein coefficient B.

Model results are related to measured quantities as follows. The fluorescence pulse $S(t)$ is measured by the PMT. It is the sum of the contribution of the two bands:

$$S(t) = S_1(t) + S_0(t) = \mathcal{C}V_s(A_{(1,1)}P_{A1} + A_{(0,0)}P_{A0}).$$

$A_{(1,1)}$ and $A_{(0,0)}$ are the radiative rates of (1,1) and (0,0) bands and V_s is the sampled volume. The time integrated spectrally dispersed fluorescence $\mathcal{I}_{LIF}(\lambda)$ is measured by the ICCD:

$$\mathcal{I}_{LIF}(\lambda) = \Psi_{(1,1)}(\lambda)\int_0^{T_G} S_1(t)\mathrm{d}t + \Psi_{(0,0)}(\lambda)\int_0^{T_G} S_0(t)\mathrm{d}t.$$

The two $\Psi(\lambda)$ are the normalised emission spectra of (1,1) and (0,0) bands. T_G, the ICCD time gate, is larger than the fluorescence lifetime. $\mathcal{C}$ is a constant accounting for the transfer function of the optical collection plus measuring apparatus:

$$\mathcal{C} = \frac{\Omega}{4\pi}T\eta eGR.$$

Ω is the solid angle subtended by the collection optics, i.e. by a 1 inch lens at a 200 mm focal length distance from the sample. T is the transmission factor of the fluorescence collection optical path, given by the grating efficiency at 3100 Å and by the loss of the transmitting/reflective surfaces of the path. η is the quantum efficiency of the photo-cathode, G the gain of the photomultiplier and e, the electron charge, converts the number of photoelectrons per second into a current. $R = 50\ \Omega$ is the input resistance of the digitising oscilloscope. The quantitative analysis of LIF outcomes then requires the knowledge of $\mathcal{C}$, of the sampled volume V_s, of the collision rates, and, finally, the correct absorption rate that depends also on the laser beam section. Although $\mathcal{C}$ can be determined by a calibration of the optical arrangement, V_s is a critical parameter especially with a focused laser beam, due to the fact that the laser energy is not distributed uniformly in the beam section. Such a parameter requires a specific treatment and must be determined by investigation of the laser energy dependence in a calibration cell.

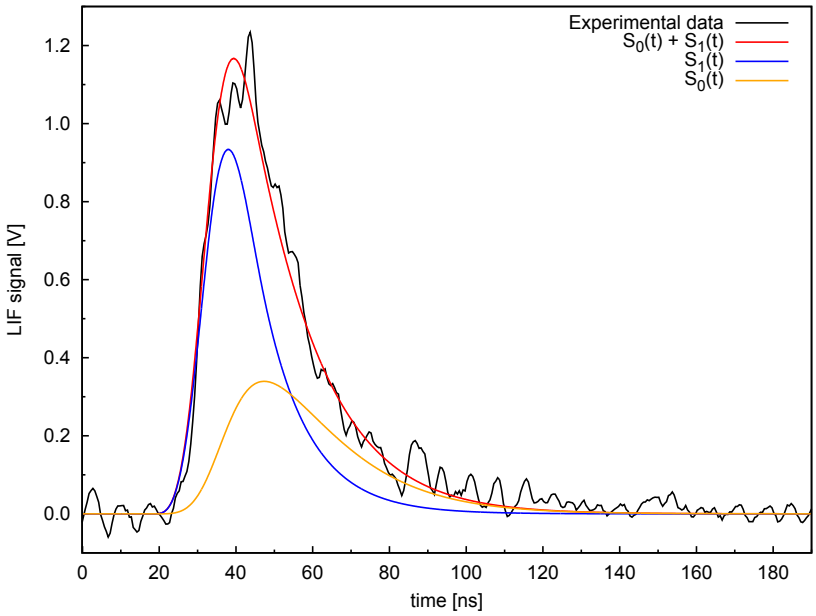

Figure 3.12: Fluorescence pulse as a function of time. The pulse is obtained averaging 200 values for the transition $Q_2(3)$. The simulated fluorescence signal $S(t)$ and its components $S_0(t)$ and $S_1(t)$ are calculated for [OH]$= 2.52 \times 10^{14}\,\mathrm{cm}^{-3}$, OH rotational temperature $T = 500\,\mathrm{K}$, air pressure $3.0\,\mathrm{torr}$ and H_2O pressure $2.9\,\mathrm{torr}$.

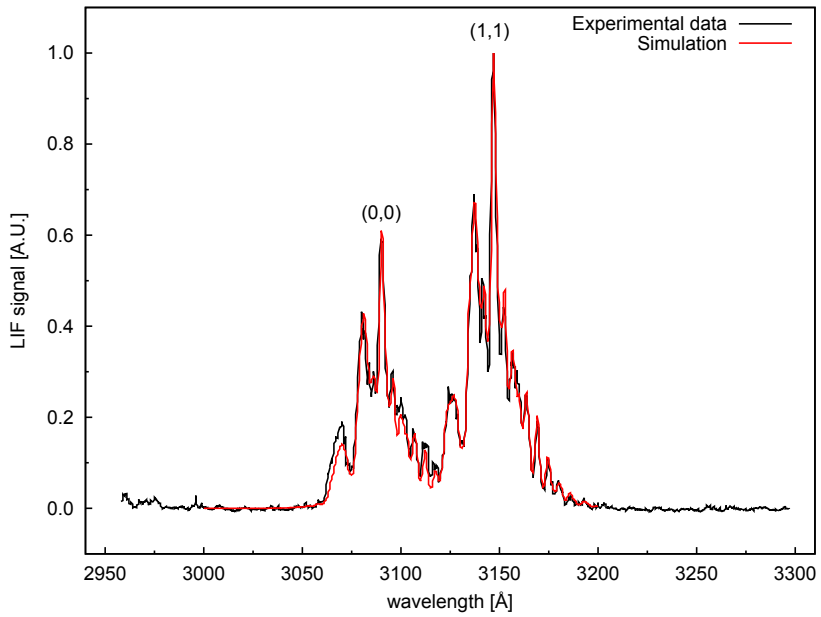

Figure 3.13: Time integrated spectrally dispersed fluorescence. The simulated spectraum is calculated for a rotational temperature $T = 500\,\mathrm{K}$, air pressure $3.0\,\mathrm{torr}$ and H_2O pressure $2.9\,\mathrm{torr}$.

Example of a measured fluorescence pulse and the corresponding simulated values are presented in Figure 3.12. The ICCD measured time integrated spectrally dispersed fluorescence is shown in Figure 3.13.

3.4.3 Spatial energy distribution of the laser beam

The laser beam irradiance is not uniform in the beam section. In the frame of combustion research, in order to get rid of the collision quenching in unknown gas mixtures, the so called saturated fluorescence spectroscopy was proposed [67] , since running LIF in high saturation conditions makes the LIF outcome independent of electronic quenching. Unfortunately true saturation is very difficult to achieve due to the spatial non-uniformity of the beam. Calculations with a 2D gaussian energy distribution:

$$E_{las}(r) \propto \mathrm{e}^{-\frac{r^2}{w_0^2}}, \tag{3.3}$$

were proposed in [74], showing a logarithmic dependence of the LIF outcome on the laser energy. In [67] the effect of top-hat, triangular, lorentzian and gaussian profiles were tested. In our case, the use of a spatial filter to clean the laser beam can give out an almost gaussian

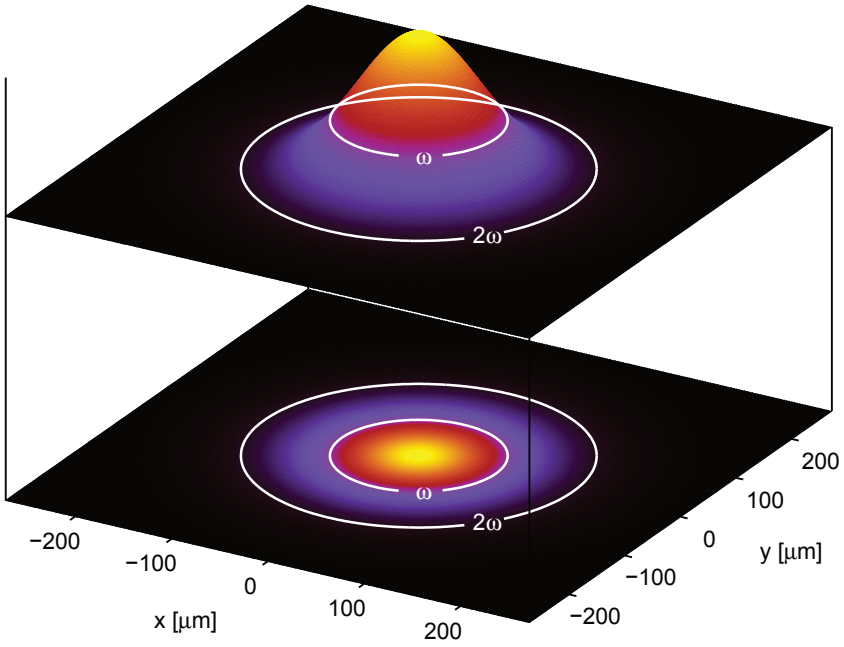

Figure 3.14: 3D and 2D plot of gaussian beam profile, $w = 80\mu m$.

beam distribution. This should be verified experimentally. We have not actually the possibility to perform such a test, then we use a gaussian distribution as a reasonable assumption for pointing out the effects of a spatial distribution.

First we point out that the functional dependence of Eq. 3.3 is normally used in textbooks for the electric field of a gaussian beam, implying for energy related quantities the form $\mathrm{e}^{-\frac{2r^2}{w_0^2}}$, i.e. still a gaussian with half the waist of the electric field. We have chosen Eq. 3.3, as in [74], since any method for visualising the beam, being it a trace on photographic paper or a true measurement, is sensitive to the energy, not to the electric field, so that w_0 is more immediately correlated to the measured/estimated beam size. Integrating Eq. 3.3 over r and over the whole 2π angle we get that the energy within a circle of radius R is:

$$E_R = E_{las}\left(1 - \mathrm{e}^{\frac{-R^2}{w_0^2}}\right),$$

so that the energy flowing through the annulus with surface $S_{1,2}$ enclosed within the radii

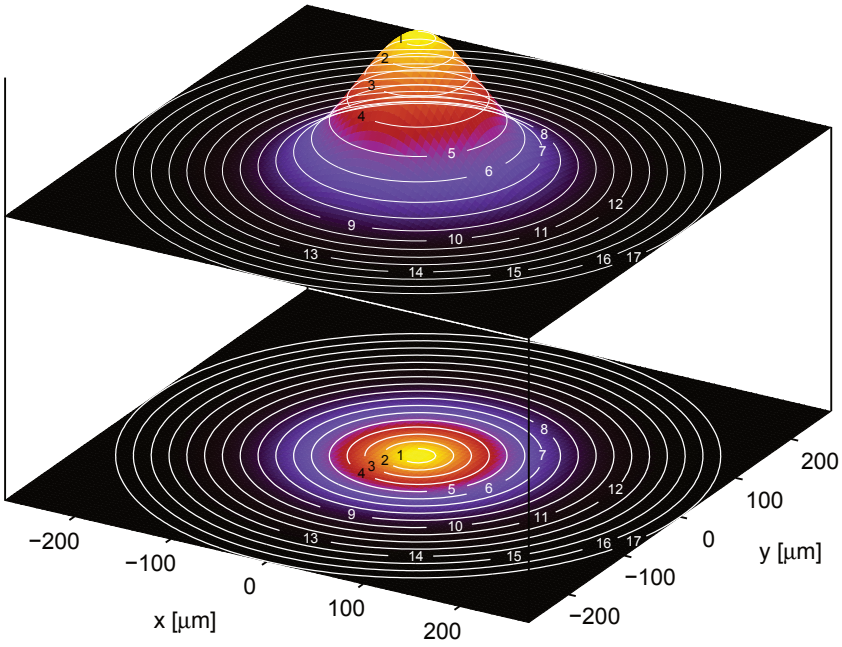

Figure 3.15: 3D and 2D plot of gaussian beam profile, $w = 80\mu m$, with the 17 annuli used in order to estimate the LIF outcome.

R_1 and R_2 is:

$$E_{1,2} = E_{las}\left(\mathrm{e}^{-\frac{R_1^2}{w_0^2}} - \mathrm{e}^{-\frac{R_2^2}{w_0^2}}\right),$$
$$S_{1,2} = \pi(R_2^2 - R_1^2).$$

With this distribution we have a central region, (circle with $r \leq w_0$) with 63.2 % of the energy, an intermediate region (annulus with $w_0 \leq r \leq 2w_0$) with 35 % of the energy, and a peripheric region ($r \geq 2w_0$) with 1.8 % of the energy (see Figure 3.14). We treat the calculation with a gaussian beam as follows. We discretise the radius into 17 values up to $3.4 \times w_0$ (see Figure 3.15). For each circular corona we solve numerically the model 3.2, with a radiant energy density given by

$$\mathcal{E}_L^{(i,i+1)} = \frac{W(t)}{cS_{i,i+1}}\left(\mathrm{e}^{-\frac{R_i^2}{w_0^2}} - \mathrm{e}^{-\frac{R_{i+1}^2}{w_0^2}}\right),$$

and we then sum up the model outcomes over all the annuli ($P_{i,i+1}$), weighted by a number proportional to the sampled volume fraction:

$$P_{A1}(t) = \frac{1}{\pi w_0^2}\sum_{i=0}^{16} P_{i,i+1}S_{i,i+1}.$$

The volume fraction is equal to the surface fraction, the other dimension being determined by the slit width. Normalisation to the waist surface makes this factor adimensional and loads the sampled volume into the calibration constant. In practice at large radii, although the energy is very low, the contribution to the LIF outcome is still significant due to the larger volume fraction. This is particularly true when the energy is large, and the beam core is highly saturated.

3.4.4 Collision data

Total quenching rates of level $(A, \upsilon = 0)$, Q_{A0}, level $(A, \upsilon = 1)$, Q_{A1}, and the VET rate from $\upsilon = 1$ to $\upsilon = 0$, $R_{(1\rightarrow 0)}$ can be calculated with good accuracy in He/Ar + H_2O + air since rate coefficients for these gases are well known. The data are reported in Table 3.1.

RET rates in the A state are dependent on the rotational level and on the collider molecule, and have been investigated mainly for $(A, \upsilon = 0)$. Calculations for $N = 1 - 5$ are reported in [84], that agree quite well with the measurements of [85]. For $(A, \upsilon = 1)$ measurements exist only for $F_1(4)$ $F_2(5)$ with various colliders [86]. In that paper it was observed that RET rate coefficients are very similar in magnitude to those of $(A, \upsilon = 0)$. We then use for our calculations the theoretical values reported in [84]. In the conditions of the calibration cell and of the jet used for the saturation curve, the dominant RET contribution is from He collisions. Total RET rate coefficients for collision with He are $2.01 \times 10^{-10}\,\mathrm{cm^3\,s^{-1}}$ for $F_1(1)$ and $1.37 \times 10^{-10}\,\mathrm{cm^3\,s^{-1}}$ for $F_1(2)$. Then, for $Q_1(1)$ line $K_{A_R} = 4.9 \times 10^9\,\mathrm{s^{-1}}$, and for $P_1(3)$ line $K_{A_R} = 3.3 \times 10^9\,\mathrm{s^{-1}}$. RET rate coefficients in the ground state are not well known, but are thought to be slightly larger than those of the A state [87]. In [88] the recovery rate of an initially depleted level of the X state was measured in various combustion mixtures at high temperature. For low N level rates of the order of $(3-6) \times 10^9\,\mathrm{s^{-1}}$ where found, almost independent of the gas mixture. We have chosen to use $K_{X_R} = 4 \times 10^9\,\mathrm{s^{-1}}$. Note that we have verified that K_{X_R} and K_{A_R} values larger than about $2 \times 10^9\,\mathrm{s^{-1}}$ do not modify appreciably the results of the model calculations. The addition of molecular gases generally increases RET rates, so that this choice of RET rates can be applied also to cases with a significant presence of molecular gases.

Table 3.1: Rate coefficients for $OH(A^2\Sigma^+, \upsilon = 0, 1)$ total collision quenching (Q + VET) and $1 \rightarrow 0$ vibrational relaxation at T=300 K by He, Ar, N_2, O_2 and H_2O (10^{-11} cm^3 s^{-1}). Radiative rates are also reported (from [63]).

	v=0	v=1	$1 \rightarrow 0$	$ref.$
He		0.004 ± 0.0015^a	0.002^a	[34]
			0.13 ± 0.04	[75]
Ar	$\leq 0.03^a$	0.3^a	0.27^a	[34]
			0.41 ± 0.03	[76]
			0.32 ± 0.04	[75]
N_2	2.8 ± 1.2^a	23.6 ± 1.5^a	23.3 ± 2.2^a	[76]
	2.7 ± 1.0			[77]
		24.1 ± 1.3	21.1 ± 2.1	[78]
		19 ± 1.5	24 ± 3	[79]
			14	[80]
H_2O	68.0 ± 6.1^a			[81]
	69.1 ± 5.0			[82]
		66 ± 4^a	≤ 12	[79]
			7.3 ± 0.5^a	[76]
O_2	9.6 ± 1.2	20.6 ± 1.5	2.1 ± 0.2	[76]
	9.2 ± 1.5			[77]
		20.2 ± 1.6	3.3 ± 0.7	[78]
		17	1.5	[80]
rad.	(s^{-1})	(s^{-1})		
A_{tot}	1.458×10^7	1.329×10^7		[83]
$A_{(0,0)}$	1.451×10^7			LIFBASE database
$A_{(1,1)}$		8.678×10^6		LIFBASE database

[a] Value recommended in [34]

3.5 Quantitative analysis

3.5.1 Saturation characteristics and calibration constant

Absolute LIF measurements require a calibration that is basically needed for the determination of the $\mathcal{C}V_s$ product. Many methods have been proposed, a survey of which can be found in [63]. In ATP plasma jets we have two examples in the literature. In [51] the calibration constant was determined by Rayleigh scattering on air molecules in open air. In [14] a DBD discharge was placed in the same position as the plasma jet and used as a source of OH, whose concentration had been previously determined by TR-BBAS. In [69] various OH calibration methods are compared. Although tested in a nanosecond pulsed plasma filament, these methods are useful for plasma jets too, and indeed for any ATP discharge type. Result from Rayleigh scattering, broadband absorption on the tiny plasma filament, and from a chemical model in the afterglow were compared in that paper.

In the present work we have used a calibration cell as in [14]. The calibration has been performed for the two laser conditions, i.e. with and without focusing lens. Measurements have been taken in the conditions of Figure 5.1 i.e in a discharge with $[\mathrm{H_2O}] = 0.56\%$, 4.5 mm inter-electrodes gap and six different values of discharge power. Laser pulse energy of about $5.3\,\mu$J (not focused) and $0.4\,\mu$J (focused) have been used with $\mathrm{P_1}(3)$ line excitation. The LIF outcomes have been compared to the OH densities of Figure 5.1 [8] to get the value of the product $\mathcal{C}V_s$.

The methodology of a calibrated LIF measurement is based on the measurement in a well characterised condition and on the extrapolation of the calibration to a range of different conditions. Such an extrapolation requires the LIF model description to be robust with respect to the change of parameters - collision processes, laser beam energy, gas temperature - that can affect the LIF outcome. The model must then be tested by comparing its outcomes to saturation curves, i.e. LIF signal vs. laser pulse energy.

In the unfocused case shown in Figure 3.16, calculations with full account of RET collisions show a reasonable agreement with experiments for a beam waist $w_0 = 750\,\mu$m. In the same figure, the effect of partial or total elimination of RET from the model is also shown. We can define as “linear” regime the condition in which model calculations are independ-

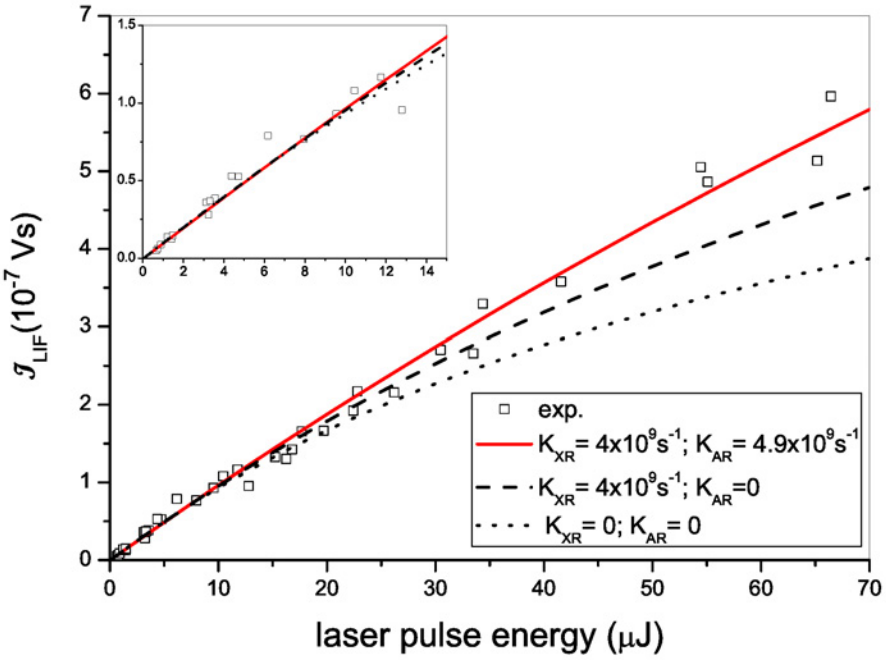

Figure 3.16: $\mathcal{I}_{LIF}$ versus laser pulse energy - unfocused beam, $Q_1(1)$ excitation. He+[H_2O]=0.23% , discharge power density of 10 W cm^{-3}. The red curve is calculated with full account of RET in the ground and $A1$ states. To show how RET affect the saturation curve, calculations without RET in the $A1$ state and without RET at all are also shown.

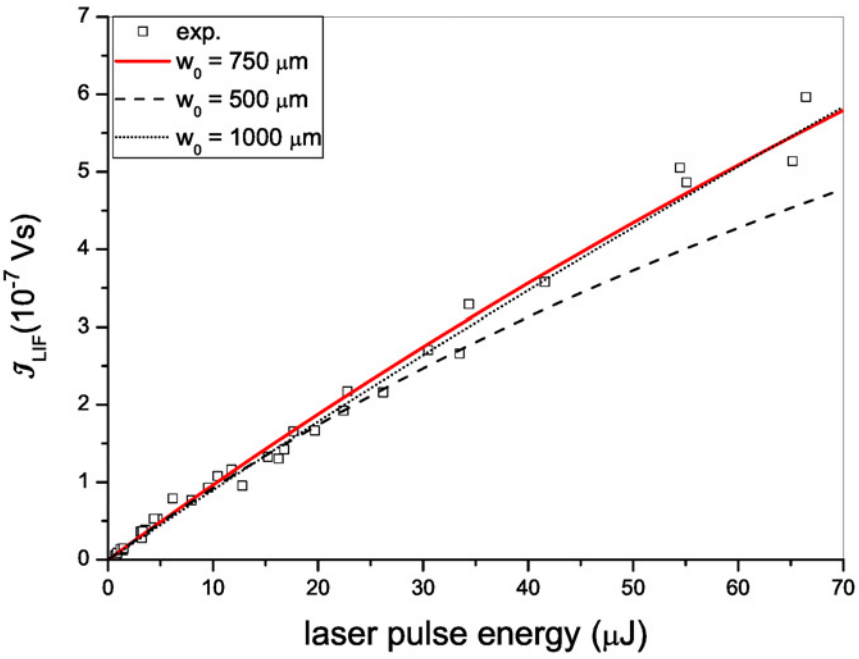

Figure 3.17: $\mathcal{I}_{LIF}$ versus laser pulse energy - unfocused beam, $Q_1(1)$ excitation. He+[H_2O]=0.23%, discharge power density of $10\,\mathrm{W\,cm^{-3}}$. Influence of the w_0 value on the saturation curve.

ent of RET collisions, i.e. in which calculations with $K_{X_R} = K_{A_R} = 0$ are almost equal to those with any RET rate. In other words in the linear regime the fraction of population pumped to the excited state is so low that any refill process is negligible. Such a linear regime is achieved up to, roughly, $8\,\mu$J per pulse.

Both the treatment of RET collisions and the spatial pattern of the beam are approximated. With our choice of RET treatment, the $w_0 = 750\,\mu$m value gives a good agreement with experiments as it is shown in Figure 3.17, where calculations with other w_0 values are presented. On the other hand, setting to zero the RET rates, a good agreement with the experimental data can still be achieved by increasing the beam size, as it is shown in Figure 3.18. This is however achieved at a non realistic w_0 value of 2 mm. We then conclude that both spatial non-uniformity and RET collisions must be taken into account, and that reasonable values of the parameters must agree with the 2 mm diameter experimentally estimated beam size. Finally we show in Figure 3.19 the contribution of the central, intermediate and peripheric space regions to the signal. Most of the LIF signal comes from $r < 2w_0$, while, as expected, non linearity is concentrated in the $r < w_0$ circle.

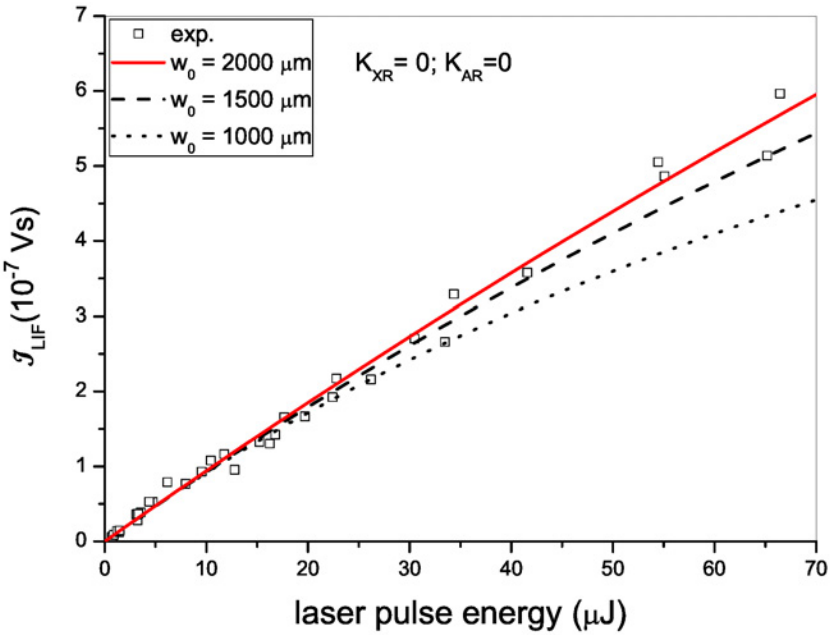

Figure 3.18: $\mathcal{I}_{LIF}$ versus laser pulse energy - unfocused beam, $Q_1(1)$ excitation. He+[H_2O]=0.23%, discharge power density of $10\,\mathrm{W\,cm^{-3}}$. Saturation curves calculated with RET rates set to zero. A good agreement is achieved at $w_0 = 2\,\mathrm{mm}$ (red curve).

In the focused beam case all these characteristic are much more evident. The smaller beam section implies about two orders of magnitude larger radiant energy densities, so that the linear regime is achieved at energies lower than $0.1\,\mu\mathrm{J}$. Working at these low energies is disadvantageous, since then the LIF signal is very low due to the corresponding two orders of magnitude smaller sampled volume. To deal with sufficient signal, then, we must operate the experiment in a partially saturated regime, where all the RET and spatial effects are very important. The saturation curve in the calibration cell is shown in Figure 3.20, together with model calculations with $w_0 = 80\,\mu\mathrm{m}$ and the same RET rates as in the unfocused case. A good agreement is observed up to $15\,\mu\mathrm{J}$. Note also that the first part of the curve might even be fitted by a linear function, showing that saturation curves in a limited energy range can be erroneously interpreted as a linear regime with a small offset (y axis intercept) due to an unidentified background in the LIF outcome, or an offset in the pulse energy measurement system. The deviation from model calculations at high energies may be due to the presence of very low energy spatial "wings" of the laser beam. These might be caused by reflections of the laser beam by the inner surfaces of the optical windows. In order to exclude such

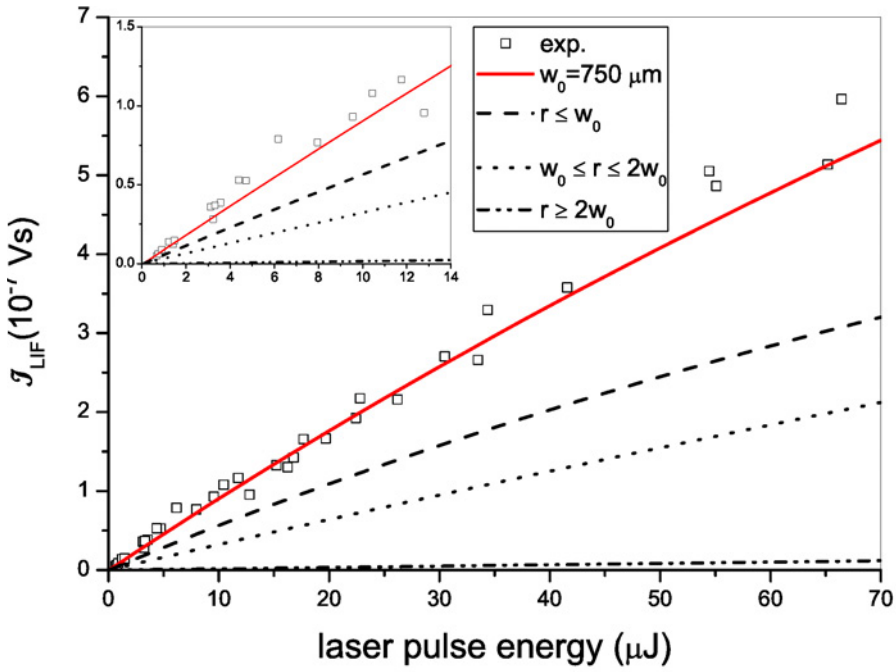

Figure 3.19: $\mathcal{I}_{LIF}$ versus laser pulse energy - unfocused beam, $Q_1(1)$ excitation. He+[H_2O]=0.23%, discharge power density of 10 W cm^{-3}. Contribution of the central, intermediate and peripheric laser beam regions.

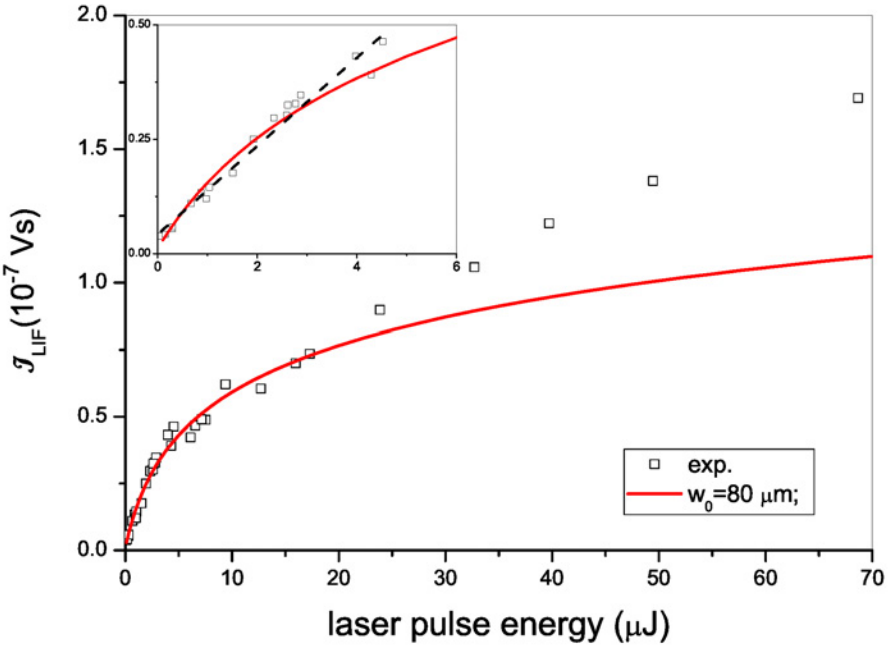

Figure 3.20: $\mathcal{I}_{LIF}$ versus laser pulse energy - focused beam, $Q_1(1)$ excitation. He + [H_2O]=0.23%, discharge power density of 10 W cm^{-3}. The red curve is the model calculation with $w_0 = 80\,\mu$m, $K_{X_R} = 3 \times 10^9\,\mathrm{s}^{-1}$, $K_{A_R} = 1.2 \times 10^9\,\mathrm{s}^{-1}$. In the inset figure the dashed line is a linear fit of the low energy part of the saturation curve.

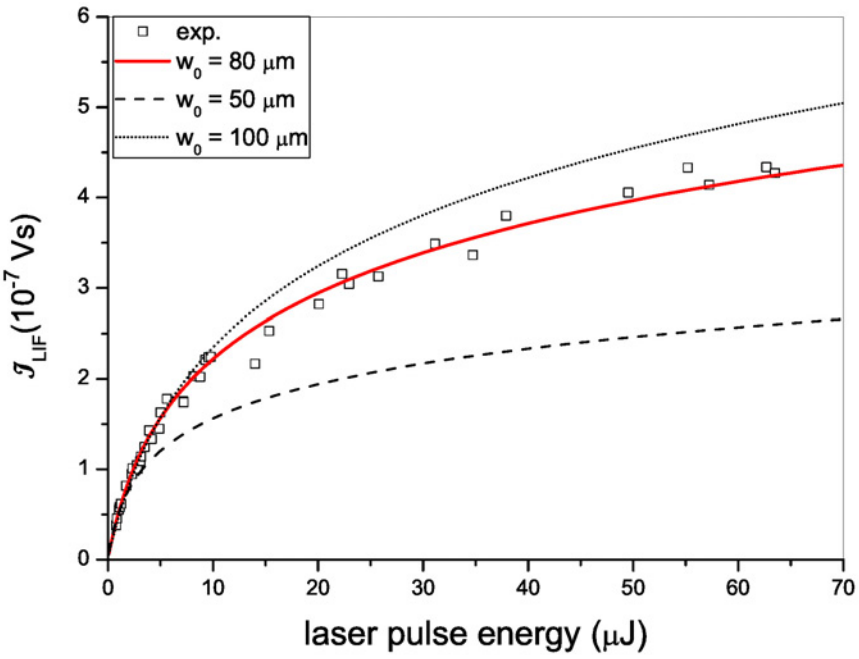

Figure 3.21: $\mathcal{I}_{LIF}$ versus laser pulse energy - focused beam, $P_1(3)$ excitation. He plasma jet with 3.1 torr H_2O and 3.2 torr of air. Calculations are made with three values of w_0

an occurrence, we have measured the saturation curve also in the plasma jet, where the absence of windows on the laser path and the small volume of the active plasma region exclude this possibility. No difference has been observed between saturation curves in the reference cell and in the plasma jet. Such a spurious effect can then be excluded. Another possibility is that, tuning on the $Q_1(1)$ line, spectral wings of the laser line can be absorbed by the adjacent $Q_{12}(1)$. We have then measured the saturation curve also on the isolated $P_1(3)$ line. Note that the two lines have similar absorption coefficients, namely 1.772 and $1.604 \times 10^{17}\,\mathrm{m^3\,J^{-1}\,s^{-2}}$, respectively. A small difference between the two cases shows the presence of a small linear contribution due to absorption by the $Q_{12}(1)$ line. We have then tested the model on the $P_1(3)$ saturation curve.

Figure 3.21 shows results of model calculations with full RET account. A good agreement is achieved for $w_0 = 80\,\mu\mathrm{m}$. As in the unfocused case we show the effect of RET collisions in Figure 3.22, and, in Figure 3.23, how an agreement can be reached without the RET collisions with larger, non realistic w_0 values. The choice of $w_0 = 200\,\mu\mathrm{m}$ is then made since such a value is closer to the calculated waist. In practice, in the focused case we

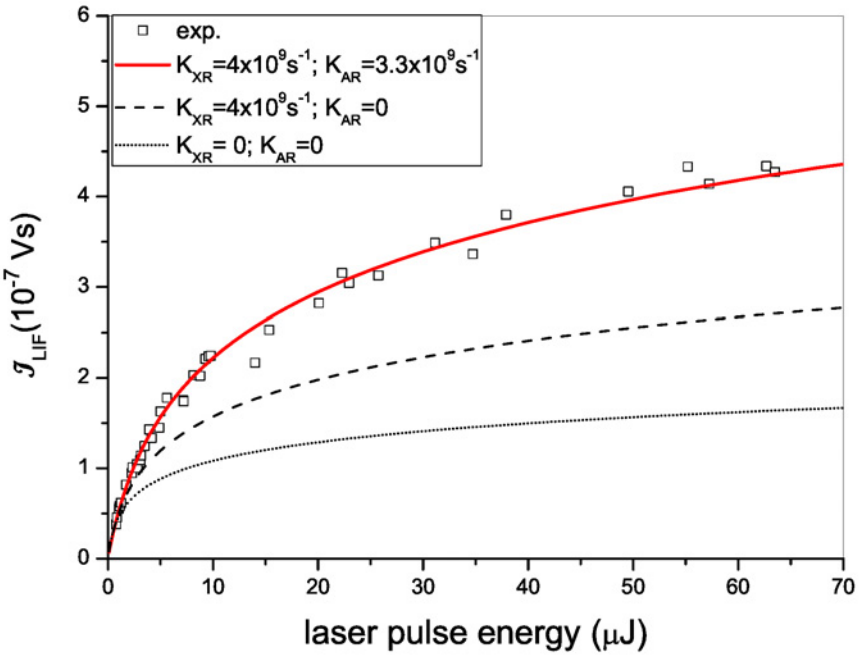

Figure 3.22: $\mathcal{I}_{LIF}$ versus laser pulse energy - focused beam, $P_1(3)$ excitation. He plasma jet with 3.1 torr H_2O and 3.2 torr of air. The red curve is calculated with full account of RET in the ground and $A1$ states. To show the effect RET on the saturation curve, calculations without RET in the $A1$ state and without RET at all are also shown.

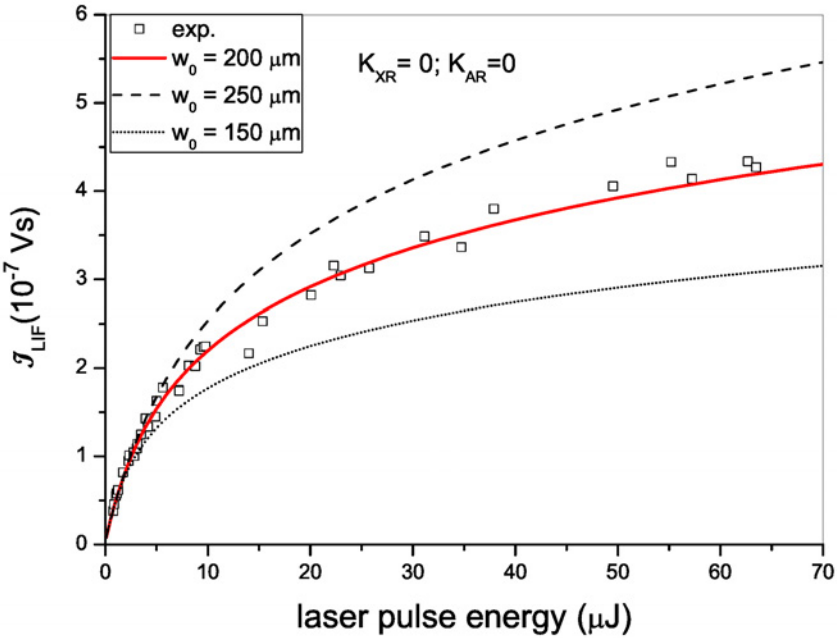

Figure 3.23: $\mathcal{I}_{LIF}$ versus laser pulse energy - focused beam, $P_1(3)$ excitation. He plasma jet with 3.1 torr H_2O and 3.2 torr of air. Saturation curves calculated with RET rates set to zero. A good agreement is achieved at $w_0 = 200\,\mu m$ (red curve).

use the $P_1(3)$ saturation curve in the jet to fix a reasonable value of w_0 and then the $Q_1(1)$ measurements in the calibration cell to get the calibration constant.

Finally, with $K_{X_R} = 3 \times 10^9\,s^{-1}$, $K_{A_R} = 1.2 \times 10^9\,s^{-1}$, we get:

$$\mathcal{C}\tilde{V}_s = (1.8 \pm 0.5) \times 10^{-18}\,V\,cm^3\,s \qquad w_0 = 750\,\mu m \qquad unfocused$$
$$\mathcal{C}\tilde{V}_s = (3.8 \pm 1.1) \times 10^{-20}\,V\,cm^3\,s \qquad w_0 = 80\,\mu m \qquad focused$$

where $\tilde{V}_s$ has here the meaning of an "effective" volume.

For the focused case also we show in Figure 3.24 the contribution of the central, intermediate and peripheric space regions to the signal. At energies roughly below $1\,\mu J$ the contribution of the peripheric region is negligible, and the spatial resolution is within $2w_0$. At higher energy the increase of LIF signal is obtained also at the expense of a lower spatial resolution.

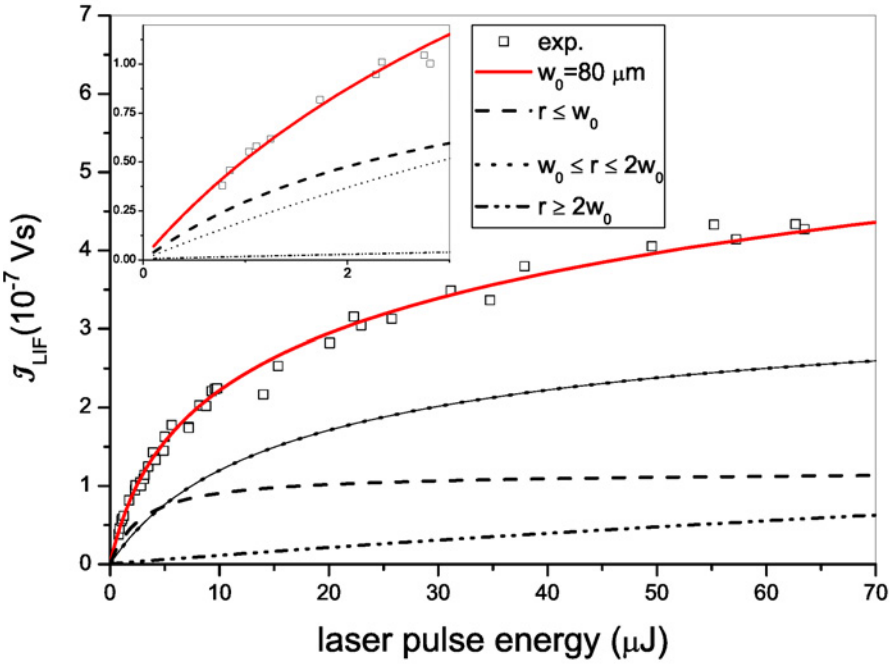

Figure 3.24: $\mathcal{I}_{LIF}$ versus laser pulse energy - focused beam. $P_1(3)$ line, He plasma jet with 3.1 torr H_2O and 3.2 torr of air. Contribution of the central, intermediate and peripheric laser beam regions.

3.5.2 Gas mixture composition

LIF is a suitable diagnostic technique for strongly inhomogeneous media, like Plasma Assisted Combustion or Plasma Jet systems. One such inhomogeneity is in the local gas mixture composition. The local collision rates involved in Eq. 3.2 must be known. These can be obtained by measuring simultaneously the fluorescence pulse $S(t)$, the decay of which is a measure of the total electronic quenching rate, and the fluorescence spectrum $\mathcal{I}_{LIF}(\lambda)$, in particular the ratio of the two fluorescence bands, from which the vibrational relaxation rate can be inferred. This is sufficient for quantitative LIF measurements, without the need of a detailed knowledge of the gas mixture composition. If rate coefficients are well known, however, it is possible to infer the gas composition using the collisional data measured by LIF. In [52] for a plasma jet expanding into free air the total electronic quenching was measured from the LIF pulse decay, and the concentration of humid air penetrating into the jet was calculated for a fixed air plus water vapour mixture. A plasma jet expanding into ambient humid air and hitting a liquid surface, instead, has not a fixed humid air

composition. Air and H_2O partial pressures must be determined independently. Since the collision rate constants are well known (see Table 3.1), the gas composition can be measured, and then accounted for in the LIF outcome, on the basis of the collision quenching and vibrational relaxation. It was demonstrated by Dilecce [19] that a unique He + air + H_2O mixture composition corresponds to a given couple of electronic quenching and vibrational relaxation rates values. Here we implement this idea by measuring at each spatial position both $S(t)$ and $\mathcal{I}_{LIF}(\lambda)$ and fitting them by the model 3.2 using the concentrations of air and water vapour as parameters. The electronic quenching is given by the decay of $S(t)$, while the ratio of the integrated emissions from the two bands depends on the VET rate. Examples of measured and simulated $S(t)$ and $\mathcal{I}_{LIF}(\lambda)$ in a jet at different positions cases are shown in the figure 3 of [14]. Such method has been applied for the first time in [14] to a pulsed HV Plasma Jet (Plasma Gun) hitting a humid surface.

3.5.3 Gas temperature measurement

The gas temperature is an important parameter to be taken into account to rationalise LIF outcomes. It determines both the initial population of the absorbing rotational state and the line width, which in turn affects the overlap integral ψ. In discharges that do not develop a high gas temperature, say less than 400 K, like the pulsed DBD of our calibration cell, or the pulsed plasma gun in [14], a space resolved measurement of the local temperature is not strictly necessary if the laser excitation scheme involves low N levels since the population, as well as the overlap integral, do not change appreciably. On the contrary, cases in which the gas temperature is higher, like a RF plasma jet, require a local measurement of the gas temperature. The safest way to measure the rotational temperature of $OH(X, \upsilon = 0)$ is to fit the LIF excitation spectrum by a synthetic spectrum, like in [89] or in [58]. This kind of measurement usually involves largely spaced rotational lines, and is then quite time consuming and/or affected by a large error. In order to get a better accuracy in a shorter time, and thanks to the quite narrow bandwidth of our laser, we choose to measure excitation spectra that, in a short spectral interval, include the closely spaced $Q_{12}(1)$, $Q_2(1)$, $Q_1(6)$, $Q_{12}(3)$ and $Q_2(3)$ lines. One such spectrum, taken in the conditions of the calibration cell, is shown in Figure 3.25. This methodology allows a good accuracy. From the spectrum of

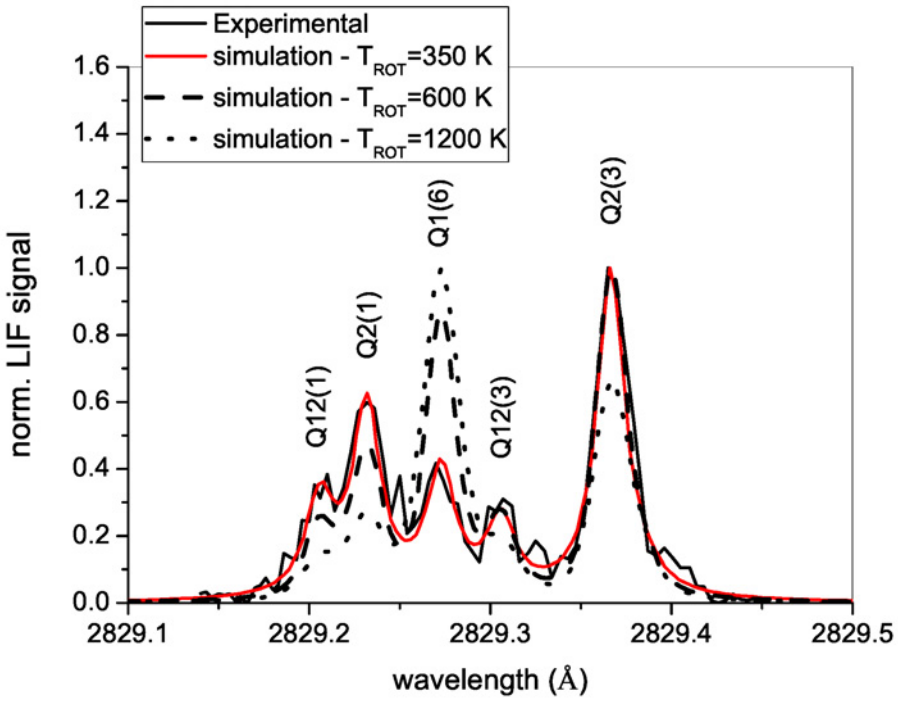

Figure 3.25: LIF excitation spectrum and model simulation for the measurement of the gas/rotational temperature. Simulated spectra at high temperature are also plotted to show how the spectrum changes on rising significantly the temperature.

Figure 3.25 a ± 10 K error can be estimated. The sensitivity at higher temperatures remains large, as it is shown in Figure 3.26 where the peak intensity ratios are shown as a function of temperature up to 1200 K. The time required for completing the wavelength scan is about 7 min. The correct measurement of excitation spectra would require to work rigor-

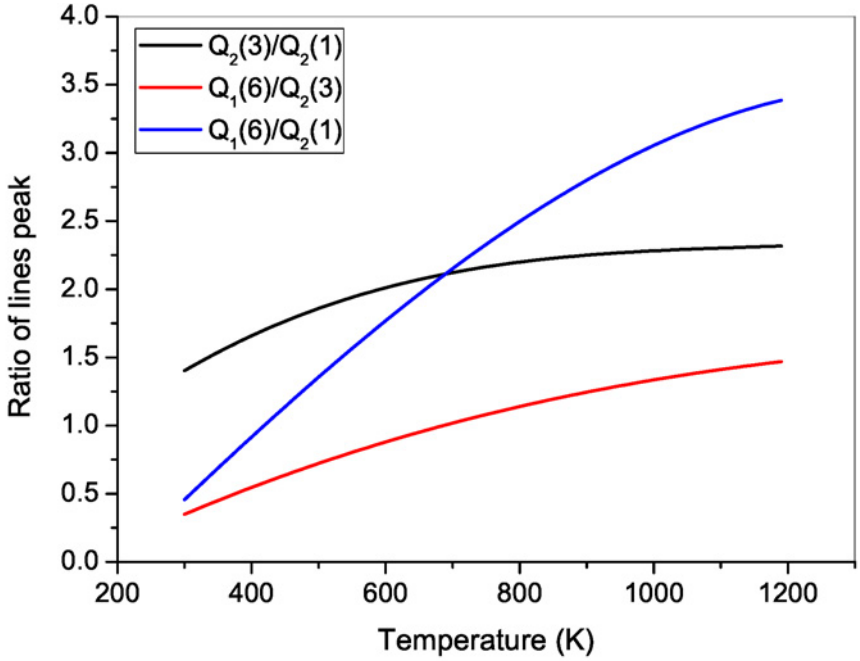

Figure 3.26: Ratio of the main lines peak intensity in the spectrum used for temperature measurements. The ratios are calculated from LIFBASE spectra simulations.

ously within the linear regime. In our case we can work also in partially saturated regime. A correction for non-linearity is in fact possible since the model correctly reproduces the saturation characteristics, taking into account the difference in the absorption coefficients of the various transitions. We remind that a difference in the absorption coefficient is equivalent to a difference in the laser energy. Nevertheless, looking at the absorption coefficients in Table 3.2, we observe that the most important lines, $Q_2(1)$, $Q_1(6)$ and $Q_2(3)$, have similar absorption coefficients, so that working in a weak saturation regime does not imply large temperature errors. The fitting temperature of the spectrum in Figure 3.25 in fact coincides with that measured by TR-BBAS in the calibration cell. On the other hand the remaining lines, $Q_{12}(1)$ and $Q_{12}(3)$, have much lower absorption coefficients, so that in saturation regimes their relative intensity will be overestimated. It is worth mentioning at this point

Table 3.2: wavelengths and absorption coefficients of the lines used for temperature measurements (from LIFBASE database)

line	wavelength (Å)	abs. coeff. ($m^3\,J^{-1}\,s^{-2}$)
$Q_{12}(1)$	2829.21	1.051×10^{17}
$Q_2(1)$	2829.23	2.102×10^{17}
$Q_1(6)$	2829.27	2.852×10^{17}
$Q_{12}(3)$	2829.31	5.441×10^{17}
$Q_2(3)$	2829.37	2.390×10^{17}

that a simpler method is available for the temperature measurement in gas mixtures with prevailing noble gas component, as it is the case in the core of He plasma jets expanding into humid air. Provided the RET rate is much larger than the quenching rate of OH(A) state, rotational equilibrium to the gas temperature is achieved in the fluorescence spectra. This ratio, that is the number of RET collisions in the lifetime of the electronic state, is reported in Figure 3.27. It can be seen that at least up to 10 Torr of air, the number of RET collisions is sufficient for the thermalization of the A state rotational distribution. In the jet periphery, then, where the lifetime is short, the temperature can no longer be deduced from fluorescence spectra.

The spectrum for temperature measurements is made of less intense lines than the low N of Q_1 and P_1 branches, since the low N lines all belong to the F_2 sublevel, that has a smaller population. Nevertheless the spectrum itself can be used for absolute OH concentration measurements performing in this way a simultaneous measurement of both the OH concentration and the temperature.

3.5.4 Errors and the lower detection limit

The adopted calibration strategy corrects for systematic errors which affect detectors and the laser source. All the systematic error contributions can be included in the $\mathcal{C}$ term. Then, the LIF outcome is only affected only by statistical errors, which in turn are taken into account during the fit of the model. The uncertainty in the estimate of the OH density carried out by the TR-BBAS technique, and used to calibrate the LIF apparatus, is the

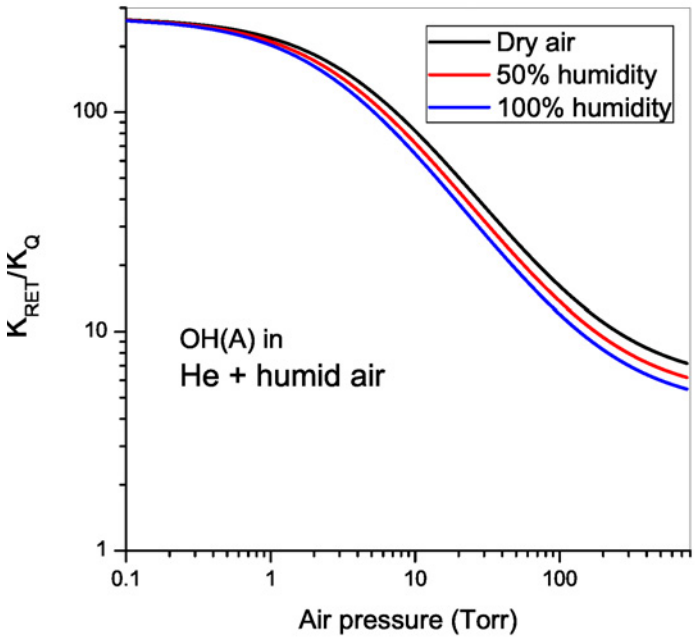

Figure 3.27: Ratio of RET over quenching collision rate as a function of air partial pressure in He buffer gas.

only remaining source of systematic error. The error affecting the LIF outcome is 20% (Chapter 2.3.2).

It is difficult to define a lower detection limit for the LIF technique. The signal depends on the molecule, the density of colliders inside the plasma, the volume sampled, the laser power, the transition used and the temperature. For all these reasons, the lower detection limit has to be estimated case by case.

Chapter 4

Measurement of the electrical power in dielectric barrier discharges and radio-frequency plasma-jets

Current-voltage (I-V) characteristic and Langmuir probes are the most commonly used diagnostics for electrical characterisation of discharges. The power dissipated in the plasma is a critical parameter in order characterise the discharge. Current, voltage, and reactor impedance are generally used to derive the power dissipation and the interaction with the substrate or the sample. An accurate impedance measurement can be interpreted using equivalent electrical circuit models, in order to get insights into the plasma properties, like electron density, dark space thickness, ion energy, and ion current [90]. The relevance of electrical data relies on the fact that they can serve as gauge of how well plasma conditions are replicated among different substrates or between different types of discharges.

4.1 Estimate of the electrical power in a dielectric barrier discharge

Dielectric barrier discharges are considered a source of non-thermal plasmas that can be used in many applications like material processing, ozone production, toxic gas decontam-

ination, plasma assisted combustion, etc. In all these applications, the role of the plasma is to produce high energetic electrons that create highly reactive species, able in turn to trigger a high energy chemistry at low temperature.

Fang *et al.* [91] and De Geyter *et al.* [92] measured the voltage drop across a DBD either by using a voltage divider in parallel with the discharge or a commercial high-voltage probe. Current flowing inside the reactor was estimated by the voltage drop on a resistor placed in series to the DBD. Also the charge stored on the electrodes was measured from the voltage drop across a capacitor. Both the capacitor and the resistor were placed between the discharge and the ground, alternatively connected to the reactor by a switch. A similar arrangement was used by Nersisyan *et al.* [93] in a He DBD, and in our work on the plasma dry reforming [8], where a high voltage probe was connected to the high voltage electrode, and a capacitor-resistor series was placed between the discharge and the ground. In such arrangement, current and the charge deposited on the electrodes can be measured simultaneously.

From the charge-voltage plot, also known as Lissajous figure, it is possible to determine the power dissipated in the plasma [94, 95, 96, 97]. Another method consists in the direct time-integration of the V-I product [91]. In the following section we are going to describe the theoretical background of the re-derivation of the Manley's equation [94] proposed by Falkenstein *et al.* [96] based on the analysis of the Lissajous figure. The discharge power and the electric parameters (gas, dielectric and stray capacitance, breakdown voltage, charge deposited in the electrodes, etc.) of the discharge are determined. The characterisation of a DBD is presented as an example of the model we used.

4.1.1 Theoretical background

Manley [94] considered the charge versus voltage plot and derived expressions for the energy transferred by the discharge into the gas. Falkenstein *et al.* [96] observed that Manley did not consider stray capacitance effects. Stray capacitances do not affect the area of the Lissajous figure, but change significantly its shape. An example of Lissajous figure is shown in Figure 4.1. The peak voltage of the applied sinusoidal signal is defined as V_{peak}, the effective gas breakdown voltage as V_b, the voltage drop through the gas as V_{gas}, the

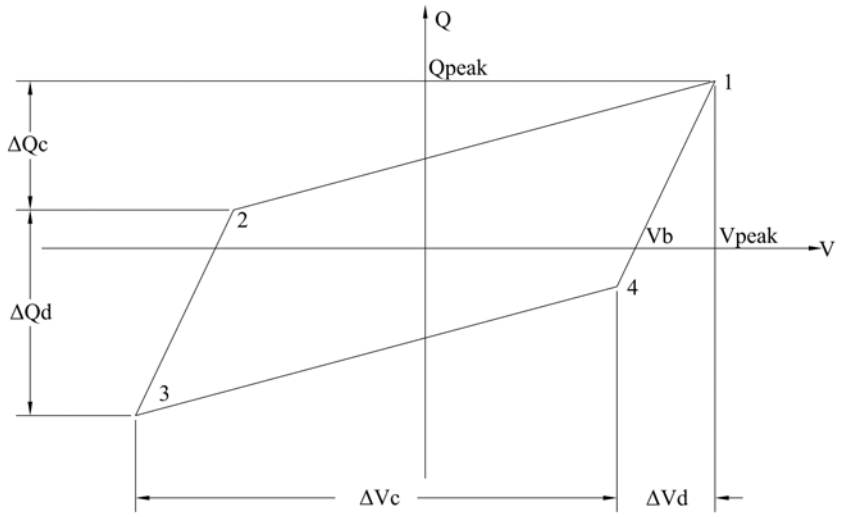

Figure 4.1: Representation of a typical Lissajous figure.

capacitance of the dielectric as C_{die}, and the capacitance of the gas as C_{gas}. If

$$V_{peak} < V_b \frac{C_{die} + C_{gas}}{C_{die}}$$

than there is no discharge and the reactor is purely capacitive. In this case the voltage applied to the reactor V and the charge on the capacitor Q are in phase, thus Q as a function of V is represented by a straight line through the origin with slope $\frac{C_{die}C_{gas}}{C_{die}+C_{gas}}$. If the applied voltage V_{peak} increases above the gas breakdown voltage V_b, a discharge occurs. Then the charge and the voltage are out of phase because a current is established through the gas. The $Q-V$ relationship is shown by the Lissajous figure, in Figure 4.1. By assuming [96] that:

- the charge on the capacitors coincides with the total charge Q;
- V_{gas} remains constant during the discharge;
- the current and voltage probes did not perturb the voltage applied to the reactor;

then:

$$V = V_{die} + V_{gas}$$
$$V_{die} = \frac{Q_{die}}{C_{die}} = \frac{Q}{C_{die}}$$
$$V_{gas} = \frac{Q_{gas}}{C_{gas}} = V_b$$

and

$$Q = C_{die}\left(V - V_b\right). \tag{4.1}$$

Then a linear relation exist between the voltage V and the charge Q as show in Figure 4.1 (Lissajous figure), where the lines 1-4 and 2-3 represent Eq. 4.1, for the two opposite signs of the breakdown potential V_b, respectively. From the slope of the two lines, the value of C_{die} can be calculated while the value of the product $C_{die}V_b$ can be estimated from the intercept with the Q axis. The slopes of 1-2 and 3-4 lines (discharge off) give the value of C_{gas}. The charge necessary for changing the sign of voltage drop through the gas is

$$\Delta Q_c = 2C_{gas}V_b$$

We observe that

$$2\Delta Q_{peak} = \Delta Q_c + \Delta Q_{die}$$

thus

$$\Delta Q_{die} = 2C_{die}\left(V_{peak} - \frac{C_{die} + C_{gas}}{C_{die}}V_b\right). \tag{4.2}$$

Each elementary charge e transfers the energy eV_b to the gas during the discharge. Given that two discharges occur every cycle, the total energy E_{cycle} transferred to the gas every cycle is:

$$E_L^{cycle} = 2\Delta Q_{die}V_b = 4C_{die}\left(V_{peak} - \frac{C_{die} + C_{gas}}{C_{die}}V_b\right)V_b \tag{4.3}$$

The mean electrical power P_L transferred to the plasma can then be obtained by multiplying E_L^{cycle} by the frequency f of the applied voltage. The effect of stray capacitances is implicitly considered in C_{die}

4.1.2 Measurement of the energy

The estimation of the electrical power is carried out either by using the method proposed by Falkenstein *et al.* [96], and by the direct time integration of the I-V product. The values of voltage $V_{HV}\left(t\right)$ and current $I\left(t\right)$, recorded by the oscilloscope, are filtered by a single pole (20 dB dec^{-1}) low pass filter in order to eliminate high frequency noise components.

The charge $Q_C\left(t\right)$ deposited on the electrodes is calculated by integrating in time the current. The integration of weak and noisy signals can be affected by systematic errors, due

to offsets or low-frequency noise. These errors can generate baseline drifts in $Q_C(t)$, which have to be properly subtracted. Starting from $Q_C(t)$ and $V_{HV}(t)$ (Lissajous figure), C_{gas} and C_{die} are estimated by calculating the four slopes in the $Q-V$ plot. The value of V_b is inferred by inverting Eq. 4.2, while the energy is calculated by using (Eq. 4.3). The power is the energy per period multiplied by the frequency of the sinusoidal excitation signal.

$$P_L = E_L^{cycle} f.$$

The second method to estimate the power is based on the I-V law:

$$E_J^{cycle} = \frac{1}{T}\int_0^T I(t)\, V_{HV}(t)\, \mathrm{d}t, \tag{4.4}$$
$$P_J = E_J^{cycle} f.$$

We solve Eq. 4.4 by using the first order Newton–Cotes formula. We also corrected the time series of voltage and current in order to eliminate DC offsets and low-frequency noise.

4.1.3 The power dissipated in a DBD of CH_4 and CO_2

We electrically characterised a DBD of CO_2 and CH_4 at atmospheric pressure [9]. The discharge source consists of a quartz tube (internal diameter 10 mm and external diameter 13 mm) and a coaxial inner metallic electrode of 8 mm of diameter. The annular discharge, between the inner grounded electrode and the outer powered electrode, has a length of 170 mm. The HV power supply is composed of a low voltage sinusoidal generator working at 8 kHz (33220A, Agilent), a power amplifier (UCD2k, Hypex) and a high voltage transformer (Al-T1000.7-P100, Amp-Line). The discharge current is measured by a current monitor (CT-01-b, Magnelab, 200 Hz–500 MHz bandwidth), and the applied voltage by a HV probe (P6015A, Tektronix). Both signals are recorded by an oscilloscope (Infiniium 54831B, Agilent, 600 MHz bandwidth). In Figure 4.2, the voltage and the current as a function of times are presented. The figure shows that the discharge is filamentary. Charge as a function of time is presented in Figure 4.3.

The Lissajous figure is presented in Figure 4.4, fitted by the four red lines. The obtained discharge parameters are presented in Table 4.1. The power determined from the Lissajous figure (P_L) is in agreement with the value calculated by the direct integration of the I-V product (P_J).

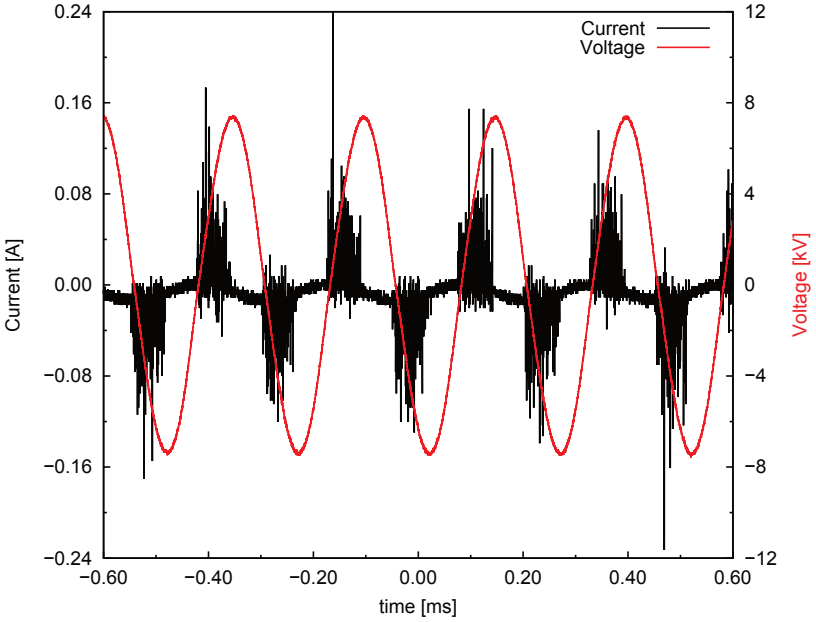

Figure 4.2: Current (black line) and voltage (red line) in function of time for a cylindrical DBD. The inner electrode is in countact with the gas flow (100 sccm CH_4, 100 sccm CO_2) and it is made of copper.

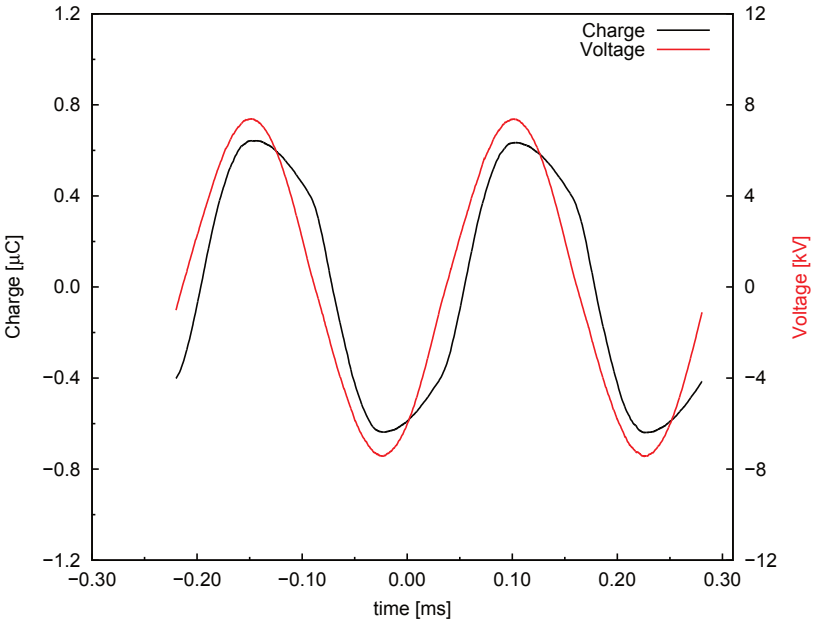

Figure 4.3: Charge (black line) and voltage (red line) versus time.

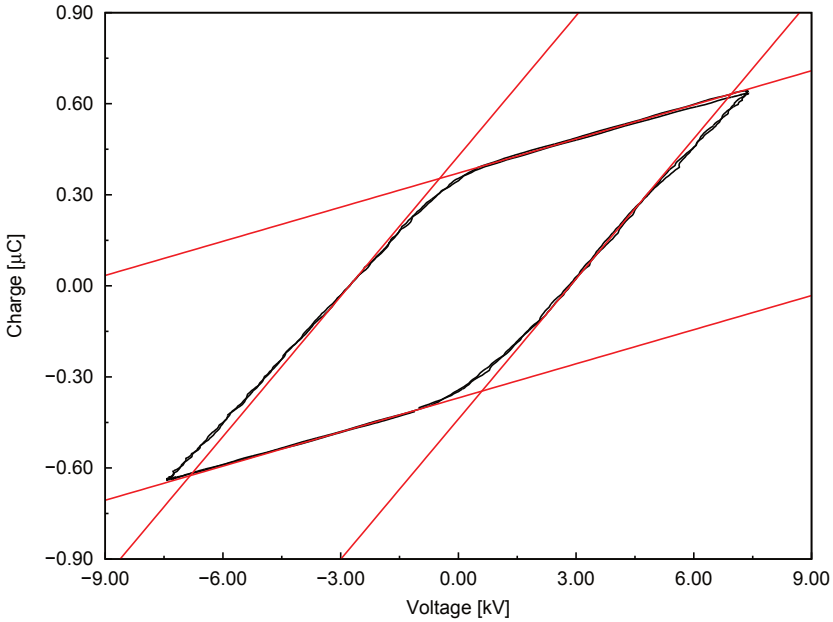

Figure 4.4: Lissajous figure (Q-V plot, black line), and the linear fit (red lines) on the four arms of the plot.

Table 4.1: Program results

Parameter	*Value*	*percent error*
V_{peak}	(7.407 ± 0.002) kV	0.03%
Q_{peak}	(638 ± 3) nC	0.4%
C_{gas}	(49 ± 6) pF	13%
C_{die}	(154 ± 11) pF	7%
C_{tot}	(37.5 ± 0.4) pF	1%
V_b	(3.3 ± 0.3) kV	9%
P_J	(21.7 ± 0.7) W	3%
P_L	(24 ± 6) W	24%

4.2 Estimate of the electrical power in a radio-frequency plasma-jet

In most cases when dealing with radio-frequency plasma jets (RF-PJs), the substrate acts as an electrode and the plasma itself depends strongly on the nature of the substrate. The measurement of the I-V characteristic in inductively (ICPs) or capacitively coupled plasmas (CCPs) is a challenging task, due to the number of significant issues regarding the accuracy of measurement and the extraction of the relevant parameters.

4.2.1 Literature overview

Commercially available directional power meters can be used for monitoring the reflected power [98, 99]. These devices tend to be expensive and with a narrow measurement range and frequency bandwidth.

The use of current and voltage probes in combination with a high-bandwidth oscilloscope appear to be the arrangement of choice for measure the plasma power. In a RF plasma source, the total applied power can be measured in different locations of the electrical setup. Hofmann *et al.* [100] proposed to measure the I-V characteristic of a CCP before the matching network, in order to avoid the influence of capacitance and impedance of the probes. When using this technique, it is generally assumed that power losses in the matching network are small compared to the power absorbed by the plasma itself [101]. This is however questionable.

An alternative approach consist in measuring the I-V characteristic after the matching box, as close as possible to the high-voltage electrode [102, 103, 104, 105, 106, 107].

4.2.2 Theoretical background

The average power of an ac signal can be calculated as the integral over the period T of the voltage-current product:

$$P = \frac{1}{T} \int_0^T V\left(t\right) I\left(t\right) dt$$

For a sinusoidal voltage of frequency $f = \frac{1}{T}$, the power can be expressed in terms of the peak value of voltage (V_p) and current (I_p) (or alternatively of the root mean square value,

V_{rms} and I_{rms}), and the relative phase ϕ between the voltage and the current

$$P = \frac{V_p I_p}{2} cos\phi = V_{rms} I_{rms} cos\phi \tag{4.5}$$

where

$$\begin{aligned} V_{rms} &= \sqrt{\frac{1}{T}\int_0^T V^2(t)\,\mathrm{d}t} = \frac{V_p}{\sqrt{2}}, \\ I_{rms} &= \sqrt{\frac{1}{T}\int_0^T I^2(t)\,\mathrm{d}t} = \frac{I_p}{\sqrt{2}}. \end{aligned} \tag{4.6}$$

In the following, some important hints are given to estimate voltage, current, and phase shift from the experimental data.

The voltage and current time series are corrected by taking into account the time delay introduced by the probe cables and oscilloscope input stage, phase error $\Delta\phi_i$. The correction is performed by adding a time offset to the voltage time series. To this purpose, it is necessary to estimate the phase error (the procedure is described in Chapter 4.2.3) and then to convert it to a time shift Δt_i using the relation

$$\Delta t_i = \frac{\Delta\phi_i}{2\pi f},$$

where f is the plasma operating frequency.

An often neglected problem is connected to systematic errors in the signal time integral due to low-frequency offsets, introduced by the measurement apparatus. To reduce this problem, we renormalised to zero the average values of $V(t)$ and $I(t)$ before time integration of their product.

An alternative procedure method is based on the phase sensitive detection algorithm. The voltage (current) signal is (only ideally) a sine wave $s(t) = s_0 sin(\omega t + \phi)$ with frequency $f = 1/(2\pi\omega)$. By multiplying the signal $s(t)$ with a synthetic signal $r(t) = sin(\omega' t)$ at arbitrary frequency $f' = 1/(2\pi\omega')$ we get:

$$\begin{aligned} s(t)r(t) &= s_0 sin(\omega t + \phi) sin(\omega' t) = \\ &= \frac{s_0}{2}\left(cos\left(\left(\omega - \omega'\right)t + \phi\right) - cos\left(\left(\omega + \omega'\right)t + \phi\right)\right) \end{aligned} \tag{4.7}$$

We observe that when $\omega \neq \omega'$, average value of $s(t)r(t)$ in Eq. 4.7 is zero. If $\omega = \omega'$, one gets a sinusoidal output at frequency 2ω, with a DC offset. Averaging $s(t)r(t)$ on an interval

$k \gg 1/(4\pi\omega)$, one obtains[1]

$$\overline{(s(t)r(t))} = \frac{s_0}{2} cos(\phi) = X, \tag{4.8}$$

Substituting $r(t)$ with $q(t) = sin(\omega' t + \pi/2)$ in Eq. 4.7 and averaging, one gets

$$\overline{(s(t)q(t))} = \frac{s_0}{2} cos\left(\phi - \frac{\pi}{2}\right) = \frac{s_0}{2} sin(\phi) = Y, \tag{4.9}$$

also known as the out-of-phase component Y. From Eq. 4.8 and Eq. 4.9 magnitude of the signal $s(t)$ at the frequency $\omega = \omega'$ can be obtained

$$R = \sqrt{X^2 + Y^2} = \frac{s_0}{2}\sqrt{(cos^2(\phi) + sin^2(\phi))} = \frac{s_0}{2}.$$

The phase ϕ of $s(t)$ with respect to $r(t)$ can be calculated

$$\phi = tan^{-1}\left(\frac{Y}{X}\right).$$

Thus it is possible to extract all the information about current, voltage, and relative phase shift. Concerning the frequency, by the procedure just described, it is possible to calculate the Fourier transform $FT(s(t))$ (Figure 4.5) of the measured signal $s^m(t)$ by varying the frequency ω'.

In RF-PJ (Chapter 3.3.5), the phase shift between voltage and current is a critical parameter for an accurate estimate of the plasma power [102]. The measured phase shift varies between $\phi = -1.48$ rad (plasma-off) and $\phi = -1.40$ rad (plasma-on). By expressing the latter as

$$\phi = -\frac{\pi}{2} + \delta,$$

δ changes between 0.09 rad and 0.17 rad. Then the power (Eq. 4.5) can be expressed as

$$P = \frac{V_p I_p}{2} sin(\delta) \approx \frac{V_p I_p}{2}\delta,$$

$$\frac{\Delta P}{P} \approx \frac{\Delta\delta}{\delta}.$$

As an example, if we want a $\Delta P/P = 5\%$ accuracy in the discharge power, we need to estimate the phase shift with an accuracy larger than $\Delta\delta \approx 4$ mrad, that corresponds to $\Delta t \approx 50$ ps at $f = 13.56$ MHz. In order to estimate with accuracy the plasma jet power, the measurement of V, I and their relative phase shift is therefore a critical issue.

[1] this operation is equivalent to applying a finite impulse response low pass filter. The algorithm proposed is similar to the one implemented in lock-in amplifiers. All the calculations are done in post processing.

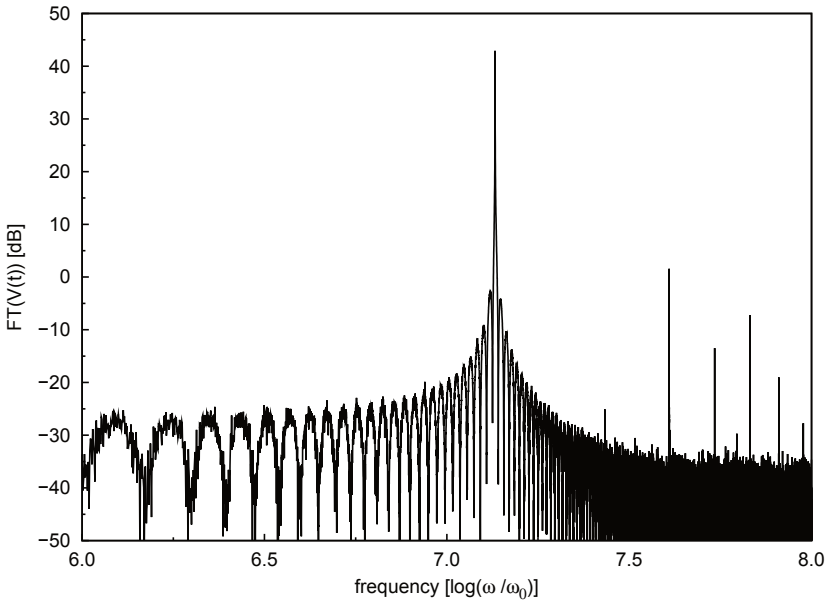

Figure 4.5: Fourier transform of the voltage applied to the RF-PJ of Figure 4.6.

4.2.3 Influence of the probes on the V, I time dependence

The major source of systematic error in the acquisition of the I-V characteristic is due to the probes [90].

In this work we measured the phase error introduced by the measurement apparatus (probes and oscilloscope), by measuring the phase shift for a 13.56 MHz sinusoidal stimulus applied to purely capacitive load (vacuum capacitor) [101].

Data were acquired using a high voltage probe (P6015A, Tektronix) and a high bandwidth (200 Hz to 500 MHz) I/V converter (CT-01-b, Magnelab). Probe output signals were recorded and digitalised with a DSO (Wavesurfer 104MXs-A 1 GHz 5 GSps, LeCroy). A single power measurement consists in the acquisition of 2.5×10^6 points at a sampling frequency of 5 GSps. For the impedance phase error measurement we used a waveform generator (33250A, Agilent) as a 13.56 MHz sinusoidal voltage generator directly connected to a vacuum capacitor. Voltage and current probes were connected between the waveform generator and the capacitor. The phase shift of the voltage respect to the current was calculated using the phase detection algorithm. We obtained a phase shift of $\Delta\phi_i = -0.086$ rad that corresponds to a time delay of 1.00 ns at 13.56 MHz.

Other sources of systematic errors are related to probe and oscilloscope amplitude measurements. The voltage probe has a scale factor accuracy of 3% and the current probe a nominal accuracy of 0.5%. The oscilloscope has a DC gain accuracy of 1.5%. We assume a total nominal accuracy of 4.5% and 2.0% for the voltage and current amplitudes, respectively.

4.2.4 The power dissipated in a RF-PJ of He and O_2

The experimental set-up is described in Figure 4.6. A mixture of He and O_2 flows

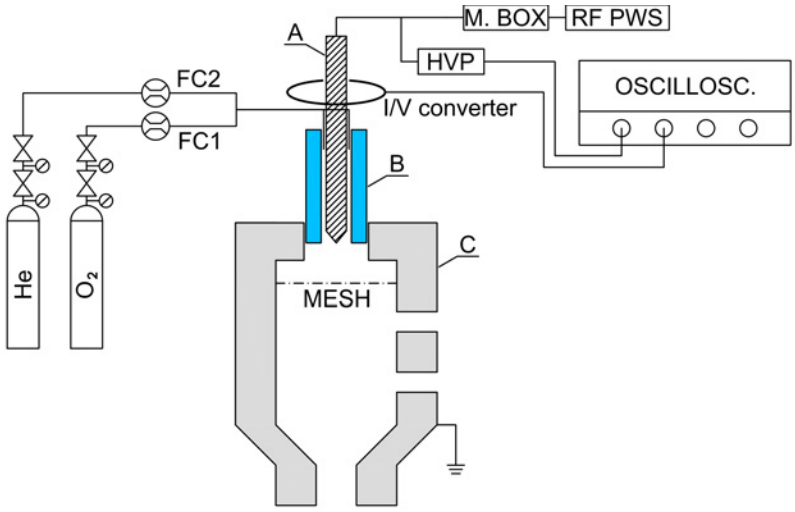

Figure 4.6: Schematic representation of the RF-PJ set-up. A: tungsten electrode; B: quartz tube; C: stainless steel metal chamber; $FC1, 2$: mass flow controller; HVP: high voltage probe; M.BOX: automatic matching network; RF PWS: RF power supply; OSCILLOSC.: oscilloscope.

between the high voltage electrode (a tungsten rod of 1 mm of diameter, 170 mm of length) and a quartz tube (1.5 mm of internal diameter, 3 mm of outer diameter). The two gas feed are controlled by using two mass flow controllers FC1 and FC2 (1179A, MKS). The total flow is set at 2000 sccm, the oxygen concentration can vary between 0 and 4.0% The grounded electrode is a mesh placed in front of the high voltage electrode. The plasma jet diffuses inside a stainless steel metal chamber at atmospheric pressure. A 500 W RF power supply (RF5S, RFPP) working at 13.56 MHz is used to generate the discharge. Impedance matching between the power supply and the plasma jet is achieved by using an automatic matching network (AM5, RFPP). All the measurements presented were recorded without changing

the matching network configuration.

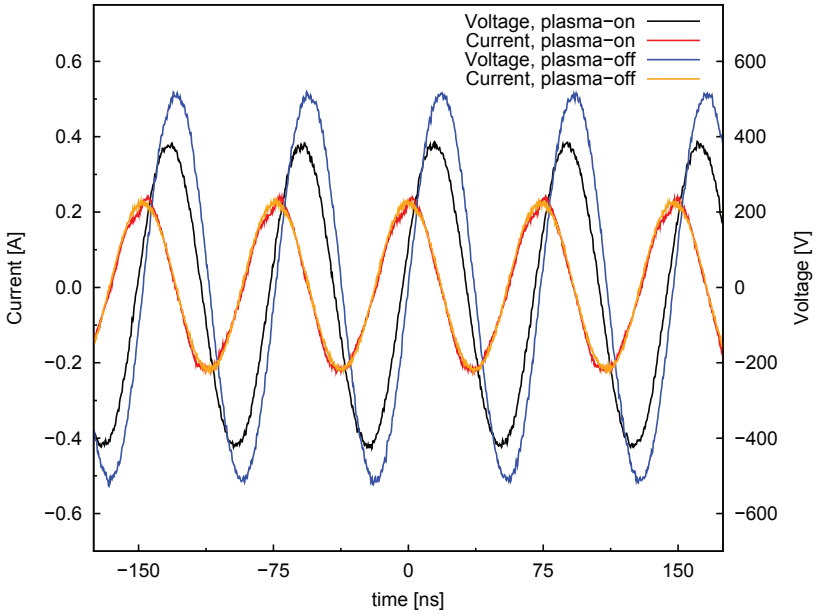

Figure 4.7: Comparison between plasma on and off condition, $I = 157\,\mathrm{A_{rms}}$, 0.0% of [O_2]. Black line: voltage, plasma on; blue line: voltage, plasma off; red line: current, plasma on; orange line: current, plasma off.

A typical I-V plot is presented in Figure 4.7 for plasma-on/off conditions. Plasma off condition is obtained by stopping the gas flow inside the plasma jet.

To compute the power dissipated into the plasma, we measured the I-V characteristic for every gas mixture used ($0.0\ \%$, $0.5\ \%$ and $4.0\ \%$ of O_2) and for different voltages (from 90 to $415\,\mathrm{V_{rms}}$). For every measurement, the quantities V_p, I_p and ϕ were calculated by using the phase detection algorithm. V_{rms} and I_{rms} were also computed by direct integration of Eq. 4.6. For both cases I and V signals were corrected for the impedance phase error. A comparison between the two respective power values is presented in Figure 4.8. A good agreement is observed.

The power as a function of the rms current for three different gas mixtures is shown in Figure 4.9. Without plasma, the increase of the power with the current is explained by the resistive impedance of the plasma jet [105].

The power dissipated in the plasma (Figure 4.10) is calculated as the difference between the plasma-on and plasma-off values (Figure 4.9). It is worth to note that by increasing

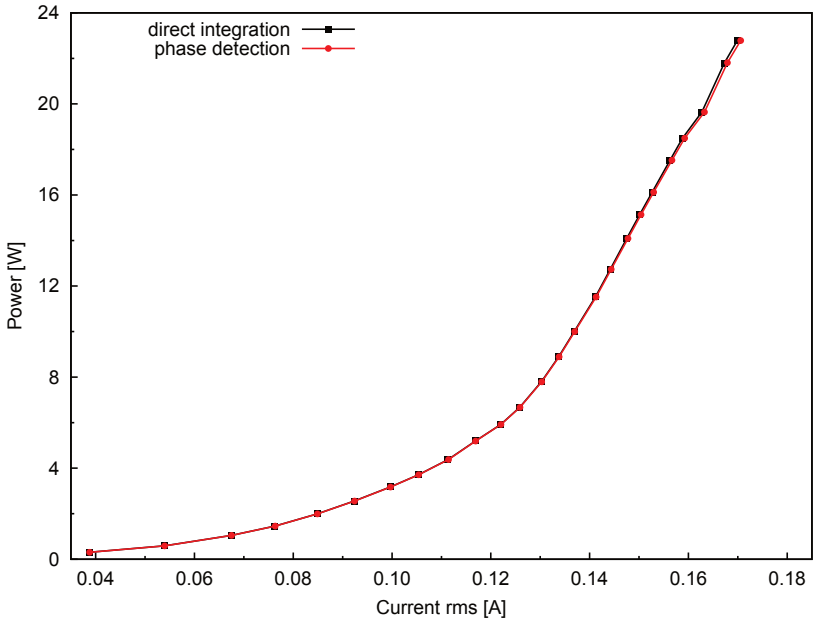

Figure 4.8: Power dissipated in the RF-PJ in function of the rms current flowing in the tungsten needle. Black line: points calculated by integration of Eq. 4.6; red line: points calculate with the phase detection algorithm.

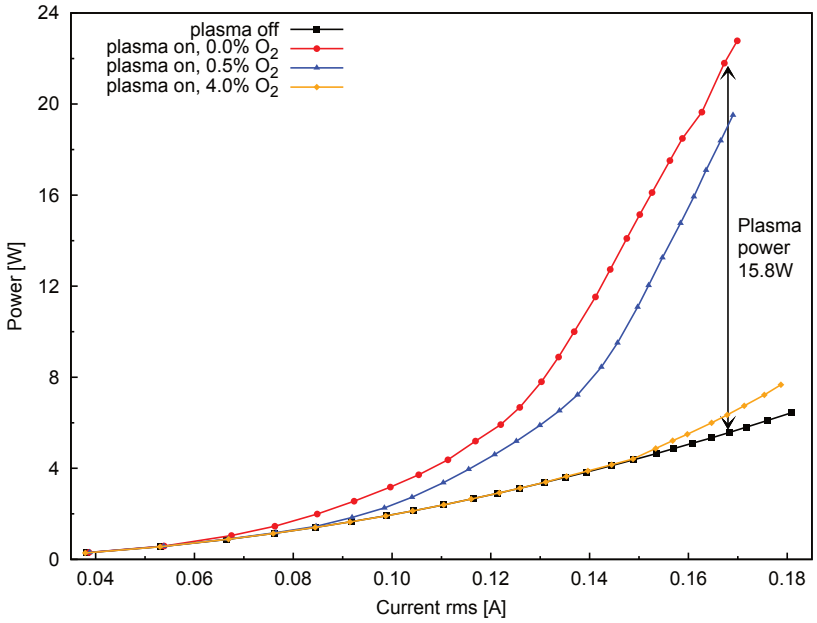

Figure 4.9: Power dissipated in the RF-PJ in function of the rms current flowing in the tungsten needle in plasma-off condition (black line), plasma-on condition with: 0.0% O_2 (red line), 0.5% O_2 (blue line) and 4.0% O_2 (orange line).

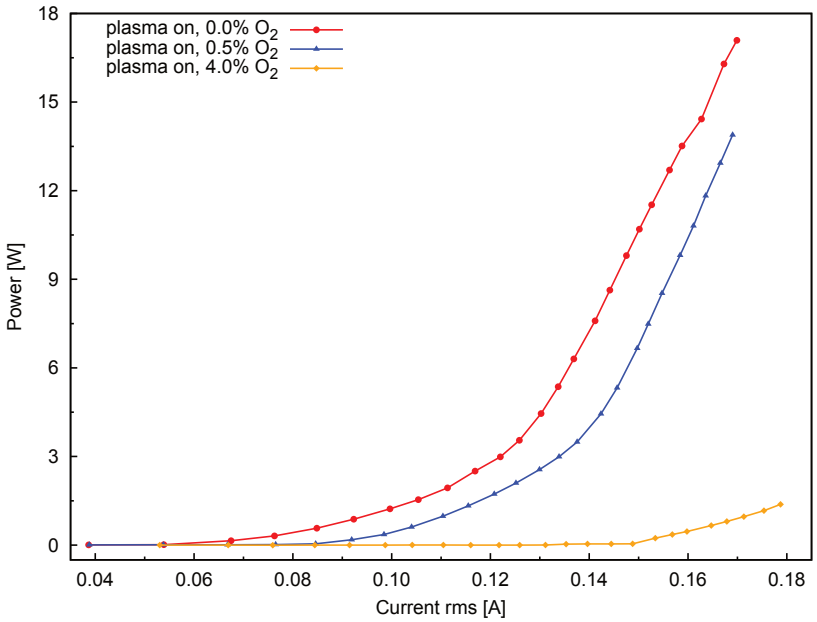

Figure 4.10: Power dissipated into the plasma with: 0.0% O_2 (red line), 0.5% O_2 (blue line) and 4.0% O_2 (orange line).

the content of oxygen, the power dissipated into the plasma decreases. This phenomenon is caused by a loss of electrons, due to attachment phenomena, and dissipation of electron energy, due to ro-vibrational excitation [11]. When we increase the content of molecular gas it is necessary to increase the voltage too in order to sustain the discharge keeping constant the current (moving from red to blue and orange line in Figure 4.11). In addition varying the O_2 content changes the voltage breakdown, see Figure 4.11. In pure He we observed the voltage breakdown at $V_B \approx 150\,\mathrm{V}$, $V_B \approx 225\,\mathrm{V}$ and $V_B \approx 350\,\mathrm{V}$ for 0.5% and 4.0% oxygen addition, respectively.

Figure 4.12 presents the real Z_R and imaginary Z_I part of the impedance as a function of the current. The reactive component is almost one order of magnitude larger than the resistive one. With the plasma switched on, the real component increases, while the reactive component decreases. Adding O_2, the resistive component decreases with respect to no-oxygen condition. This is further evidence that oxygen behaves has an electron acceptor. With the plasma switched off, the reactive component is more than one order of magnitude larger than the resistance. All these results are in agreement with those presented in [108, 109].

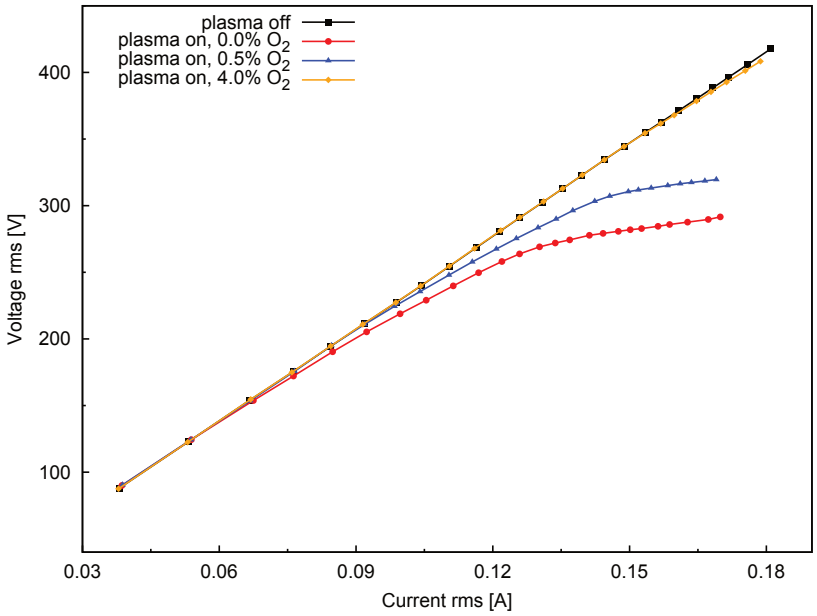

Figure 4.11: Rms voltage in function of the rms current flowing in the RF-PJ. Black line: plasma-off; red line: plasma-on, 0.0% O_2; blue line: plasma-on, 0.5% O_2; orange line: plasma-on 4.0% O_2.

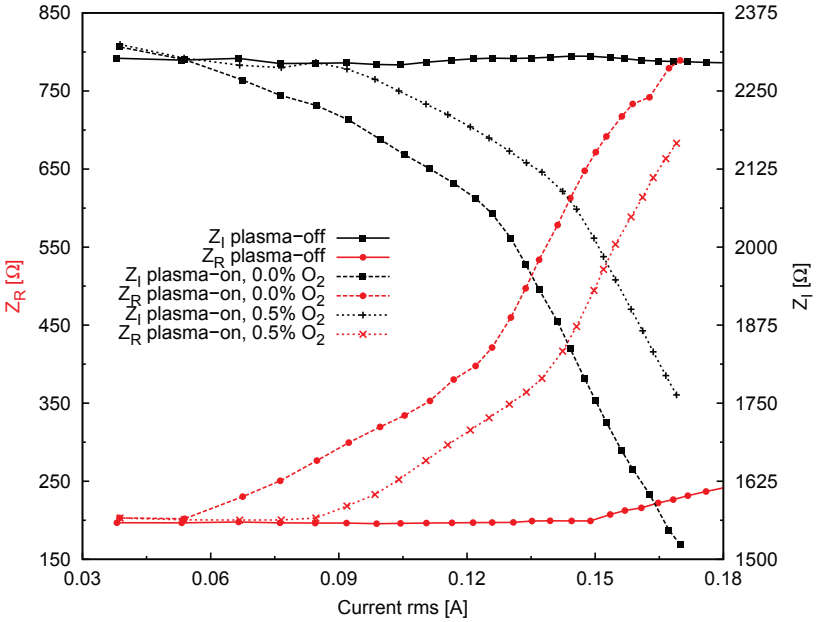

Figure 4.12: Real (Z_R) and imaginary (Z_I) part of the impedance (Z) as a function of rms current in the case of plasma-off and plasma-on with 0.0% and 0.5% O_2 addition.

Chapter 5

OH density measurements in He-H2O-O2 discharges

The importance of OH as an oxidation agent in many atmospheric pressure discharge applications, like plasma assisted combustion [110, 111, 112] and plasma medicine [113, 114, 115, 116, 13], is well known. Thus its local measurement in real operating conditions is highly desirable. OH concentration measurements in test cases are also of interest for comparison to model calculations [15].

We investigated the practical possibility of tailoring the OH production in two kinds of discharges widely used in technological, and in particular plasma medicine, applications. In the following, I present results of the application of TR-BBAS technique described in Chapter 2 to a $He-H_2O-O_2$ dielectric barrier discharge, aimed at investigating the effect of small oxygen additions to the OH concentration. The same $He-H_2O$ DBD (without O_2 additions) was used as calibration source for the LIF apparatus described in Chapter 3.5.1. In Section 5.2 I present the LIF measurements of OH generated in the plasma jet described in Chapter 3.3.5.

5.1 OH density measurements by time-resolved broad band absorption spectroscopy in a He-H_2O dielectric barrier discharge with small O_2 addition

We measured the OH density as a function of oxygen addition for various water vapour concentration values in the DBD discharge presented in Chapter 2.2.3.

The measurements are obtained by using the two detection setups already described in Chapter 2.2.2. Results are shown in Figure 5.1 and Figure 5.2 for detection setup D1[1] and D2[2], respectively.

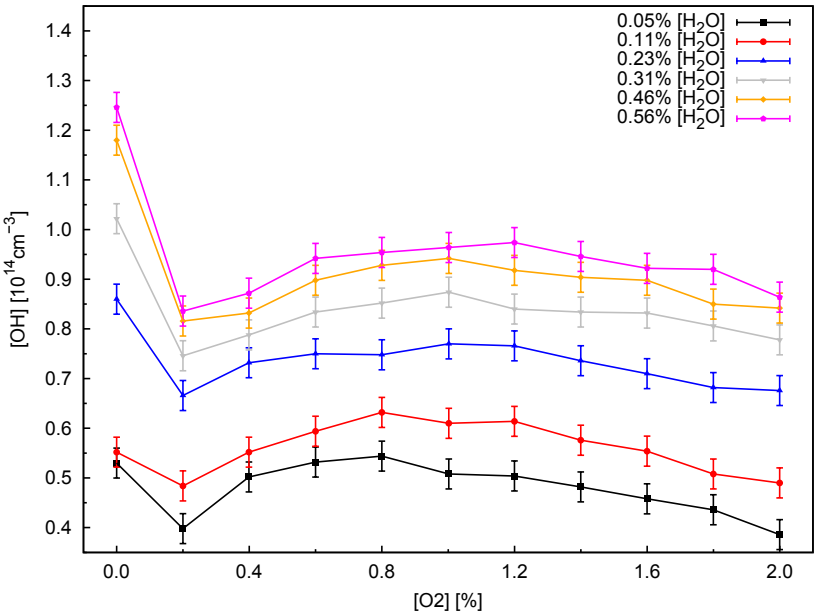

Figure 5.1: OH concentration as a function of O_2 percentage at various H_2O content, inter-electrodes gap 4.5 mm, applied voltage is 8.6 kV peak-to-peak, the gas temperature is constant and equal to 400 K, D1 detection setup. Error bars are the fit statistical error only.

[1] D1 is based on a 140 mm focal length monochromator (microHR, Jobin-Yvon) equipped with a 1200 gr mm^{-1} 300 nm blaze grating with a 100 µm input slit. The light detector is a charge coupled device (CCD) (GARRY 3000, Ames Photonics). This device is non-cooled, non-intensified, gateable 3000 elements linear CCD array.

[2] D2 is composed of a 300 mm focal length monochromator (Shamrock 303i, Andor) equipped with a 1200 gr mm^{-1} 300 nm blaze grating, 70 µm input slit. The detector coupled to the Shamrock 303i is a cooled, 1024 × 1024 pixel, intensified CCD (ICCD) (DH334T-18U-03, Andor).

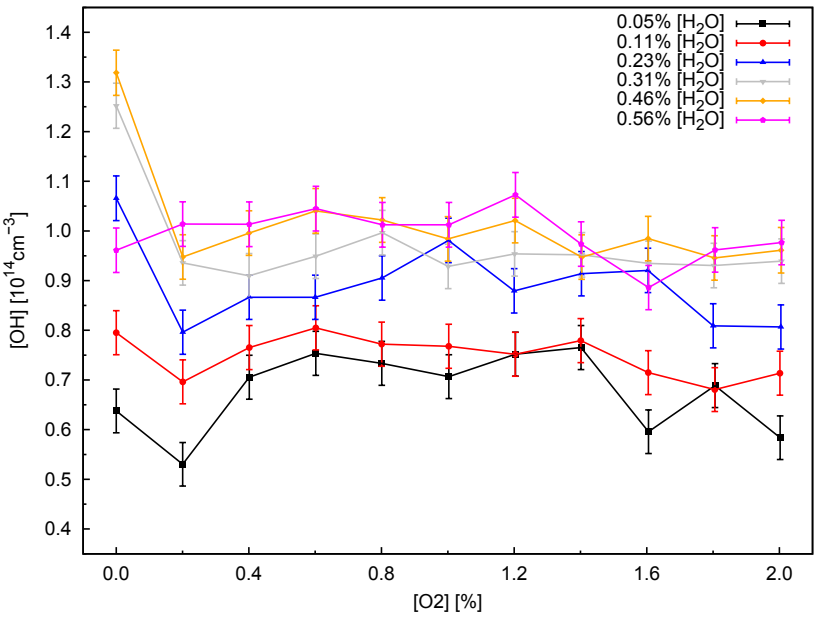

Figure 5.2: Same condition of Figure 5.1. Detection scheme is D2. Error bars are the fit statistical error only.

The results shown in the two previous figures are compatible within the experimental error. As expected, the errors associated to the fits of detection setup D2 are larger than those of detection setup D1, and the plot appears noisier. This is due to the fact that in detection setup D2 the effective CCD gate is decreased from the $300\,\mu s$ (of D1) to $140\,\mu s$ at the expense of the signal to noise ratio.

The discharge power density is reported as a function of water and oxygen addition in Figure 5.3. Figure 5.4 shows a comparison between two Lissajous figures obtained at different oxygen concentration. Oxygen addition causes a decrease of the charge accumulated in the dielectrics, i.e. the current decreases and the resistive component of the impedance increases. Power variation remains within about 10% along the gas composition range examined. The largest variation is at low water content, while with more water added the power does not change much with the gas composition. The power density is then $8.1 - 9\,W\,cm^{-3}$.

We investigated the dependence of the OH concentration as a function of the discharge power density. Figure 5.5 shows the [OH] vs power plots for the $4.5\,mm$ and $2.0\,mm$.

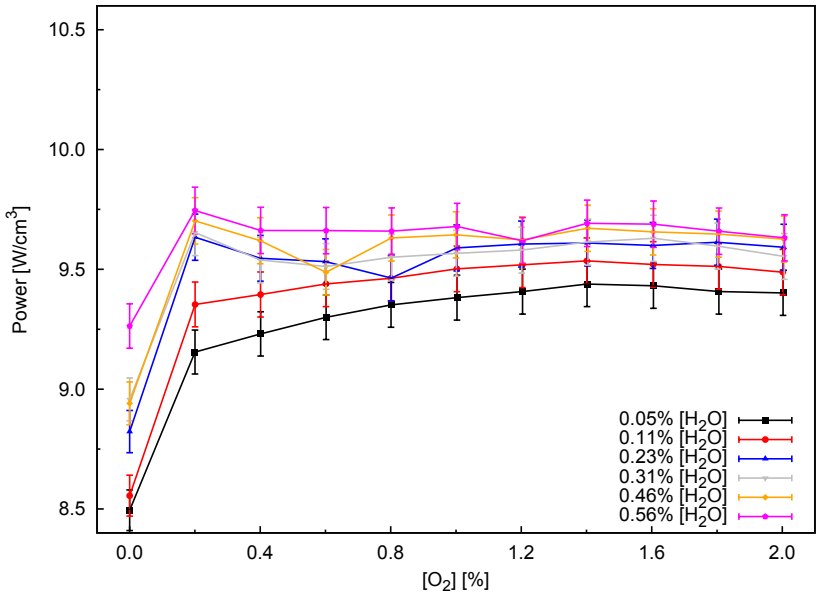

Figure 5.3: Power density as a function of the addition of O_2 and H_2O at the same condition of Figure 5.1 and Figure 5.2.

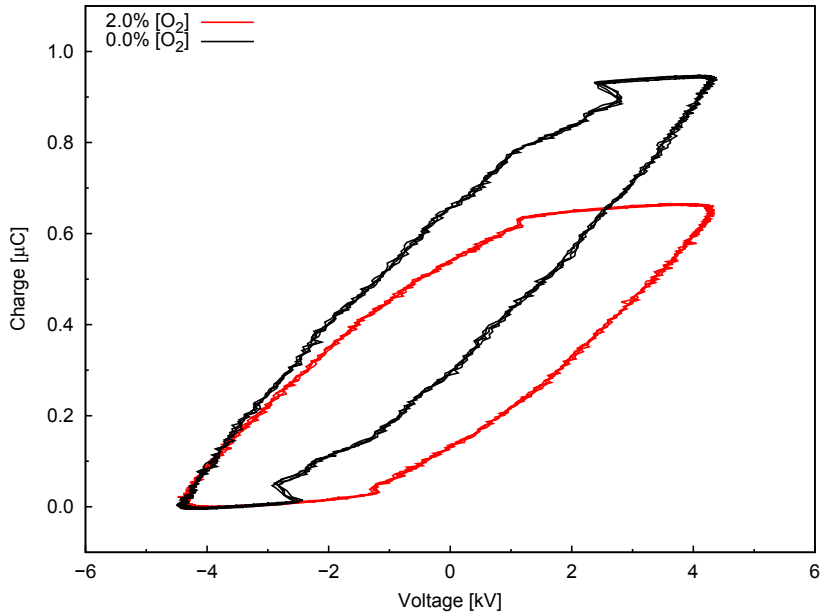

Figure 5.4: Lissajous figures for 0.0% and 2.0% oxygen concentration. H_2O content is 0.05%, discharge gap is 4.5 mm, applied voltage is 8.6 kV peak-to-peak.

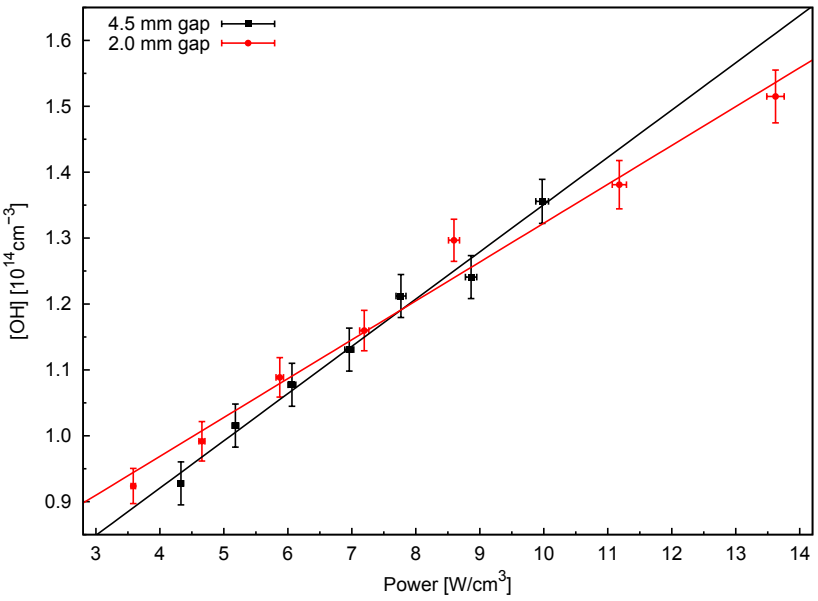

Figure 5.5: OH concentration as a function of power density at [H_2O]$= 0.56\%$, gaps of 4.5 and 2 mm, detection scheme D2. OH concentration error bars are the fit statistical error only.

We also measured the OH density in the same discharge but with a smaller inter-electrodes gap of 2 mm. Figure 5.6 shows the concentration of OH as a function of the oxygen and water concentrations. The power as a function of gas composition, is presented in Figure 5.7. In general we observe an increase of the OH density.

A detailed comparison between our results and those reported in literature can be found in our paper [23].

5.1.1 Discharge morphology

The discharge appears to be a diffuse one. As shown in Figure 5.8, with no oxygen added the current is quasi-periodic and micro-discharge peaks are not observed. Such a structure is conserved when oxygen is present (Figure 5.9, and Figure 5.10).

In the case of the 2 mm gap, some difference are observed with respect the 4.5 mm case. A large number of well defined current peaks appears in Figure 5.11. Adding only water to the discharge does not cause the appearance of this ordered structures (Figure 5.12). The influence of water addition on the discharge structure in presence of oxygen is shown in

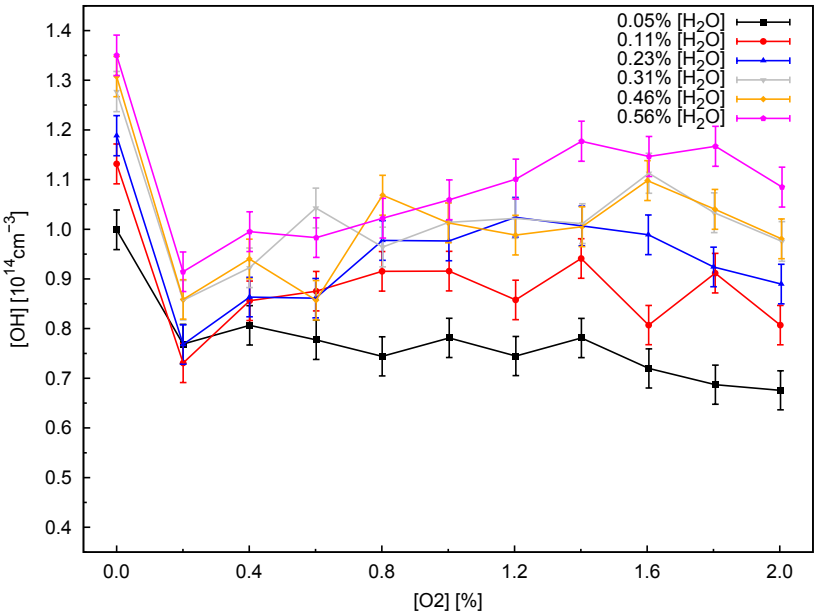

Figure 5.6: OH concentration as a function of O_2 percentage at various H_2O content; inter-electrodes gap is 2.0 mm; applied voltage is 6.8 kV peak-to-peak; the gas temperature is constant and equal to 380 K; D2 detection setup is used. Error bars are the fit statistical error only.

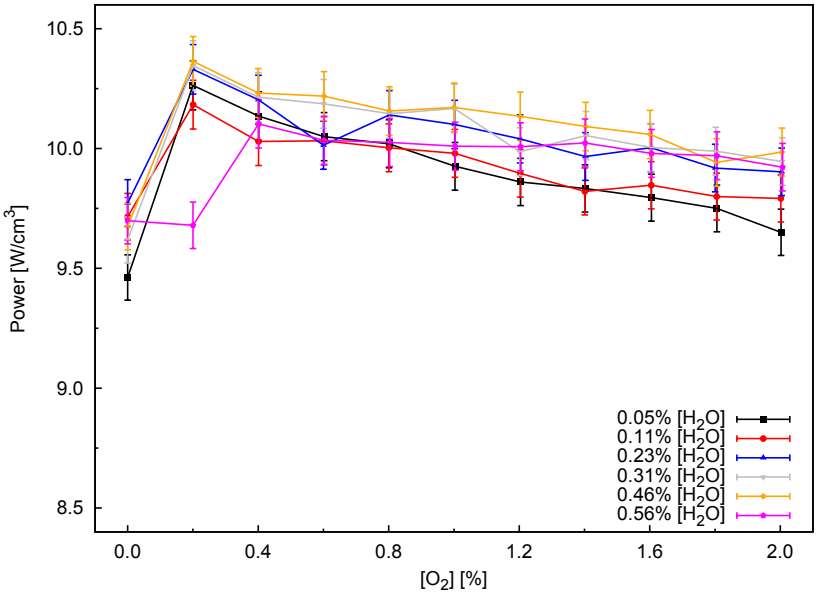

Figure 5.7: Power density as a function of the addition of O_2 and H_2O at the same condition of Figure 5.6.

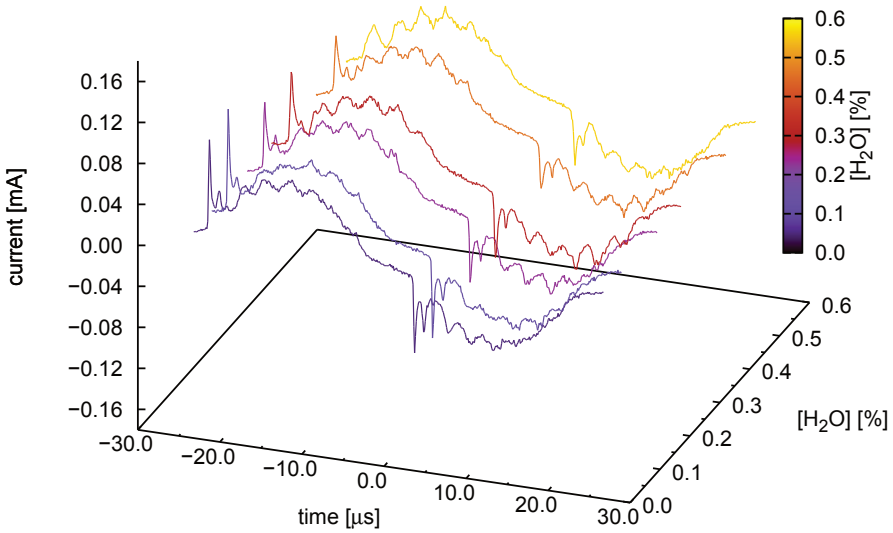

Figure 5.8: Single-period current traces for the 4.5 mm inter-electrodes gap; applied voltage is 8.6 kV peak-to-peak; [O_2]= 0.0%. The difference between various H_2O additions is shown.

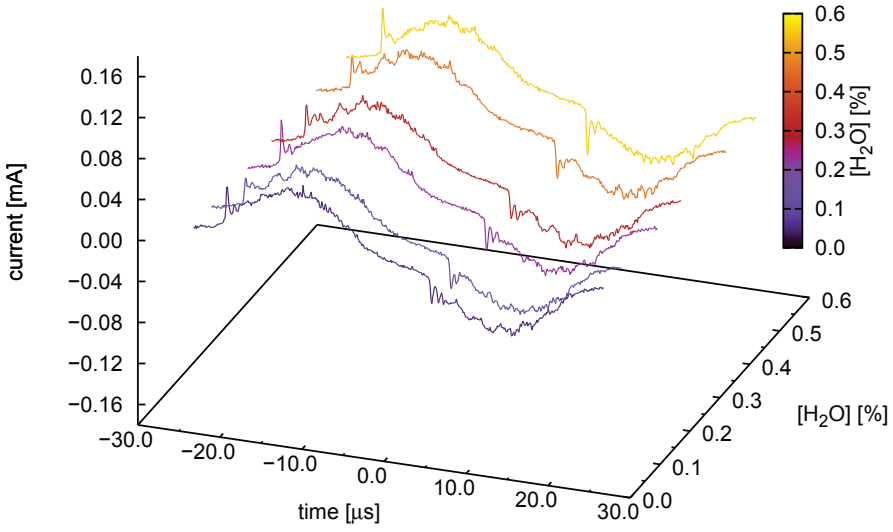

Figure 5.9: Single-period current traces for the 4.5 mm inter-electrodes gap; applied voltage is 8.6 kV peak-to-peak; [O_2]= 2.0%. The difference between various H_2O additions is shown.

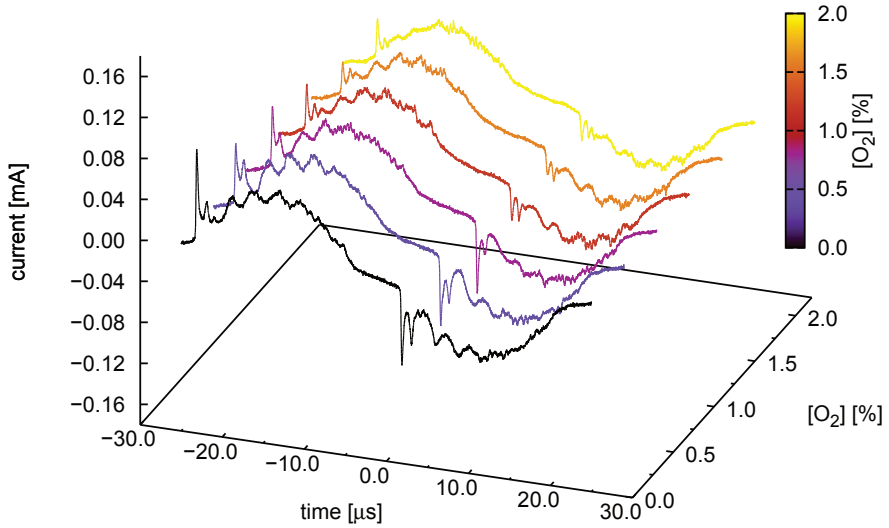

Figure 5.10: Single-period current traces for the 4.5 mm inter-electrodes gap; applied voltage is 8.6 kV peak-to-peak; [H_2O]$= 0.05\%$. The difference between various O_2 additions is shown.

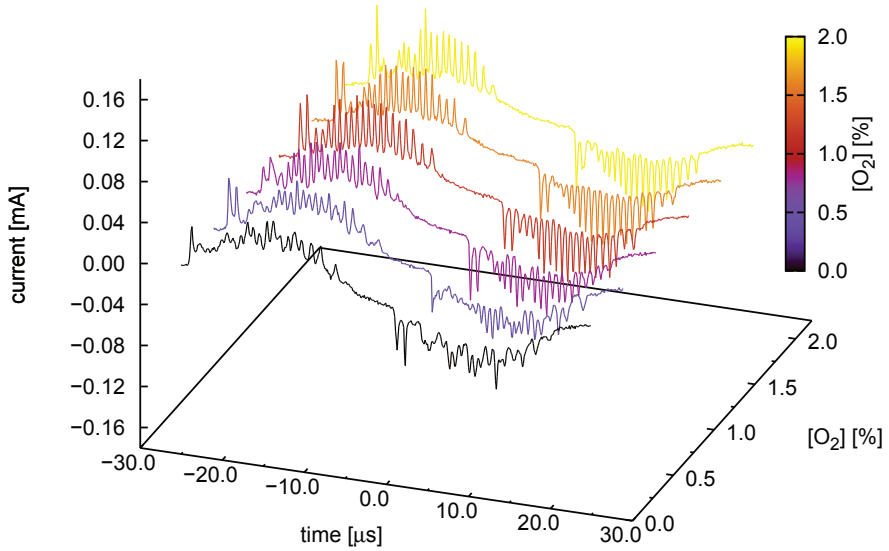

Figure 5.11: Single-period current traces for the 2.0 mm inter-electrodes gap; applied voltage is 6.8 kV peak-to-peak; [H_2O]$= 0.05\%$. The difference between various O_2 additions is shown.

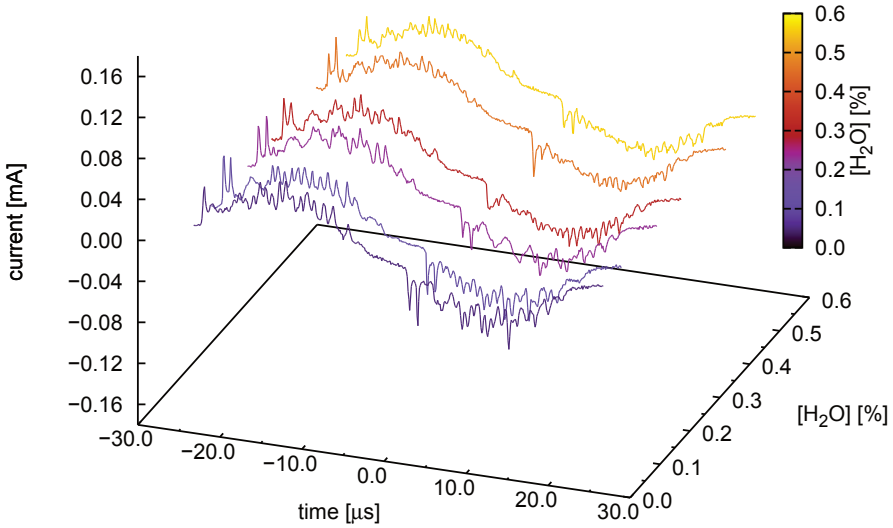

Figure 5.12: Single-period current traces for the 2.0 mm inter-electrodes gap; applied voltage is 6.8 kV peak-to-peak; $[O_2]= 0.0\%$. The difference between various H_2O additions is shown.

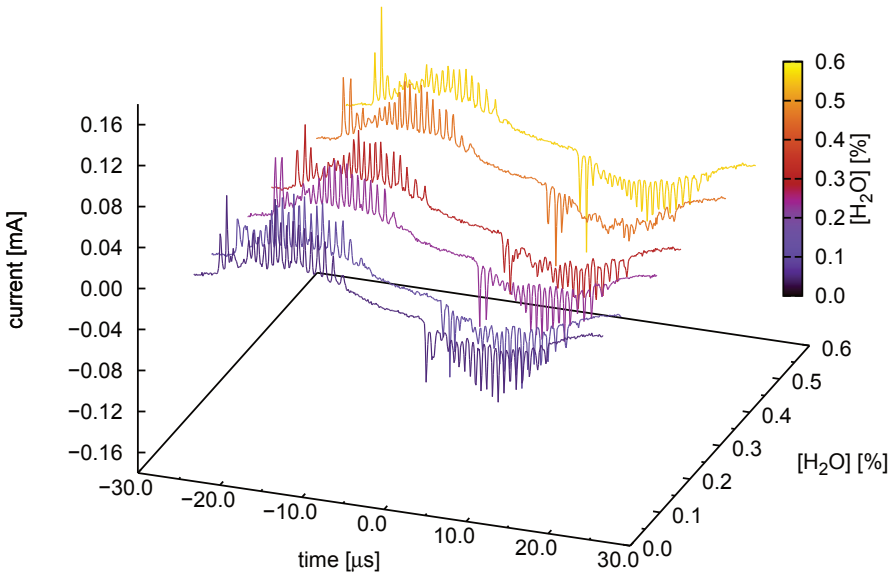

Figure 5.13: Single-period current traces for the 2.0 mm inter-electrodes gap; applied voltage is 6.8 kV peak-to-peak; $[O_2]= 2.0\%$. The difference between various H_2O additions is shown.

Figure 5.13, where we observe a slight decrease of the current peaks intensity increasing the water content. The appearance of ordered structures in the current versus time plot does not indicates a transition to a filamentary regime, but rather a morphological change of the discharge that is not distinguishable by the naked eye. The current peaks have in fact a long duration of the order of many hundreds of ns, and the current pattern is quasi-periodic.

Temperature measurements were also carried out. The OH ground-state temperature was estimated by fit of the BBAS spectra. We obtained (400 ± 20) K for 4.5 mm gap, (380 ± 20) K for 2 mm gap, and independently of the gas composition. The lower temperature for the 2 mm gap can be explained to the faster gas flow and the reduced discharge volume, which in turn permits an higher heat dissipation.

5.2 OH density measurements by Laser Induced Fluorescence spectroscopy in a He-H_2O Radio Frequency Plasma Jet

Atmospheric-pressure plasma jets are a source of non-thermal plasma of emerging interest. The possibility to generate ROS, such as OH and O radicals, makes PJ attractive for biomedical applications [117]. We used LIF to measure OH concentration in a RF plasma jet of He$-H_2O$. The jet plume impinges over the surface of a liquid target, composed by 100 µl of a commercial mixture of oilseeds. A flux of 1600 sccm of He is mixed with a second 400 sccm flow of He coming from a bubbler filled with distilled water. Further 2000 sccm of He are used as a co-flow in order to shield the plume from the surrounding air. The plasma power is 2.7 W.

OH concentration along a plane cutting the plasma plume in the centre is presented in Figure 5.14. In Figure 5.15, 5.16 are reported the air and water partial pressure, respectively. Figure 5.17 shows the OH ground state rotational temperature map. Ground state rotational temperature was estimated by using the group of lines $Q_{12}(1)$, $Q_2(1)$, $Q_1(6)$, $Q_{12}(3)$ and $Q_2(3)$. OH density, air and water partial pressure were calculated using the $Q_2(3)$ line, as described in Chapter 3. The OH map shows quite clearly a deviation towards the right side of the flow, which was also visible with the naked eye. From the air map, it appears that this deviation is due to an asymmetry of the co-flow that allows air to penetrate from the left

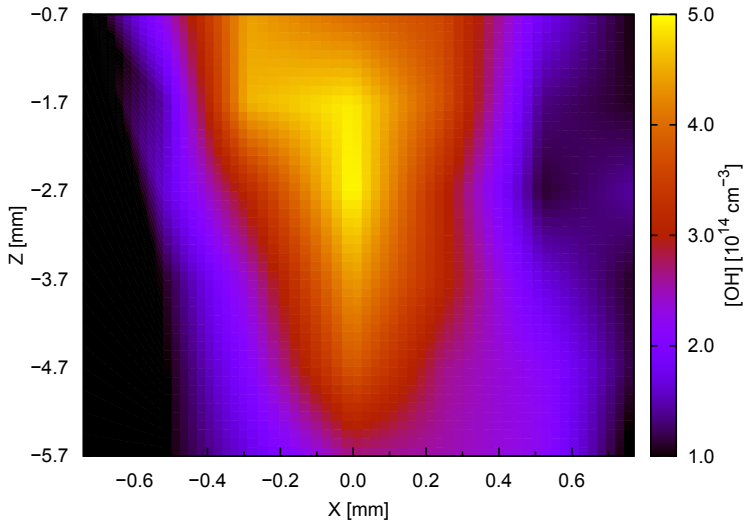

Figure 5.14: Map of OH in the effluent jet impinging on an oilseed target. Z is the distance from the jet edge. The target is at -6.2 mm from the edge. The maps are made of 42 interpolated experimental points. The effluent flux is a 2000 sccm He+0.45% H_2O mixture, with a 2000 sccm of He co-flow. RF power is 2.7 W.

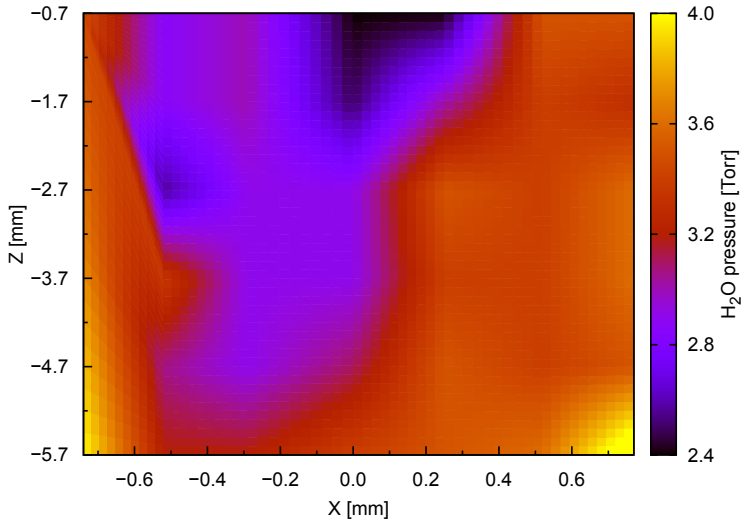

Figure 5.15: Map of air concentration in the effluent jet in the same condition of Figure 5.14.

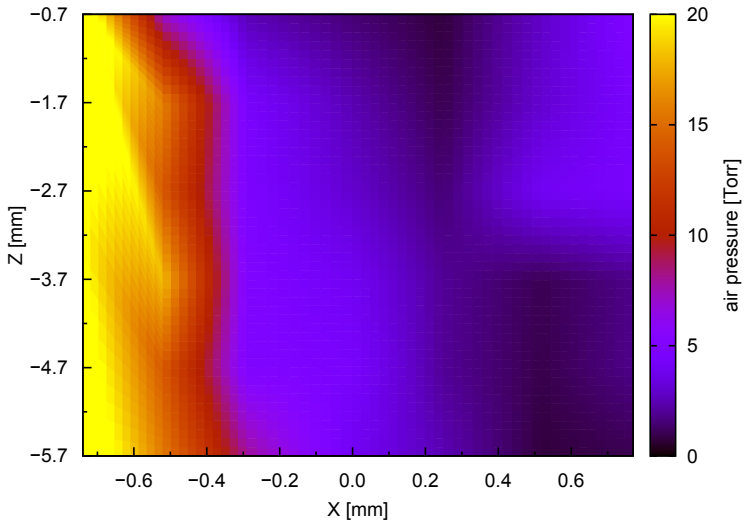

Figure 5.16: Map of H_2O concentration in the effluent jet in the same condition of Figure 5.14.

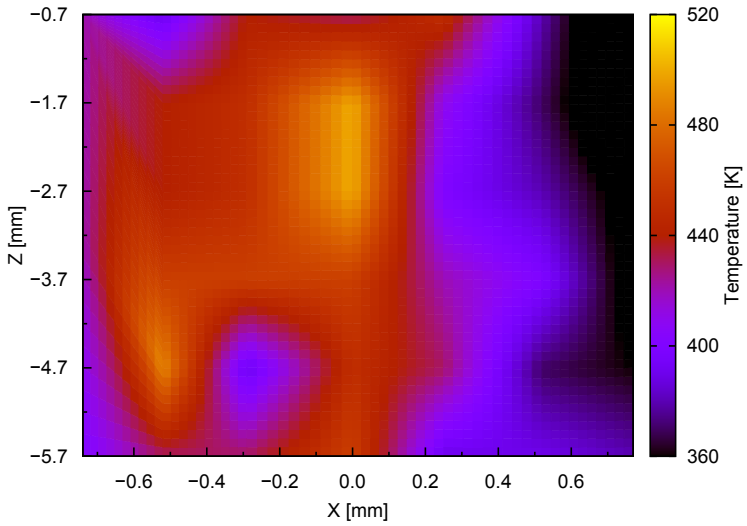

Figure 5.17: Map of the OH ground state rotational temperature in the effluent jet in the same condition of Figure 5.14.

side. Such an air penetration into the left side of the discharge region could be the reason for the temperature increase in the same side. Measurements demonstrate that temperatures are higher for molecular gases, such as air, compared with those of rare gases [118]. The water partial pressure is smaller in the plume, due to the increasing dissociation rate inside the plasma. We finally observe that the spatial resolution is of the order of 0.2 mm.

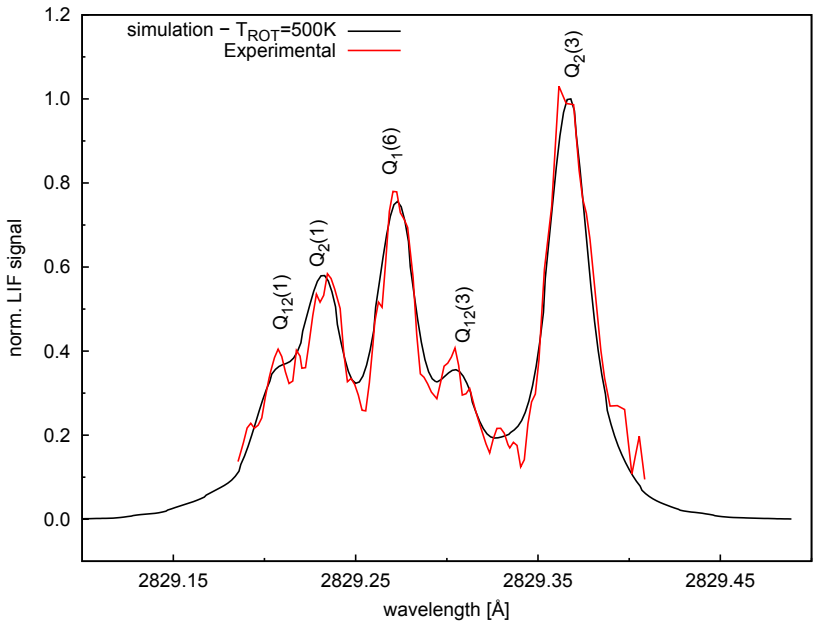

Figure 5.18: LIF excitation spectrum and model simulation for the measurement of the OH ground state rotational temperature. The excitation spectrum is recorded at recorded at $X = 0.0$ mm, $Z = -2.7$ mm. Simulated spectra is calculated at $T = 500$ K. The estimated OH density is 5.04×10^{14} cm^{-3}. Water and air partial pressure are 2.9 torr and 3.0 torr, respectively.

Figure 5.18 shows an experimental excitation spectrum. The measure was performed at $X = 0.0$ mm and $Z = -2.7$ mm, where the [OH] density reaches the maximum value of 5.04×10^{14} cm^{-3}. The best fitting ground state rotational temperature is 500 K.

The maximum OH density measured 0.5 mm above the target (i.e. the oil surface) is 1.23×10^{14} cm^{-3}. It was not possible to measure the OH concentration closer to the oil surface because of the wall of the vessel that contains the liquid target. We also estimate the minimum amount of OH produced without injecting He in the bubbler in the same condition of total flux (2000 sccm in the carrier gas and 2000 sccm in the co-flow) and power (around $2.7 - 2.9$ W). The maximum content of OH on the target surface was 5.0×10^{13} cm^{-3}, that

is only five times smaller than the value obtained with the H_2O added into the gas carrier. This large value of OH concentration is probably due to the presence of residual water in the pipe lines, despite the various experimental cautions taken.

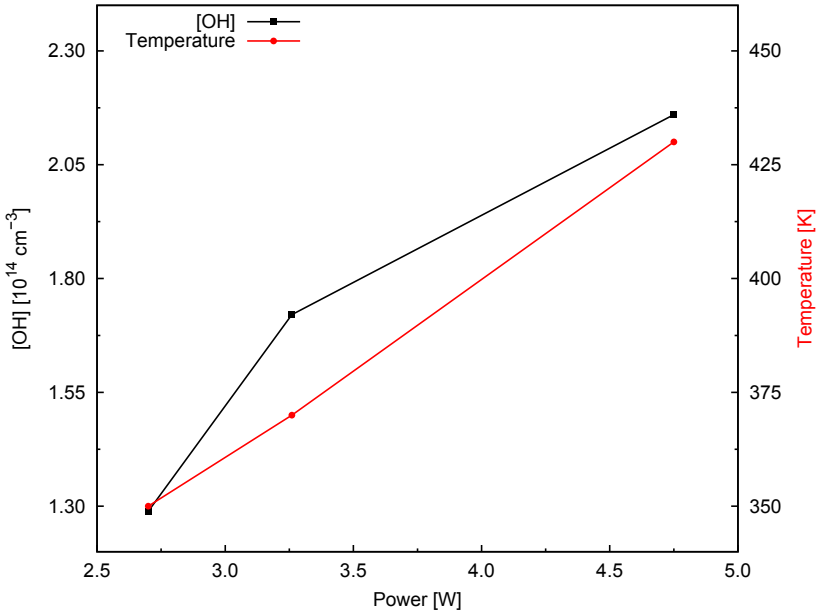

Figure 5.19: OH concentration (left) and ground state rotational temperature (right) as a function of the power dissipated in the plasma. The target is at -6.2 mm from the tungsten needle. The effluent flux is a 2000 sccm He$+0.45\%$ H_2O mixture, with a 2000 sccm of He co-flow. Air and H_2O concentrations are 1.6 torr and 3.6 torr, respectively. OH density uncertainty is 20%. Ground state rotational temperature uncertainty is ± 10 K.

Figure 5.19 show the OH concentration and rotational temperature as a function of power. Increasing the dissipated power into the discharge correspond to an increase of the OH production and ground state rotational temperature.

Chapter 6

Conclusions

The experimental and modelling advancements achieved in the present work reduce the noxious effects of the spontaneous emission on the optical detection of transient species, in non-thermal plasmas, by either TR-BBAS or LIF. For the specific case of LIF, we introduced a novel excitation scheme based on several rotational transitions. This allows us to measure, at the same time, the density and the rotational temperature of OH in the ground state.

We developed a new model for interpreting LIF outcomes in non linear regimes. This is particularly useful when measuring radical concentrations in small and highly inhomogeneous targets, with high-spatial resolution. This requires focusing the laser beam on a minimum spot, and in turn this may lead to a non linear regime of the excitation. We used OH as a benchmark for our model, which appears to be robust and predictive of the LIF outcome also in the condition of weak saturation. Our improved technique allows us to perform accurate LIF measurements also on small and inhomogeneous discharges, as micro-plasma jets that are widely used nowadays. The improved interpretation of LIF outcomes, which we tested in the case of OH, can be reasonably extended to other radicals, as H and CH.

Appendix A

Detailed description of the devices

A.1 Optical variable attenuator

A key requirement in LIF experiments is the ability to change the laser power over a wide dynamic range without significant alteration of the beam profile, position and direction. For this purpose various devices can be utilised. A first example is given by attenuators based on rotating $\lambda/2$ wave plates coupled with a polarising cube. These devices have a wide dynamic range and produce a minimum beam deviations. Other devices are simply based on rotating polarising cubes, but then the beam deviation becomes important. These attenuators aren't suitable for broad-band applications and their dynamics range is in the order of $20 - 25\,\mathrm{dB}$. Our aim was to build a variable attenuator with a higher dynamic range, and broad-band operation capabilities. We chose to build a device based on Fresnel reflection, like the one describe by Bennett *et al* [61], who reported the construction of a broad-band attenuator, with a dynamic range of $30 - 35\,\mathrm{dB}$, and a damage threshold $> 3\,\mathrm{J\,cm^{-2}}$.

A.1.1 Theoretical background

The attenuator is composed of two counter-rotating couples of beam-splitters, as shown Figure A.1. For a single surface, the power transmission depends on polarization, refraction

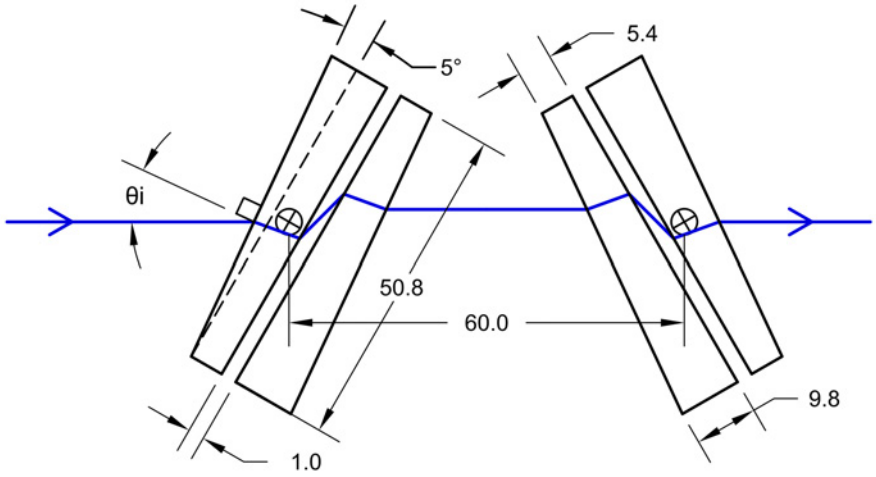

Figure A.1: Schematic representation of the attenuator optical layout. Two couples of uncoated UV fused silica beam-splitters (BSF2550, Thorlabs) counterrotate around their rotation axis $\oplus$. The incoming laser beam hit the first wedge plate (on the left side of the figure) and it is propagated from one to the other. The laser beam losses energy upon each reflection and refraction. The angle of incidence θ_i is defined as the angle respect of the normal of the first surface encountered by the laser beam (that is $\alpha = 5^\circ$ larger than the rotation angle of the attenuator plates θ_w that is defined as the angle respect to the condition in which the wedge plates surfaces of the inner gaps of the two couple are parallel).

indexes of the incident n_i and transmitting media n_t, and the angle of incidence θ_i:

$$T_{S\perp}(\theta_i, n) = \frac{sin(2\theta_i)\, sin(2\theta_t)}{sin^2(\theta_i + \theta_t)},$$

$$T_{S\parallel}(\theta_i, n) = \frac{T_{S\perp}(\theta_i, n)}{cos^2(\theta_i - \theta_t)},$$

$$n = \frac{n_t}{n_i},$$

$$n\, sin(\theta_t) = sin(\theta_i).$$

Wedge plates, with wedge angle $\alpha = 5°$, allow total internal reflection to be achieved. The total transmittance T of the device is the fourth power of the transmittance of a single wedge plate T_w:

$$T(\theta_i, n, \alpha) = [T_w(\theta_i, n, \alpha)]^4 = [T_S(\theta_i, n)\, T_S(\theta_t + \alpha, 1/n)]^4.$$

A.1.2 Design and testing

Figure A.1 shows a schematic of the wedge-plate attenuator. Two couples of identical plates (50.8×25.4 mm, 5.4 mm thick, $\alpha = 5°$ wedge angle) counter-rotate at a distance of 60 mm. The beam acceptance aperture is set to $a = 3$ mm. As reported in [61], we calculated the fractional beam expansion, in the plain of incidence, $\Delta a/a$ as:

$$\frac{\Delta a}{a} \approx 2\frac{cos^2(\theta_i)}{cos^3(\theta_{t_2})}\Delta\theta_i.$$

For a 281 nm laser beam, with a maximum attenuation of 25 dB, the beam expansion is $\Delta a/a < 350\Delta\theta_i$. We verify that the wedge overlap (in our case $D = L = 50.8$ mm), is sufficient to avoid beam clipping by the second wedge. As shown in Figure A.2, the propagation direction of the beam passes through the centre of the counter-rotating plates. When the beam intercepts the wedge with an angle θ_i, the projection on the gap plane of the distance between the centre of the window and the incidence point:

$$A(\theta_i) \approx \frac{k}{2} atan(\theta_w) = \frac{k}{2} atan(\theta_i + \alpha),$$

where $k = 7.6$ mm is the windows thickness in the centre. We define Δk as the difference between the two short axes of the wedge, $\Delta k = 9.8 - 5.4 = 4.4$ mm. The thickness of the

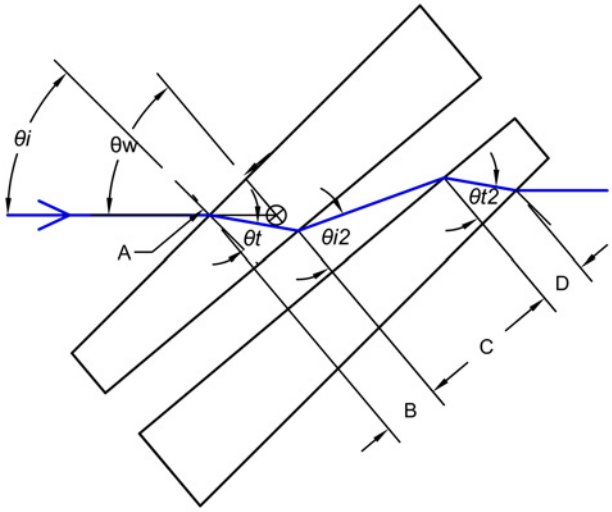

Figure A.2: Detail of the beam-splitter. A,B,C and D indicate the projections of the laser beam on the internal surface of a the wedge plate.

windows in the point where the laser intercepts the first and the second window are T_{eff1} and T_{eff2}, respectively:

$$T_{eff1} = k - \frac{\Delta k}{2}\left(\frac{2A\left(\theta_i\right)}{L}\right),$$
$$T_{eff2} = k - \frac{\Delta k}{2}\left(\frac{2\left(B\left(\theta_t\right) + C\left(\theta_{i2}\right) - A\left(\theta_i\right)\right)}{L}\right).$$

The components of the beam path parallel to the internal surface (see Figure A.2) are:

$$B\left(\theta_t\right) \approx T_{eff1}\, tan\left(\theta_t\right),$$
$$C\left(\theta_{i2}\right) = S\, tan\left(\theta_{i2}\right),$$
$$D\left(\theta_{t2}\right) \approx T_{eff2}\, tan\left(\theta_{t2}\right).$$

The angles θ_t, θ_{i2} and θ_{t2} can be written in function of θ_i using the Snell-Law.

$$n\, sin\left(\theta_t\right) = sin\left(\theta_i\right),$$
$$sin\left(\theta_{i2}\right) = n\, sin\left(\theta_t + \alpha\right),$$
$$n\, sin\left(\theta_{t2}\right) = sin\left(\theta_{i2}\right).$$

The clipping of the beam occurs when:

$$\frac{L-a}{2} \leqslant -A\left(\theta_i\right) + B\left(\theta_i\right) + C\left(\theta_i\right) + D\left(\theta_i\right).$$

We expect a maximum attenuation of 31.2 dB at $\theta_i = 63.8°$.

A.1.3 Test

In order to verify the attenuator performances, we built a test setup as shown in Figure A.3. We used a He-Ne laser source with a beam waist of 0.4 mm, and a divergence of

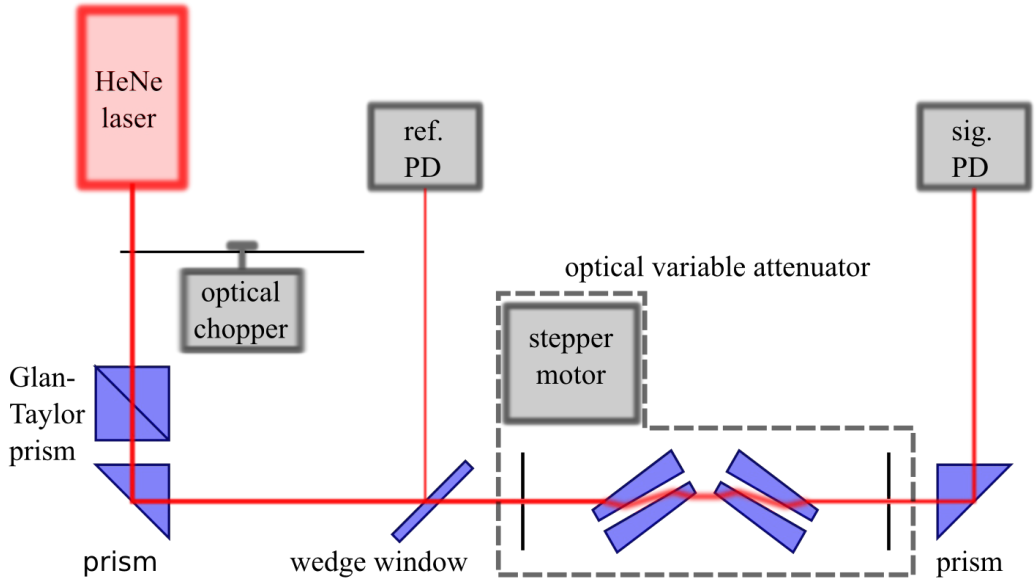

Figure A.3: Schematic representation of the attenuator test setup. ref. PD: He-Ne laser reference photodiode; sig. PD: signal photodiode.

1 mrad. Reference and attenuated beams were measured using two unbiased silicon photodetector (OSD5-5T, Centronic) coupled with a transimpedance amplifier ($G = 10^4$ V A^{-1}). An optical chopper modulates the laser beam for lock-in detection. A Glan-Taylor polarising prism was placed before the reference beam splitter in order to obtain a vertical polarised laser beam. The counter-rotating plates were moved by a stepper motor. Lock-in outputs were sampled using a USB DAQ module (NI-USB 6212, National Instruments), which also generates digital signals for driving the stepper motor.

The laser attenuation as a function of the increment from the critical angle is reported in Figure A.4. The plane of incidence of the attenuator was chosen perpendicular to the polarisation of the incoming laser beam. Experimental points appear in agreement with the calculated ones. For the 632.8 nm-beam the insertion loss is 1.8 dB, and the maximum

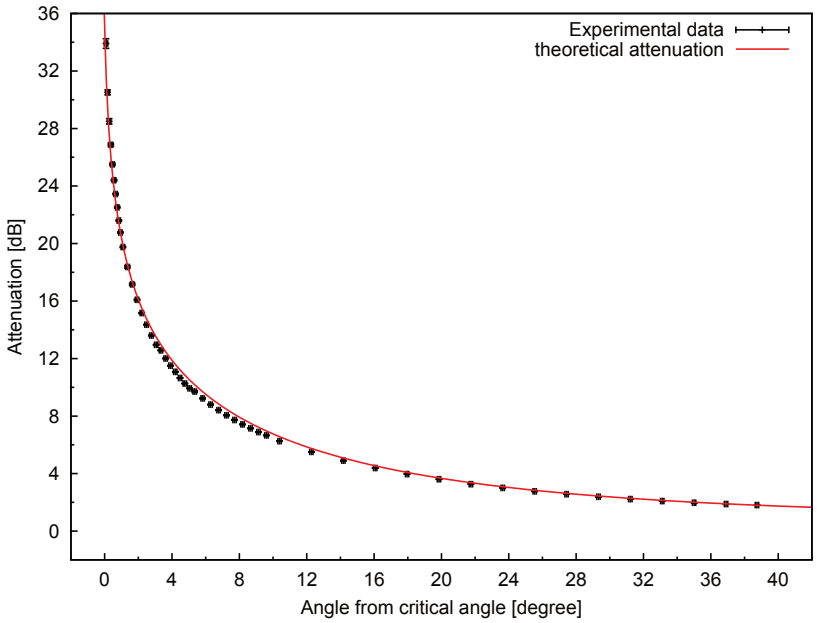

Figure A.4: Attenuation as a function of the angle from the critical angle for a 632.8 nm-beam with polarisation perpendicular to the plane of incidence

attenuation is about 34 dB.

A.2 Laser energy detectors

Knowing the energy of the laser beam is crucial for LIF measurements, in particular its time evolution. In order to measure with the maximum accuracy the laser shot energy, we developed two distinct power detectors.

A.2.1 Low-energy pulse detector

The first detector is based on a single-channel silicon-based thermopile (DX-0576, Dexter research center) and it is used for energy $E < 4\,\mu\text{J pulse}^{-1}$. The detector has an active area of $2.25\,\text{mm}^2$, a typical responsivity $\Re = 31\,\text{V W}^{-1}$, an equivalent series resistance $R_s = 90\ k\Omega$, and a time constant $\tau_s = 38\,\text{ms}$. Due to the large time constant of the thermopile, it is impossible to record the measured energy profile using an oscilloscope simultaneously with the fluorescence signal. Indeed the power measure is carried out using a digital multimeter that records the peak voltage after $t_{sample} = 150\,\mu\text{s}$ from the laser shot,

when the detector signal is at the maximum. In order to increase the sensor signal we used a non-inverting amplifier with gain $G = 500$. The amplifier design is based on 250 MHz rail-to-rail CMOS operational amplifier (OPA357, Texas Instruments). A graphical repres-

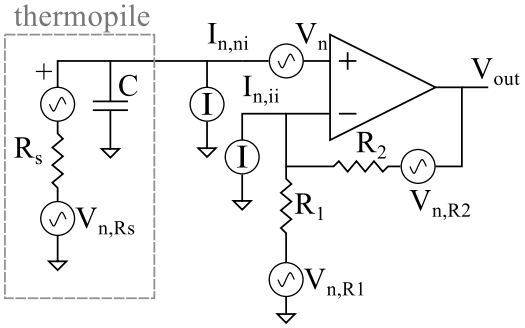

Figure A.5: Schematic representation of the single-channel silicon-based thermopile detector and its non inverting amplifier with gain $G = 500$. $R_s = 90\ k\Omega$, $R_1 = 100\ \Omega$, $R_2 = 51.1\ k\Omega$. C is the detector element capacitance.

entation of the amplifier circuit is presented in Figure A.5. The amplifier design is finalised at minimising the noise figure (NF) of the device in order to maximise the signal to noise ratio SNR_o. The large thermopile series resistance impose us to choose an opamp characterised by a low input bias current $I_{bias} = 3\,\text{pA}$ and a low input noise $V_n = 6.5\,\text{nV Hz}^{-1/2}$. The noise figure of the device (expressed in dB) is defined as:

$$NF = 10\ log\left(\frac{SNR_I}{SNR_O}\right) = 10\ log\left(1 + \frac{N_A}{N_I}\right),$$

where N_I is the noise delivered from the thermopile to the input of the amplifier and N_A is the input noise of the operational amplifier. The input-referred noise is easy to find, in fact is essentially the noise voltage generated by the thermopile source resistance:

$$N_I = 4kTR_s.$$

The amplifier's voltage noise is a function of the current $I_{n,ni} = I_{n,ii} = I_n = 50\,\text{fA Hz}^{-1/2}$ and voltage noise $V_n = 6.5\,\text{nV Hz}^{-1/2}$ of the opamp, and the thermal noise of the resistors:

$$N_A = c_1V_n^2 + c_2I_{n,ni}^2 + c_3I_{n,ii}^2 + c_4V_{n,R_1}^2 + c_5V_{n,R_2}^2.$$

c_1 to c_5 are scaling factors, $c_1 = 1$ for the opamp's input noise, $c_2 = R_S^2$ because the non-inverting input noise develops a voltage across the thermopile series resistor. The inverting

input current noise develops a voltage drop across the parallel of R_1 and R_2:

$$c_3 = \left(\frac{R_1 R_2}{R_1 + R_2}\right)^2 \approx R_1^2,$$

because $R_1 \ll R_2$. The noise terms associated to R_1 and R_2 are:

$$c_4 V_{n,R_1}^2 = 4kTR_1 \left(\frac{R_2}{R_1 + R_2}\right)^2,$$
$$c_5 V_{n,R_2}^2 = 4kTR_2 \left(\frac{R_1}{R_1 + R_2}\right)^2.$$

The resulting noise figure is $NF = 0.18$ ($N_I = 39\,\mathrm{nV\,Hz^{-1/2}}$, $N_A = 8\,\mathrm{nV\,Hz^{-1/2}}$ and $N_O = 892\,\mathrm{nV\,Hz^{-1/2}}$). The amplifier output noise expressed in terms of energy is $N_O = 2.9\,\mathrm{pJ\,Hz^{-1/2}}$.

A.2.2 High-energy pulse detector

The second energy detector is based on a pyroelectric element (P1-13, Molectron). The schematic representation is presented in Figure A.6. The incoming UV-beam is focalised on the active surface of the detector that in turn generates a current. As a consequence a voltage drop is generated on the parallel between $R_1 = 250\ \Omega$ and $R_2 = 200\ \Omega$. The voltage signal is then buffered by a AD8021 (Analog Devices) and amplified by a factor of 10. The noise voltage delivered to the amplifier input from the source resistance of the

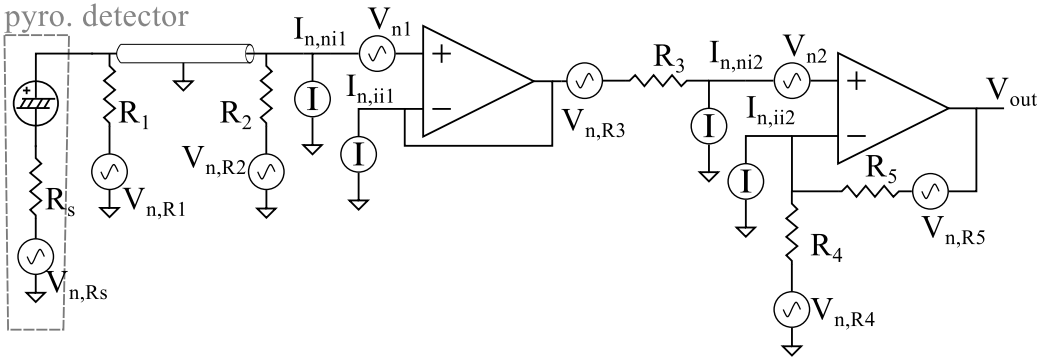

Figure A.6: Schematic representation of the pyroelectric-based energy detector and its amplifier with gain $G = 10$. $R_s = 10\ G\Omega$, $R_1 = 250\ \Omega$, $R_2 = 200\ \Omega$, $R_3 = 159\ \Omega$, $R_4 = 99\ \Omega$ and $R_5 = 899\ \Omega$.

pyroelectric detector is $\sqrt{4kTR_s}$ and it is divided by the resistor R_s and the parallel of R_1

and R_2:

$$N_I = 4kTR_s \left(\frac{R_1\ R_2}{R_1\ R_2 + R_s\ R_1 + R_s\ R_2} \right)^2.$$

The amplifier's voltage noise is a function of the current $I_{n,ni} = I_{n,ii} = I_n = 2.1\,\text{pA}\,\text{Hz}^{-1/2}$ and voltage noise $V_n = 2.1\,\text{nV}\,\text{Hz}^{-1/2}$ of the opamp, and the thermal noise of the resistors:

$$N_A = c_1 V_{n1}^2 + c_2 I_{n,ni1}^2 + c_3 I_{n,ii1}^2 + c_4 V_{n,R_1}^2 + c_5 V_{n,R_2}^2 + c_6 V_{n2}^2 + \\ + c_7 I_{n,ni2}^2 + c_8 I_{n,ii2}^2 + c_9 V_{n,R_3}^2 + c_{10} V_{n,R_4}^2 + c_{11} V_{n,R_5}^2.$$

The input voltage noise of the two opamp appears at the amplifier input with scaling factors $c_1 = c_6 = 1$. The first opamp's non-inverting input current noise develops a voltage through the parallel combination of R_s, R_1 and R_2 and it appears at the amplifier's input:

$$c_2 I_{n,ni1}^2 = \left(\frac{R_s\ R_1\ R_2}{R_s\ R_1 + R_s\ R_2 + R_1\ R_2} \right)^2 I_{n,ni1}^2.$$

The inverting input current noise generates a voltage drop across R_3:

$$c_3 I_{n,ii1}^2 = (R_3)^2\ I_{n,ii1}^2.$$

The noise voltage term V_{n,R_1} associated with R_1 is equal to $\sqrt{4kTR_1}$ and the noise is divided by R_1 and the parallel of resistors R_s and R_2.

$$c_4 V_{n,R_1}^2 = 4kTR_1 \left(\frac{R_s\ R_2}{R_s\ R_1 + R_s\ R_2 + R_1\ R_2} \right)^2.$$

A similar result is obtained for the noise voltage term V_{n,R_2}:

$$c_5 V_{n,R_2}^2 = 4kTR_2 \left(\frac{R_s\ R_1}{R_s\ R_1 + R_s\ R_2 + R_1\ R_2} \right)^2.$$

The second opamp non-inverting input current noise develops a voltage drop through the resistor R_3 that appears at the amplifier's input:

$$c_7 I_{n,ni2}^2 = (R_3)^2\ I_{n,ni2}^2.$$

The inverting input current noise generates a voltage drop through the parallel combination of R_4 and R_5:

$$c_8 I_{n,ii2}^2 = \left(\frac{R_4\ R_5}{R_4 + R_5} \right)^2 I_{n,ii2}^2.$$

The noise voltage term V_{n,R_3} associated with R_3 is equal to $\sqrt{4kTR_3}$ and appears to the inverting input of the first opamp:

$$c_9 V_{n,R_3}^2 = 4kTR_3.$$

The noise voltage term V_{n,R_4} associated with R_4 is equal to $\sqrt{4kTR_4}$ and it is divided by the resistors R_5 and R_4:

$$c_{10} V_{n,R_4}^2 = 4kTR_4 \left(\frac{R_5}{R_4 + R_5} \right)^2.$$

The noise voltage term V_{n,R_5} associated with R_5 is equal to $\sqrt{4kTR_5}$ and it is divided by the resistors R_4 and R_5:

$$c_{11} V_{n,R_5}^2 = 4kTR_5 \left(\frac{R_4}{R_4 + R_5} \right)^2.$$

The resulting noise figure is $NF = 119$ ($N_I = 5 \times 10^{-6}\,\text{nV}\,\text{Hz}^{-1/2}$, $N_A = 3.9\,\text{nV}\,\text{Hz}^{-1/2}$ and $N_O = 12.3\,\text{nV}\,\text{Hz}^{-1/2}$). The amplifier output noise expressed in term of power is $N_O = 46\,\mu\text{W}\,\text{Hz}^{-1/2}$.

A.3 Gated PMT

The time-resolved fluorescence signal is recorded by using a 12-stage end window linear PMT (8575, Burle Electron Tubes). Spontaneous emission can be detrimental for LIF measurement, because it can generate a large signal compared to the fluorescence one. In particular spontaneous emission can cause the saturation of PMT, which then required some time to recovery normal operation. To overcame this problem, we used a gating strategy to kept the PMT always off except during the LIF signal acquisition[119, 120, 121].

A.3.1 Design and testing

We chose to gate the PMT by acting on the single dynode 7. Figure A.7 presents a scheme of the technique. In this way the electrons travelling inside the PMT are periodically stopped, avoiding strong current flowing in the last dynodes. A half-bridge configuration based on high-voltage very fast IGBTs (STGF3NC120HD, ST Microelectronics) is used to change the potential of dynode 7. The drive of the IGBT gates is performed

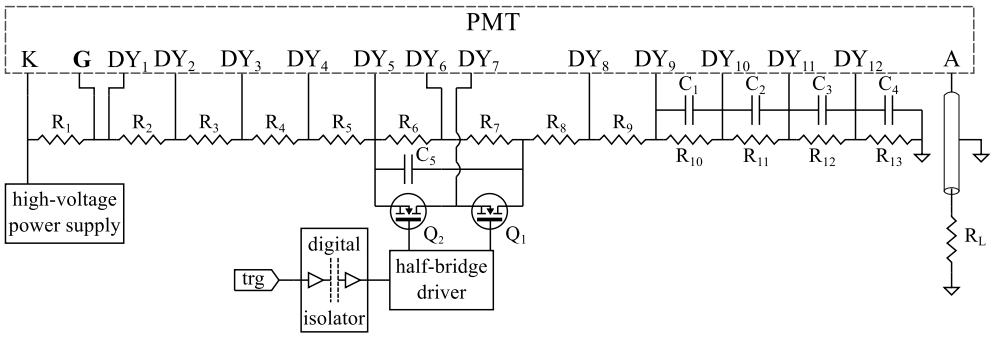

Figure A.7: Schematic representation of the PMT voltage divider and dynode 7 switching circuit. $R_1 = 400\ k\Omega$, $R_2 = 100\ k\Omega$, $R_3 = 130\ k\Omega$, R_4 through $R_{13} = 100\ k\Omega$, $R_L = 50\ \Omega$, $C_1 = 5$ nF, $C_2 = 10$ nF, $C_3 = 20$ nF, $C_4 = 50$ nF and $C_5 = 1.1$ µF. Q_1 and Q_2 are the high-side and low-side IGBTs of the half-bridge, respectively. The voltage divider is biased at $V_S = -2750$ V.

by a high-voltage, high and low-side driver (NCP5111, ON Semiconductor), with a high voltage range (600 V), an internal fixed delay time of 650 ns between the two IGBT gate-state change. A 1414 V isolation-rated working voltage digital isolator (ISO7520C, Texas Instruments) connects the external trigger signal to the half-bridge driver. A DC/DC converter with maximum $1410\ V_p$ working voltage I/O isolation (THB 6-1212, Traco Power) is used to power the circuit.

To test the PMT performances we used a continuous UV-light source (UVTOP 305, Set). An external trigger with $t_{on} = 10$ µs and $t_{off} = 90$ µs was used to gate the PMT. Results are shown in Figure A.8. The two fixed 650 ns delay times are visible, and the counts reach a steady state after 1.25 µs from the trigger rising edge. An over shot in the signal is present at the end of the on time and it is probably due to noise produced by the low side IGBT transition to the on-state. The average number of counts in the on state is $21.7(3) \times 10^3$, while the counts in the off region (sampled for a total extension of 44 µs) are zero.

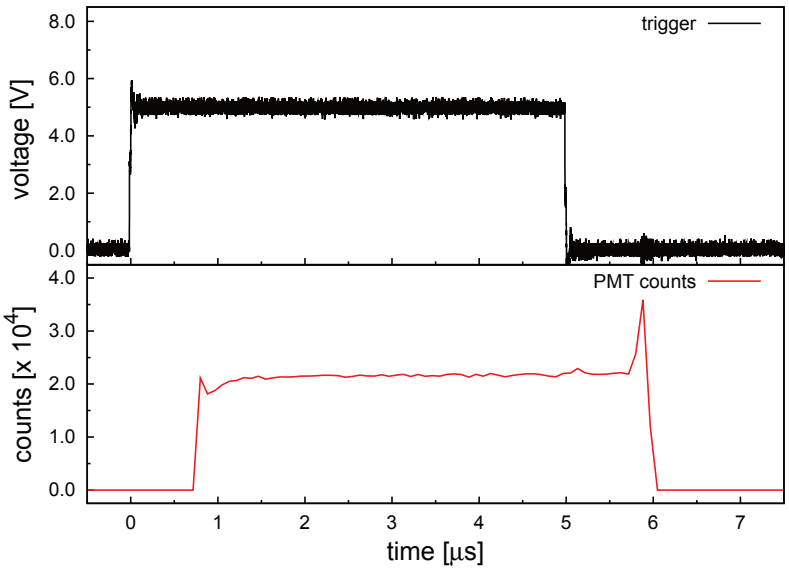

Figure A.8: Top: trigger signal; bottom: counts in function of times. A count is detected when the PMT voltage is larger than $-100\,\mathrm{mV}$.

Appendix B

Diatomic molecules nomenclature

B.1 Good quantum numbers

The angular momenta that describe the energy levels of diatomic molecules are:

- the electronic spin angular momentum $\boldsymbol{S}$;
- the electronic orbital angular momentum $\boldsymbol{L}$;
- the total angular momentum $\boldsymbol{J}$;
- the rotational angular momentum of the nuclei $\boldsymbol{R}$;
- the total angular momentum excluding electron spin $\boldsymbol{N} = \boldsymbol{J} - \boldsymbol{S}$.

We adopt the LIFBASE nomenclature, that is equal to the one used by Brown and Carrigton [122]. In other publications, [123, 124], the quantum number of the total angular momentum excluding electron spin is labelled K, while N is used for the angular momentum of nuclear rotation.

In particular, the orbital angular momentum projection about the internuclear axis quantum number $\boldsymbol{\Lambda}$ (indicated by the term symbols Σ, Π, Δ, Φ, Γ, ... for 0, 1, 2, 3, 4, ..., respectively), the total electron spin quantum number $\boldsymbol{S}$ and the spin projection about the internuclear axis quantum number $\boldsymbol{\Sigma}$, ($\Sigma = -S, -S+1, ..., S$), define the electronic quantum state of the molecule according to the following notation:

$$^{2S+1}\Lambda_{\Lambda+\Sigma}.$$

Angular momenta can be coupled in different ways, corresponding to the Hund's coupling cases [122]. We discuss the two most frequently encountered cases: *a* and *b*. Hund's case *c*, *d* and *e* will not be discussed.

B.1.1 Hund's case *a*

Case *a* is characterised by a weak interaction between nuclear rotation and electronic spin (see Figure B.1 left). On the other hand the electronic motion is coupled strongly to the line joining the nuclei. The total electronic angular momentum about the internuclear axis

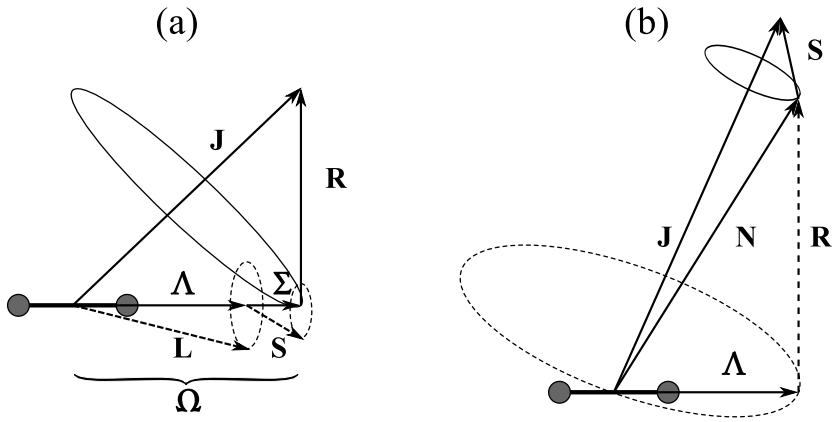

Figure B.1: Hund's case *a* (left) and *b* (right) schematic representation.

($\Omega = |\Lambda + \Sigma|$) is well defined. The total angular momentum $\boldsymbol{J}$ is the resultant of $\boldsymbol{\Omega}$ and the angular momentum of nuclear rotation $\boldsymbol{R}$.

B.1.2 Hund's case *b*

The Hund's case *b* is characterised by a weak or zero coupling between $\boldsymbol{S}$ and the internuclear axis (see Figure B.1 right). When the orbital angular momentum is not zero ($\Lambda \neq 0$), it adds to $\boldsymbol{R}$ to give $\boldsymbol{N}$, which is the total angular momentum apart from spin. The combination of $\boldsymbol{N}$ and $\boldsymbol{S}$ forms the total angular momentum including spin $\boldsymbol{J}$.

B.1.3 Electronic states nomenclature

When dealing with molecular electronic transitions, the upper state is written before the lower one (e.g. $^2\Sigma^+ - {}^2\Pi$). The electronic states are distinguished by an additional letter $X,\ A,\ B,\ C, ...,\ a,\ b,\ c, ...$ in front of the term symbol, where X indicates the ground state and the other letters the excited states (e.g. $A^2\Sigma^+ - X^2\Pi$). The arrow between the two term symbols is used to indicate if the transition is observed in emission (e.g. $A^2\Sigma^+ \rightarrow X^2\Pi$) or absorption (e.g. $A^2\Sigma^+ \leftarrow X^2\Pi$).

B.2 $A^2\Sigma^+ \leftrightarrow X^2\Pi$ transitions for OH

The $^2\Sigma$ state belongs to Hund's case *b* ($\Lambda = 0$). The $^2\Pi$ state generally belongs to an intermediate case between *a* and *b*. In the case of OH, for relatively cold temperatures (around 200 K), the $^2\Pi$ state is best described by the Hund's case *a* [125]. Increasing the temperature, large rotations cause a transition to Hund's case *b* [123]. Our experiment is carried out between 300 K and 500 K, so that we decide to adopt the Hund's case *b* quantum numbers set. According to Luque *et al.* [36], the name of rotational branches is given by $\Delta N = N' - N''$ where N' refers to the upper state and N'' to the lower. The possible branches are five, $\Delta N = -2,\ -1,\ 0,\ 1,\ 2$, indicated by the letters $O,\ P,\ Q,\ R,\ S$, respectively. The nomenclature is:

$$^{\Delta J}\Delta N_{F'F''}\left(N''\right),$$

where for $F = 1$ (F_1 sub-manifold) $J = N + 1/2$ and for $F = 2$ (F_2 sub-manifold) $J = N - 1/2$. The superscript of the F therm refer to the level: F' for the upper and F'' for the lower. For $F' = F''$, one of the two subscript of the branch is omitted.

B.2.1 Λ-Splitting

The $^2\Pi$ rotational ground state is splitted by spin-orbit interaction in two sub-manifold components F_1 ($^2\Pi_{3/2}$, $J = N + 1/2$) and F_2 ($^2\Pi_{1/2}$, $J = N - 1/2$). Λ-doubling further splits the components into +/- sublevels. This determines four rotational manifolds F_1, F_2 and F_1', F_2' [123], which can also be classified according to notation "e, f" parity. The latter choice makes the notation independent of the coupling case [126], with labels $F_{1e}(N)$

- $F_{1f}(N)$, and $F_{2e}(N)$ - $F_{2f}(N)$ for $^2\Pi_{1/2}$ and $^2\Pi_{3/2}$ sub-states, respectively. Analogous notations are used for the $^2\Sigma$ state although Λ = 0 and no Λ-doubling occurs. No line doublets appear due to the selection rule according to which *positive terms combine only with negative and vice versa* (see [123], p. 241 and 257), or equivalently $e \leftrightarrow e$ and $f \leftrightarrow f$ transitions are allowed for $\Delta J = \pm 1$ branches, while $e \leftrightarrow f$ are allowed for the $\Delta J = 0$ branch [126]. Since the Λ energy splitting is very small, the populations of the two sublevels are identical, and thus equal to one half of the F(N) population. Then, since only one of the two +/- or e/f sublevels is active in the absorption process, one half of the rotational level population must be considered. Figure B.2 shows the energy diagram of the $(X, \upsilon = 0)$ and $(A, \upsilon = 1)$ states of OH with the transitions used in the LIF experiment (see Chapter 3).

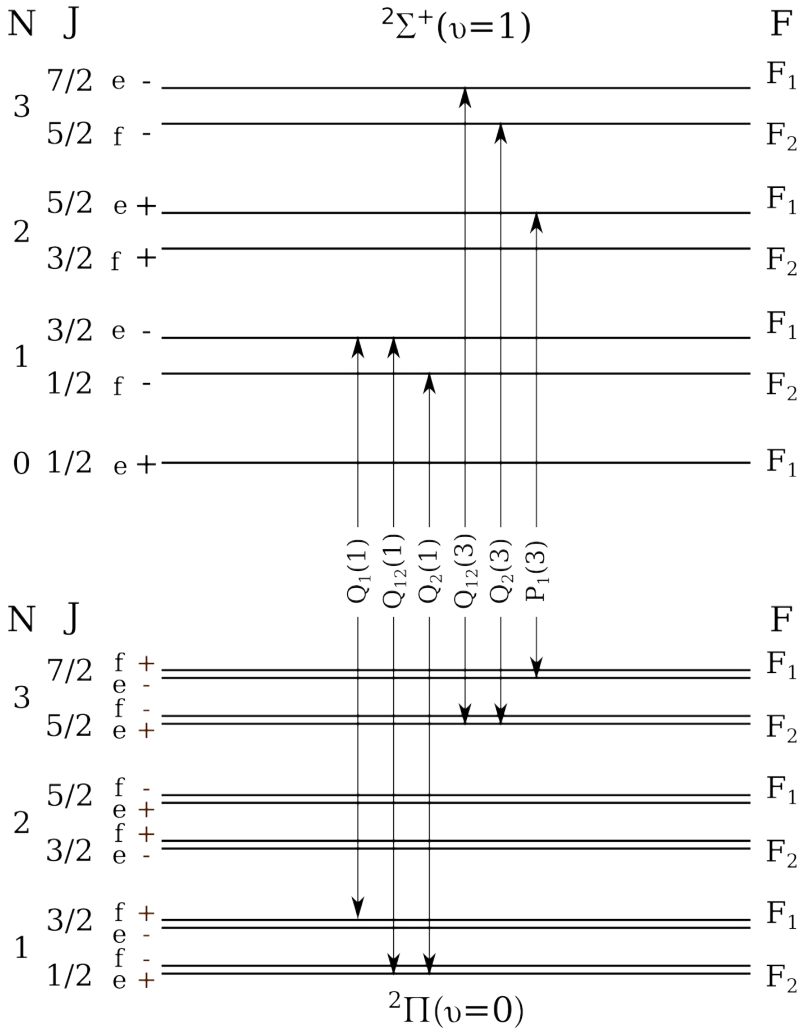

Figure B.2: Energy diagram of the $A^2\Sigma^+$ $(\upsilon = 1)$ and $X^2\Pi$ $(\upsilon = 0)$. Arrows represent the transitions used in the LIF experiment. The parity components are labelled both by absolute parity (+/-) and e/f parity. The diagram is not to scale for clarity.

Bibliography

[1] G. Centi and S. Perathoner, *Green Carbon Dioxide, Advantages in CO_2 Utilizations*. John Wiley & Sons, Inc., 2014.

[2] C.-J. Liu, B. Xue, B. Eliasson, F. He, Y. Li, and G.-H. Xu, "Methane conversion to higher hydrocarbons in the presence of carbon dioxide using dielectric-barrier discharge plasmas," *Plasma Chem. Plasma Process.*, vol. 21, pp. 301–310, 2001.

[3] Istadi and N. Amin, "Co-generation of synthesis gas and C_{2+} hydrocarbons from methane and carbon dioxide in a hybrid catalytic-plasma reactor: A review," *Fuel*, vol. 85, pp. 577–592, 2006.

[4] Y. ping Zhang, Y. Li, Y. Wang, C. jun Liu, and B. Eliasson, "Plasma methane conversion in the presence of carbon dioxide using dielectric-barrier discharges," *Fuel Process. Technol.*, vol. 83, pp. 101 – 109, 2003.

[5] G. Scarduelli, G. Guella, D. Ascenzi, and P. Tosi, "Synthesis of liquid organic compounds from CH_4 and CO_2 in a dielectric barrier discharge operating at atmospheric pressure," *Plasma Process. Polym.*, vol. 8, pp. 25–31, 2011.

[6] T. Nozaki, A. Ağıral, S. Yuzawa, J. H. Gardeniers, and K. Okazaki, "A single step methane conversion into synthetic fuels using microplasma reactor," *Chemical Engineering Journal*, vol. 166, pp. 288 – 293, 2011.

[7] X. Tu and J. C. Whitehead, "Plasma dry reforming of methane in an atmospheric pressure AC gliding arc discharge: Co-generation of syngas and carbon nanomaterials," *International Journal of Hydrogen Energy*, vol. 39, pp. 9658 – 9669, 2014.

[8] L. M. Martini, G. Dilecce, G. Guella, A. Maranzana, G. Tonachini, and P. Tosi, "Oxidation of CH_4 by CO_2 in a dielectric barrier discharge," *Chem. Phys. Lett.*, vol. 593, pp. 55–60, 2014.

[9] M. Scapinello, L. M. Martini, and P. Tosi, "CO_2 hydrogenation by CH_4 in a dielectric barrier discharge: Catalytic effects of nickel and copper," *Plasma Process. Polym.*, vol. 11, pp. 624–628, 2014.

[10] R. Snoeckx, R. Aerts, X. Tu, and A. Bogaerts, "Plasma-based dry reforming: A computational study ranging from the nanoseconds to seconds time scale," *J. Phys. Chem. C*, vol. 117, pp. 4957–4970, 2013.

[11] A. Fridman and G. Friedman, *Plasma Medicine*. Wiley, 2013.

[12] J. V. der Paal, S. Aernouts, A. C. T. van Duin, E. C. Neyts, and A. Bogaerts, "Interaction of o and oh radicals with a simple model system for lipids in the skin barrier: a reactive molecular dynamics investigation for plasma medicine," *J. Phys. D: Appl. Phys.*, vol. 46, p. 395201, 2013.

[13] S. Norberg, W. Tian, E. Johnsen, and M. Kushner, "Atmospheric pressure plasma jets interacting with liquid covered tissue: touching and not-touching the liquid," *J. Phys. D: Appl. Phys.*, vol. 47, p. 475203, 2014.

[14] D. Riès, G. Dilecce, E. Robert, P. F. Ambrico, S. Dozias, and J.-M. Pouvesle, "LIF and fast imaging plasma jet characterization relevant for NTP biomedical applications," *J. Phys. D: Appl. Phys.*, vol. 47, p. 275401, 2014.

[15] K. McKay, D. X. Liu, M. Z. Rong, F. Iza, and M. G. Kong, "Generation and loss of reactive oxygen species in low-temperature atmospheric-pressure RF He + O_2 + H_2O plasmas," *J. Phys. D: Appl. Phys.*, vol. 45, p. 172001, 2012.

[16] F. Thevenet, L. Sivachandiran, O. Guaitella, C. Barakat, and A. Rousseau, "Plasma–catalyst coupling for volatile organic compound removal and indoor air treatment: a review," *J. Phys. D: Appl. Phys.*, vol. 47, p. 224011, 2014.

[17] C. Hibert, I. Gaurand, O. Motret, and J. M. Pouvesle, "$[\mathrm{OH}(X)]$ measurements by resonant absorption spectroscopy in a pulsed dielectric barrier discharge," *J. Appl. Phys.*, vol. 85, pp. 7070–7075, 1999.

[18] G. Dilecce, P. F. Ambrico, M. Simek, and S. De Benedictis, "OH density measurement by time-resolved broad band absorption spectroscopy in an Ar-H2O dielectric barrier discharge," *J. Phys. D: Appl. Phys.*, vol. 45, p. 125203, 2012.

[19] G. Dilecce, "Optical spectroscopy diagnostics of discharges at atmospheric pressure," *Plasma Sources Sci. Technol.*, vol. 23, p. 015011, 2014.

[20] H.-J. Kunze, *Introduction to Plasma Spectroscopy*. Springer, 2009.

[21] H. Jentschke, U. Schumacher, and K. Hirsch, "Studies of silicon erosion in plasma-target-interaction from optical emission and absorption spectroscopy," *Contrib. Plasma Phys.*, vol. 38, pp. 501–512, 1998.

[22] W. Demtröder, *Laser Spectroscopy - Basic Concepts and Instrumentation*. Springer-Verlag, 1982.

[23] L. M. Martini, G. Dilecce, M. Scotoni, P. Tosi, and S. De Benedictis, "OH Density Measurements by Time- Resolved Broad Band Absorption Spectroscopy in a He-H_2O Dielectric Barrier Discharge with Small O_2 Addition," *Plasma Process. Polym.*, vol. 11, pp. 232–238, 2014.

[24] G. Meijer, M. G. Boogaarts, R. T. Jongma, D. H. Parker, and A. M. Wodtke, "Coherent cavity ring down spectroscopy," *Chem. Phys. Lett.*, vol. 217, pp. 112 – 116, 1994.

[25] C. O. Laux, T. G. Spence, C. H. Kruger, and R. N. Zare, "Optical diagnostics of atmospheric pressure air plasmas," *Plasma Sources Sci. Technol.*, vol. 12, p. 125, 2003.

[26] Z. W. Liu, X. F. Yang, A. M. Zhu, G. L. Zhao, and Y. Xu, "Determination of the OH radical in atmospheric pressure dielectric barrier discharge plasmas using near

infrared cavity ring-down spectroscopy," *Eur. Phys. J. D*, vol. 48, pp. 365 – 373, 2008.

[27] G. D. Stancu, F. Kaddouri, D. A. Lacoste, and C. O. Laux, "Atmospheric pressure plasma diagnostics by OES, CRDS and TALIF," *J. Phys. D: Appl. Phys.*, vol. 43, p. 124002, 2010.

[28] I. P. Vinogradov, A. Dinkelmann, and A. Lunk, "Measurement of the absolute CF_2 concentration in a dielectric barrier discharge running in argon/fluorocarbon mixtures," *J. Phys. D: Appl. Phys.*, vol. 37, p. 3000, 2004.

[29] A. V. Pipa, T. Bindemann, R. Foest, E. Kindel, J. Röpcke, and K.-D. Weltmann, "Absolute production rate measurements of nitric oxide by an atmospheric pressure plasma jet (APPJ)," *J. Phys. D: Appl. Phys.*, vol. 41, p. 194011, 2008.

[30] S. G. Belostotskiy, T. Ouk, V. M. Donnelly, D. J. Economou, and N. Sadeghi, "Time- and space-resolved measurements of Ar($1s_5$) metastable density in a microplasma using diode laser absorption spectroscopy," *J. Phys. D: Appl. Phys.*, vol. 44, p. 145202, 2011.

[31] C. Penache, M. Miclea, A. Bräuning-Demian, O. Hohn, S. Schössler, T. Jahnke, K. Niemax, and H. Schmidt-Böcking, "Characterization of a high-pressure microdischarge using diode laser atomic absorption spectroscopy," *Plasma Sources Sci. Technol.*, vol. 11, p. 476, 2002.

[32] K. Niemi, J. Waskoenig, N. Sadeghi, T. Gans, and D. O'Connell, "The role of helium metastable states in radio-frequency driven helium–oxygen atmospheric pressure plasma jets: measurement and numerical simulation," *Plasma Sources Sci. Technol.*, vol. 20, p. 055005, 2011.

[33] P. Bruggeman, G. Cunge, and N. Sadeghi, "Absolute OH density measurements by broadband UV absorption in diffuse atmospheric-pressure He-H_2O RF glow discharges," *Plasma Sources Sci. Technol.*, vol. 21, p. 035019, 2012.

[34] G. Dilecce and S. De Benedictis, "Laser diagnostics of high-pressure discharges: laser induced fluorescence detection of OH in He/Ar-H_2O dielectric barrier discharges," *Plasma Phys. Controlled Fusion*, vol. 53, p. 124006, 2011.

[35] G. Dilecce, P. F. Ambrico, M. Simek, and S. De Benedictis, "LIF diagnostics of hydroxyl radical in atmospheric pressure He-H_2O dielectric barrier discharges," *Chem. Phys.*, vol. 398, pp. 142–147, 2012.

[36] J. Luque and D. R. Crosley, "Lifbase: Database and spectral simuation program (version 2.1)," tech. rep., SRI International Report MP 99-099, 1999.

[37] V. Kasyutich, "Pressure broadening parameters of the hydroxyl radical $A^2\Sigma^+(\upsilon' = 0) \leftarrow X^2\Pi_{3/2}(\upsilon'' = 0)$ transitions at ca.308 nm," *Eur. Phys. J. D.*, vol. 33, pp. 29–33, 2005.

[38] L. M. Martini, G. Dilecce, M. Scotoni, P. Tosi, and S. De Benedictis, "Corrigendum on oh density measurements by time- resolved broad band absorption spectroscopy in a he-h_2o dielectric barrier discharge with small o_2 addition," *Submitted to Plasma Process. Polym.*

[39] M. Galassi, J. Davies, J. Theiler, B. Gough, G. Jungman, P. Alken, M. Booth, and F. Rossi, *GNU Scientific Library Reference Manual*. 2011.

[40] J. E. Dennis and R. B.Schnabel, *Numerical methods for unconstrained optimization and nonlinear equations*. Society for Industrial and Applied Mathematics, 1987.

[41] B. Löhden, S. Kuznetsova, K. Sengstock, V. Baev, A. Goldman, S. Cheskis, and B. Pálsdóttir, "Fiber laser intracavity absorption spectroscopy for in situ multicomponent gas analysis in the atmosphere and combustion environments," *Appl. Phys. B*, vol. 102, pp. 331–344, 2011.

[42] K. Muraoka and M. Maeda, "Application of laser-induced fluorescence to high-temperature plasmas," *Plasma Phys. Controlled Fusion*, vol. 35, p. 633, 1993.

[43] R. Ono and T. Oda, "Dynamics and density estimation of hydroxyl radicals in a pulsed corona discharge," *J. Phys. D: Appl. Phys.*, vol. 35, pp. 2133 – 2138, 2002.

[44] R. Ono and T. Oda, "Dynamics of ozone and OH radicals generated by pulsed corona discharge in humid-air flow reactor measured by laser spectroscopy," *J. Appl. Phys.*, vol. 93, pp. 5876–5882, 2003.

[45] S. Kanazawa, H. Tanaka, A. Kajiwara, T. Ohkubo, Y. Nomoto, M. Kocik, J. Mizeraczyk, and J.-S. Chang, "LIF imaging of OH radicals in DC positive streamer coronas," *Thin Solid Films*, vol. 515, pp. 4266 – 4271, 2007.

[46] S. Kanazawa, H. Kawano, S. Watanabe, T. Furuki, S. Akamine, R. Ichiki, T. Ohkubo, M. Kocik, and J. Mizeraczyk, "Observation of OH radicals produced by pulsed discharges on the surface of a liquid," *Plasma Sources Sci. Technol.*, vol. 20, p. 034010, 2011.

[47] Y. Nakagawa, R. Ono, and T. Oda, "Density and temperature measurement of OH radicals in atmospheric-pressure pulsed corona discharge in humid air," *J. Appl. Phys.*, vol. 110, p. 073304, 2011.

[48] L. Magne, S. Pasquiers, N. Blin-Simiand, and C. Postel, "Production and reactivity of the hydroxyl radical in homogeneous high pressure plasmas of atmospheric gases containing traces of light olefins," *J. Phys. D: Appl. Phys.*, vol. 40, pp. 3112 – 3127, 2007.

[49] Y. Teramoto, H.-H. Kim, A. Ogata, and N. Negishi, "Measurement of OH($X^2\Sigma$) in immediate vicinity of dielectric surface under pulsed dielectric barrier discharge at atmospheric pressure using two geometries of laser induced fluorescence," *J. Appl. Phys.*, vol. 115, p. 133302, 2014.

[50] N. Srivastava and C. Wang, "Effects of water addition on OH radical generation and plasma properties in an atmospheric argon microwave plasma jet," *J. Appl. Phys.*, vol. 110, p. 053304, 2011.

[51] Q. Xiong, A. Y. Nikiforov, L. Li, P. Vanraes, N. Britun, R. Snyders, X. P. Lu, and C. Leys, "Absolute OH density determination by laser induced fluorescence spectroscopy in an atmospheric pressure RF plasma jet," *Eur. Phys. J. D*, vol. 66, p. 281, 2012.

[52] S. Yonemori, Y. Nakagawa, R. Ono, and T. Oda, "Measurement of OH density and air-helium mixture ratio in an atmospheric-pressure helium plasma jet," *J. Phys. D: Appl. Phys.*, vol. 45, p. 225202, 2012.

[53] J. Vorac, P. Dvorak, V. Prochazka, J. Ehlbeck, and S. Reuter, "Measurement of OH concentration in Ar RF plasma jet by LIF," *Plasma Sources Sci. Technol.*, vol. 22, p. 025016, 2013.

[54] X. Pei, Y. Lu, S. Wu, Q. Xiong, and X. Lu, "A study on the temporally and spatially resolved OH radical distribution of a room-temperature atmospheric-pressure plasma jet by laser-induced fluorescence imaging," *Plasma Sources Sci. Technol.*, vol. 22, p. 025023, 2013.

[55] J. Vorac, A. Obrusn, V. Prochazka, P. Dvoak, and M. Talaba, "Spatially resolved measurement of hydroxyl radical (OH) concentration in an argon RF plasma jet by planar laser-induced fluorescence," *Plasma Sources Sci. Technol.*, vol. 23, p. 025011, 2014.

[56] X. Pei, S. Wu, Y. Xian, X. Lu, and Y. Pan, "On OH Density of an Atmospheric Pressure Plasma Jet by Laser-Induced Fluorescence," *IEEE Trans. Plasma Sci.*, vol. 42, p. 1206, 2014.

[57] T. Verreycken, R. M. van der Horst, A. H. F. M. Baede, E. M. Van Veldhuizen, and P. J. Bruggeman, "Time and spatially resolved LIF of OH in a plasma filament in atmospheric pressure He-H_2O," *J. Phys. D: Appl. Phys.*, vol. 45, p. 045205, 2012.

[58] T. Verreycken, N. Sadeghi, and P. J. Bruggeman, "Time-resolved absolute OH density of a nanosecond pulsed discharge in atmospheric pressure He-H_2O: absolute calibration, collisional quenching and the importance of charged species in OH production," *Plasma Sources Sci. Technol.*, vol. 23, p. 045005, 2014.

[59] T. Verreycken and P. J. Bruggeman, "OH dynamics in a nanosecond pulsed plasma filament in atmospheric pressure He-H_2O upon the addition of O_2," *Plasma Chem. Plasma Process.*, vol. 34, pp. 605 – 619, 2014.

[60] I. Choi, Z. Yin, I. V. Adamovich, and W. R. Lempert, "Hydroxyl radical kinetics in repetitively pulsed hydrogen-air nanosecond plasmas," *IEEE Trans. Plasma Sci.*, vol. 39, pp. 3288–3299, 2011.

[61] K. Bennett and R. Byer, "Computer-controllable wedged-plate optical variable attenuator," *Appl. Optics*, vol. 19, pp. 2408–2412, 1980.

[62] P. Celliers, K. Estabrook, R. Wallace, J. Murray, L. Da Silva, B. MacGowan, B. Van Wonterghem, and K. Manes, "Spatial filter pinhole for high-energy pulsed lasers," *Appl. Optics*, vol. 37, pp. 2371–2378, 1998.

[63] S. De Benedictis and G. Dilecce, *Physics and technology of atmospheric pressure discharges*, ch. Laser-Induced Fluorescence Methods for Transient Species Detection in High-Pressure Discharges, pp. 261–284. Taylor and Francis, 2013.

[64] D. X. Liu, F. Iza, X. H. Wang, M. G. Kong, and M. Z. Rong, "He+O_2+H_2O plasmas as a source of reactive oxygen species," *Appl. Phys. Lett.*, vol. 98, p. 221501, 2011.

[65] J. L. Walsh and M. G. Kong, "Contrasting characteristics of linear-field and cross-field atmospheric plasma jets," *Appl. Phys. Lett.*, vol. 93, pp. –, 2008.

[66] T. Verreycken, R. Mensink, R. van der Horst, N. Sadeghi, and P. J. Bruggeman, "Absolute OH density measurements in the effluent of a cold atmospheric-pressure Ar-H_2O RF plasma jet in air," *Plasma Sources Sci. Technol.*, vol. 22, p. 055014, 2013.

[67] M. J. Dunn and A. R. Masri, "A comprehensive model for the quantification of linear and nonlinear regime laser-induced fluorescence of OH under $A^2\Sigma^+ \leftarrow X^2\Pi\,(1,0)$ excitation," *Appl. Phys. B*, vol. 101, pp. 445 – 463, 2010.

[68] J. Luque, R. J. H. Klein-Douwel, J. B. Jeffries, G. P. Smith, and D. R. Crosley, "Quantitative laser-induced fluorescence of CH in atmospheric pressure flames," *Appl. Phys. B*, vol. B 75, pp. 779 – 790, 2002.

[69] T. Verreycken, R. M. van der Horst, N. Sadeghi, and P. J. Bruggeman, "Absolute calibration of OH density in a nanosecond pulsed plasma filament in atmospheric

pressure He-H_2O: comparison of independent calibration methods," *J. Phys. D: Appl. Phys.*, vol. 46, p. 464004, 2013.

[70] R. Loudon, *Quantum theory of light*. Oxford University Press, 2000.

[71] J. W. Daily, "Use of rate equations to describe laser excitation in flames," *Appl. Opt.*, vol. 16, pp. 2322–2327, 1977.

[72] T. B. Settersten and M. A. Linne, "Modeling pulsed excitation for gas-phase laser diagnostics," *J. Opt. Soc. Am. B*, vol. 19, pp. 954–964, 2002.

[73] P. Avan and C. Cohen-Tannoudji, "Two-level atom saturated by a fluctuating resonant laser beam. calculation of the fluorescence spectrum," *J. Phys. B:At. Mol. Phys.*, vol. 10, pp. 155–170, 1977.

[74] J. W. Daily, "Saturation of fluorescence in flames with a gaussian laser beam," *Appl. Opt.*, vol. 17, pp. 225–229, 1978.

[75] R. K. Lengel and D. R. Crosley, "Energy transfer in $A^2\Sigma^+$ OH. II. Vibrational," *J. Chem. Phys.*, vol. 68, pp. 5309–5324, 1978.

[76] L. R. Williams and D. R. Crosley, "Collisional vibrational energy transfer of OH$(A^2\Sigma^+, \upsilon' = 1)$," *J. Chem. Phys.*, vol. 104, pp. 6507–6514, 1996.

[77] R. A. Copeland, M. J. Dyer, and D. R. Crosley, "Rotational-level-dependent quenching of $A^2\Sigma^+$ OH and OD," *J. Chem. Phys.*, vol. 82, pp. 4022–4032, 1985.

[78] J. Burris, J. J. Butler, T. J. Mcgee, and W. S. Heaps, "Collisional deactivation rates for A $^2\Sigma^+(\upsilon = 1)$ state of OH," *Chemical Physics*, vol. 124, pp. 251 – 258, 1988.

[79] R. A. Copeland, M. L. Wise, and D. R. C. and *J. Phys. Chem.*, vol. 92, p. 5710, 1988.

[80] K. R. German, "Collision and quenching cross sections in the $A^2\Sigma^+$ state of OH and OD," *J. Chem. Phys.*, vol. 64, pp. 4065–4068, 1976.

[81] I. J. Wysong, J. B. Jeffries, and D. R. Crosley, "Quenching of $A^2\Sigma^+$ OH at 300 K by several colliders," *J. Chem. Phys*, vol. 92, pp. 5218–5222, 1990.

[82] A. E. Bailey, D. E. Heard, D. A. Henderson, and P. H. Paul, "Collisional quenching of OH($A^2\Sigma^+, v' = 0$) by H_2O between 211 and 294 K and the development of a unified model for quenching," *Chem. Phys. Lett.*, vol. 302, pp. 132 – 138, 1999.

[83] K. R. German, "Radiative and predissociative lifetimes of the V=0, 1, and 2 levels of the $A^2\Sigma^+$ state of OH and OD," *J. Chem. Phys.*, vol. 63, p. 5252, 1975.

[84] A. Jorg, A. Degli Esposti, and H. J. Werner, "Quantum scattering study of rotational energy transfer in OH($A^2\Sigma^+, v' = 0$) in collisions with He(1 S)," *J. Chem. Phys.*, vol. 93, p. 8757, 1990.

[85] A. Jorg, U. Maier, and K. Kohse-Hoinghaus, "Rotational energy transfer in OH ($A^2\Sigma^+, v' = 0$): A method for the direct determination of state-to-state transfer coefficients," *J. Chem. Phys.*, vol. 93, p. 6453, 1990.

[86] R. Kienle, A. Jorg, and K. Kohse-Hoinghaus, "State-to-state rotational energy transfer in OH($A^2\Sigma^+, v' = 1$)," *Appl. Phys. B*, vol. 56, pp. 249 – 258, 1993.

[87] G. Zizak, G. A. Petrucci, C. L. Stevenson, and J. D. Winefordner, "Ground state saturated population distribution of oh in an acetylene-air flame measured by two optical double resonance pump-probe approaches," *Appl. Opt.*, vol. 30, pp. 5270–5275, 1991.

[88] J. Tobai, T. Dreier, and J. W. Daily, "Rotational level dependence of ground state recovery rates for OH $X^2\Pi(v'' = 0)$ in atmospheric pressure flames using the picosecond saturating-pump degenerate four-wave mixing probe technique," *J. Chem. Phys.*, vol. 116, pp. 4030–4038, 2002.

[89] Z. Yin, A. Montello, C. D. Carter, W. R. Lempert, and I. V. Adamovich, "Measurements of temperature and hydroxyl radical generation/decay in lean fuel-air mixtures excited by a repetitively pulsed nanosecond discharge," *Combust. Flame*, vol. 160, pp. 1594–1608, 2013.

[90] M. A. Sobolewski, "Electrical characterization of radio-frequency discharges in the gaseous electronics conference reference cell," *J. Vac. Sci. Technol., A*, vol. 10, pp. 3550–3562, 1992.

[91] Z. Fang, Y. Qiu, and Y. Luo, "Surface modification of polytetrafluoroethylene film using the atmospheric pressure glow discharge in air," *J. Phys. D: Appl. Phys.*, vol. 36, pp. 2980–2985, 2003.

[92] N. De Geyter, R. Morent, and C. Leys, "Surface modification of a polyester nonwoven with a dielectric barrier discharge in air at medium pressure," *Surf. Coat. Technol.*, vol. 201, pp. 2460–2466, 2006.

[93] G. Nersisyan and W. Graham, "Characterization of a dielectric barrier discharge operating in an open reactor with flowing helium," *Plasma Sources Sci. Technol.*, vol. 13, pp. 582–587, 2004.

[94] T. C. Manley, "The electric characteristics of the ozonator discharge," *Trans. Electrochem. Soc.*, vol. 84, pp. 83–96, 1943.

[95] L. A. Rosenthal and D. A. Davis, "Electrical characterization of a corona discharge for surface treatment," *IEEE Trans. Ind. Appl.*, vol. IA-11, pp. 328–335, 1975.

[96] Z. Falkenstein and J. Coogan, "Microdischarge behaviour in the silent discharge of nitrogen-oxygen and water-air mixtures," *J. Phys. D: Appl. Phys.*, vol. 30, pp. 817–825, 1997.

[97] R. Valdivia-Barrientos, J. Pacheco-Sotelo, M. Pacheco-Pacheco, J. Benitez-Read, and R. Lopez-Callejas, "Analysis and electrical modelling of a cylindrical DBD configuration at different operating frequencies," *Plasma Sources Sci. Technol.*, vol. 15, pp. 237–245, 2006.

[98] G. Fortunato, "End-point determination by reflected power monitoring," *J. Sci. Instrum.*, vol. 20, p. 1051, 1987.

[99] W.-C. Zhu, B.-R. Wang, Z.-X. Yao, and Y.-K. Pu, "Discharge characteristics of an atmospheric pressure radio-frequency plasma jet," *J. Phys. D: Appl. Phys.*, vol. 38, p. 1396, 2005.

[100] S. Hofmann, K. van Gils, S. van der Linden, S. Iseni, and P. Bruggeman, "Time and spatial resolved optical and electrical characteristics of continuous and time modulated rf plasmas in contact with conductive and dielectric substrates," *Eur. Phys. J. D*, vol. 68, pp. 1–14, 2014.

[101] S. Hofmann, A. F. H. van Gessel, T. Verreycken, and P. Bruggeman, "Power dissipation, gas temperatures and electron densities of cold atmospheric pressure helium and argon RF plasma jets ," *Plasma Sources Sci. Technol.*, vol. 20, p. 065010, 2011.

[102] W. Guo and C. A. DeJoseph Jr, "Time-resolved current and voltage measurements on a pulsed rf inductively coupled plasma," *Plasma Sources Sci. Technol.*, vol. 10, p. 43, 2001.

[103] C. Mahony, P. Maguire, and W. Graham, "Electrical characterization of radio frequency discharges," *Plasma Sources Sci. Technol.*, vol. 14, p. S60, 2005.

[104] V. Léveillé and S. Coulombe, "Electrical probe calibration and power calculation for a miniature 13.56 mhz plasma source," *Meas. Sci. Technol.*, vol. 17, p. 3027, 2006.

[105] J. Benedikt, V. Raballand, A. Yanguas-Gil, K. Focke, and A. Von Keudell, "Thin film deposition by means of atmospheric pressure microplasma jet," *Plasma Phys. Controlled Fusion*, vol. 49, p. B419, 2007.

[106] J. Pawłat, R. Samoń, H. D. Stryczewska, J. Diatczyk, and T. Giżewski, "Rf-powered atmospheric pressure plasma jet for surface treatment," *Eur. Phys. J. Appl. Phys.*, vol. 61, p. 24322, 2013.

[107] A. Sobota, O. Guaitella, and A. Rousseau, "The influence of the geometry and electrical characteristics on the formation of the atmospheric pressure plasma jet," *Plasma Sources Sci. Technol.*, vol. 23, p. 025016, 2014.

[108] J. J. Shi, X. T. Deng, R. Hall, J. D. Punnett, and M. G. Kong, "Three modes in a radio frequency atmospheric pressure glow discharge," *J. Appl. Phys.*, vol. 94, pp. 6303–6310, 2003.

[109] A. Yanguas-Gil, K. Focke, J. Benedikt, and A. von Keudell, "Optical and electrical characterization of an atmospheric pressure microplasma jet for Ar/CH_4 and Ar/C_2H_2 mixtures," *J. Appl. Phys.*, vol. 101, p. 103307, 2007.

[110] S. M. Starikovskaia, "Plasma assisted ignition and combustion," *J. Phys. D: Appl. Phys.*, vol. 39, pp. R265–R299, 2006.

[111] I. V. Adamovich, I. Choi, N. Jiang, J.-H. Kim, S. Keshav, W. R. Lempert, E. Mintusov, M. Nishihara, M. Samimy, and M. U. M. A. Chaszeyka, "Plasma assisted ignition and high-speed flow control," *Plasma Sources Sci. Technol.*, vol. 18, p. 034018, 2009.

[112] A. Starikovskiy and N. Aleksandrov, "Plasma-assisted ignition and combustion," *Prog. Energ. Combust.*, vol. 39, pp. 61–110, 2013.

[113] K. Priya Arjunan and A. Morss Clyne, "Hydroxyl radical and hydrogen peroxide are primarily responsible for dielectric barrier discharge plasma-induced angiogenesis," *Plasma Processes and Polymers*, vol. 8, pp. 1154–1164, 2011.

[114] T. von Woedtke, S. Reuter, K. Masur, and K.-D. Weltmann, "Plasmas for medicine," *Physics Reports*, vol. 530, pp. 291 – 320, 2013.

[115] S.-H. Hong, E. J. Szili, A. T. A. Jenkins, and R. D. Short, "Ionized gas (plasma) delivery of reactive oxygen species (ROS) into artificial cells," *J. Phys. D: Appl. Phys.*, vol. 47, p. 362001, 2014.

[116] S. Yonemori and R. Ono, "Flux of oh and o radicals onto a surface by an atmospheric-pressure helium plasma jet measured by laser-induced fluorescence," *J. Phys. D: Appl. Phys.*, vol. 47, p. 125401, 2014.

[117] D. B. Graves, "The emerging role of reactive oxygen and nitrogen species in redox biology and some implications for plasma applications to medicine and biology," *J. Phys. D: Appl. Phys.*, vol. 45, p. 263001, 2012.

[118] R. Foest, M. Schmidt, and K. Becker, "Microplasmas, an emerging field of low-temperature plasma science and technology," *International Journal of Mass Spectrometry*, vol. 248, pp. 87 – 102, 2006.

[119] J. R. Herman, T. R. Londo, N. A. Rahman, and B. G. Barisas, "Normally on photomultiplier gating circuit with reduced post-gate artifacts for use in transient luminescence measurements," *Rev. Sci. Instrum.*, vol. 63, pp. 5454–5458, 1992.

[120] D. J. Creasey, P. A. Halford-Maw, D. E. Heard, J. E. Spence, and B. J. Whitaker, "Fast photomultiplier tube gating system for photon counting applications," *Rev. Sci. Instrum.*, vol. 69, pp. 4068–4073, 1998.

[121] G. Hagen, G. Gao, D. Roess, and B. Barisas, "Flexible normally on photomultiplier gating strategy for reducing postgate artifacts," *Rev. Sci. Instrum.*, vol. 76, p. 083117, 2005.

[122] J. M. Brown and A. Carrigton, *Rotational Spectroscopy of Diatomic Molecules*. Cambridge University Press, 2003.

[123] G. Herzberg and J. W. T. Spinks, *Molecular Spectra and Molecular Structure: I. Diatomic molecules*. 1950.

[124] G. H. Dieke and H. M. Crosswhite, "The ultraviolet bands of OH, fundamental data," *J. Quant. Spectrosc. Radiat. Transfer.*, vol. 2, pp. 97–199, 1962.

[125] M. Stevens and R. Conway, "Calculated OH $A^2\Sigma^+ - X^2\Pi$ $(0,0)$ band rotational emission rate factors for solar resonance fluorescence," *J. Geophys. Res.*, vol. 104, pp. 16369–16378, 1999.

[126] J. M. Brown, J. T. Hougen, K.-P. Huber, J. W. C. Johns, I. Kopp, P. H. Lefebvre-Brion, A. J. Merer, D. A. Ramsay, J. Rostas, and R. N. Zare, "The labeling of parity doublet levels in linear molecules," *J. Mol. Spectrosc.*, vol. 55, pp. 500 – 503, 1975.

List of Publications

1. L. Ricci, L. M. Martini, M. Franchi and A. Bertoldi, "A current-carrying coil design with improved liquid cooling arrangement," *Review of Scientific Instruments*, vol. 84, p. 065115, 2013.

2. L.M. Martini, G. Dilecce, G. Guella, A. Maranzana, G. Tonachini and P. Tosi, "Oxidation of CH_4 by CO_2 in a dielectric barrier discharge," *Chemical Physics Letters*, vol. 593, p. 55, 2014.

3. L. M. Martini, G. Dilecce, M. Scotoni, P. Tosi and S. De Benedictis, "OH Density Measurements by Time-Resolved Broad Band Absorption Spectroscopy in a He-H_2O Dielectric Barrier Discharge with Small O_2 Addition," *Plasma Processes and Polymers*, vol. 11, p. 232, 2014.

4. M. Scapinello, L. M. Martini, and P. Tosi, "CO_2 Hydrogenation by CH_4 in a Dielectric Barrier Discharge: Catalytic Effects of Nickel and Copper," *Plasma Processes and Polymers*, vol. 11, p. 624, 2014.

5. M. Scapinello, L. M. Martini, P. Tosi, A. Maranzana and G. Tonachini, "Molecular growth induced by oxygen species: experimental and theoretical study of naphthalene reacting with HO ($^2\Pi_{3/2}$), O (^3P), and O_2 ($^3\Sigma_g^-$)," submitted to *RSC Advances*.

6. G. Dilecce, L. M. Martini, P. Tosi, M. Scotoni and S. De Benedictis, "Laser Induced Fluorescence in atmospheric pressure discharges," submitted to *Plasma Sources Science and Technology*